Novel Nanobodies and Chromobodies to Study Biomarkers of Epithelial-Mesenchymal Transition (EMT)

Dissertation

der Mathematisch-Naturwissenschaftlichen Fakultät

der Eberhard Karls Universität Tübingen

zur Erlangung des Grades eines

Doktors der Naturwissenschaften

(Dr. rer. nat.)

vorgelegt von

Julia Maier

aus Singen (Hohentwiel)

Tübingen

2015

Gedruckt mit Genehmigung der Mathematisch-Naturwissenschaftlichen Fakultät der Eberhard Karls Universität Tübingen.

Tag der mündlichen Qualifikation: 23.11.2015
Dekan: Prof. Dr. Wolfgang Rosenstiel
1. Berichterstatter: Prof. Dr. Ulrich Rothbauer
2. Berichterstatter: Prof. Dr. Hansjürgen Volkmer

TABLE OF CONTENTS

TABLE OF CONTENTS

II

TABLE OF CONTENTS

ABBREVIATIONS

aa	amino acid
ATP	adenosine triphosphate
BSA	bovine serum albumin
CB	chromobody
CDR	complementary determining region
cfu	colony forming unit
C_H	constant domain of heavy chain
ChIP	chromatin immunoprecipitation
C_L	constant domain of light chain
CLMP	coxsackie-and adenovirus receptor-like membrane protein
CME	custom module editor
CSC	cancer stem cell
CTC	circulating tumor cell
ctr	control
D	diversity
Da	Dalton
DAPI	4',6-diamidino-2-phenylindole
DARPin	Designed Ankyrin Repeat Protein
DMEM	Dulbecco's Modified Eagle's Medium
DMSO	dimethyl sulfoxide
DNA	deoxyribonucleic acid
dNTP	deoxynucleotide triphosphate
DOL	degree of labeling
ECM	extracellular matrix
EDTA	ethylenediaminetetraacetic acid
EGF	epidermal growth factor
ELISA	enzyme linked immunosorbent assay
EMT	epithelial-mesenchymal transition
F2H	fluorescent two hybrid
FACS	fluorescence active cell sorting
FBS	fetal bovine serum
FGF	fibroblast growth factor
FPLC	fast flow liquid chromatography
FR	framework
FRAP	fluorescence recovery after photobleaching
GAPDH	glyceraldehyde 3-phosphate dehydrogenase
GBP	GFP binding protein
GFP	green fluorescent protein
GST	gluthatione S transferase
hcAb	heavy chain antibody
HIV	human immunodeficiency virus
HRP	horse radish peroxidase
IACT	intracellular capture technology
IALB	intensity above local background

ABBREVIATIONS

IC-IP	intracellular-immunoprecipitation
Ig, IgG	immunoglobulin G
IGF	insulin growth factor
IMAC	immobilized metal ion affinity chromatography
IPTG	isopropyl-beta-D-thiogalactopyranoside
J	joining
JAM	junctional adhesion molecule
LB	luria bertani
MET	mesenchymal epithelial transition
n	number of technical replicates
N	number of independent experiments
NB	nanobody
NES	nuclear export signal
NHS	N-hydroxysuccinimide
NLS	nuclear localization signal
NTA	nitrilotriacetic acid
OCLN	occludin
PAGE	polyacrylamid gel electrophoresis
PBS	phosphate buffered saline
PDGF	platelet-derived growth factor
PEG	polyethylenglycol
PMSF	phenylmethanesulfonylfluoride
RNA	ribonucleic acid
Rpm	rounds per minute
RTK	receptor tyrosine kinase
scFv	single chain variable fragment
sdAb	single domain antibody
SDS	sodium dodecylsulfate
TBS	tris buffered saline
TCF	T cell factor
TEMED	tetramethylethylenediamine
TF	transcription factor
TGF	transforming growth factor
V	variable
v/v	volume per volume
VAP	vascular adhesion molecule
V_H	variable domain of heavy chain
$V_H H$	variable domain of heavy-chain-only antibody
VIM	vimentin
V_L	variable domain of light chain
w/v	weight per volume
WFA	Withaferin A
wt	wildtype
Y2H	yeast two hybrid
ZO	*zona occludens*

VI

ZUSAMMENFASSUNG

Die epithelial-mesenchymale Transition (EMT) ist ein reversibler zellulärer Reprogrammierungsprozess, der ursprünglich während der Embryonalentwicklung auftritt. Im somatischen Gewebe ist der EMT-Prozess entscheidend an der Initiierung von Metastasen und Entwicklung von Tumoren beteiligt. Während des EMT-Prozesses verlieren einzelne Zellen eines Zellverbunds ihre epithelialen Eigenschaften, lösen sich von ihren Nachbarzellen ab und erlangen einen mesenchymalen Phänotyp mit hohem Migrations- und Invasionspotential. Die Aufklärung der molekularen Ursachen und die Erforschung neuer Möglichkeiten, gezielt in diesen Prozess einzugreifen, sind daher von besonderem Interesse für die Entwicklung neuer Behandlungsstrategien gegen die Bildung von Metastasen. Dabei dienen charakteristische epitheliale und mesenchymale Proteine, wie das Zellkontakt-Protein Occludin, das Aktin-Zytoskelett, der transkriptionale Repressor SNAI1 und das Intermediärfilament Vimentin als spezifische Biomarker oder sogar als Zielstrukturen für Wirkstoffe. Bis heute existiert noch kein Ansatz, diese endogenen Markerproteine in lebenden Zellen und in einem physiologischen Kontext zu untersuchen.

In dieser Arbeit wurden neue Einzeldomänen-Antikörper (Nanobodies) selektiert, um dynamische Veränderungen dieser EMT-Biomarker in Lebendzellsystemen biochemisch und optisch zu verfolgen. Nanobodies basieren auf der variablen Domäne von Schwere-Ketten-Antikörpern aus Kameliden und sind die kleinste, natürlich vorkommende antigenbindende Einheit. Für intrazelluläre Anwendungen werden Nanobodies an fluoreszierende Proteine fusioniert, wodurch sogenannte Chromobodies entstehen, die auf DNA-Ebene in Zellen eingebracht werden. Es wurden spezifische Nanobodies gegen Occludin, SNAI1 und Vimentin mittels der Phagen-Display-Technologie selektiert und ihre Bindeeigenschaften in biochemischen und zellbiologischen Analysen untersucht. Darauf basierend wurden stabile Zellsysteme mit einem Vimentin-spezifischen Chromobody sowie mit einem bereits beschriebenen Aktin-Chromobody hergestellt. Mittels *High-Content*-Mikroskopie konnten damit zum ersten Mal dynamische Veränderungen dieser endogenen Strukturkomponenten nach Induktion des EMT-Prozesses mit dem Wachstumsfaktor TGF-β detailliert beobachtet und quantifiziert werden. Abschließend wurden in einem Screeningsystem Zeit- und Dosis-abhängige Effekte nach Behandlung mit dem Vimentin-modifizierenden Wirkstoff Withaferin A bestimmt. Dieser hier beschriebene und vielseitig nutzbare Ansatz ermöglicht es nun die räumliche und zeitliche Organisation von relevanten EMT-Biomarkern detailliert in lebenden Zellen zu studieren. Damit ist ein Grundstein für neue Screeningtechnologien zur Findung von EMT-beeinflussenden Wirkstoffen mit antimetastasierender Wirkung gelegt.

ABSTRACT

The epithelial-mesenchymal transition (EMT) is a reversible cellular reprogramming process that originally occurs during embryonic development and is strongly involved in the initiation of metastases and cancer progression. During EMT, single cells of an epithelial layer lose their characteristic epithelial features, detach from their neighbor cells and acquire a mesenchymal phenotype with increased migratory and invasive potential. Targeting EMT is of particular interest for the development of novel compounds in the anti-metastatic cancer therapy. Thereby, certain epithelial and mesenchymal proteins, including the tight junction component occludin, the actin cytoskeleton, the transcriptional repressor SNAI1 and the intermediate filament vimentin, serve as specific biomarkers or even as target structures for compounds. To date, there is no approach available to study these endogenous markers in living cells in a physiological context.

In this thesis, novel single-domain antibodies (nanobodies) were selected to trace EMT biomarkers in a cancer-relevant living cell system. Nanobodies (~15 kDa), derived from heavy-chain-only antibodies of camelids, represent the smallest naturally occurring antigen binding reagent. For intracellular target visualization, they can be fused to fluorescent proteins (referred to as chromobodies) and introduced into cells on DNA level. Specific nanobodies against occludin, SNAI1 and vimentin were selected via the phage display technology and respective binding properties of nanobodies and chromobodies were analyzed in biochemical and cell biological assays. The vimentin specific and intracellular functional chromobody VB6-CB and a previously described chromobody specific for actin (Actin-CB) were stably introduced in cellular models. Based on the chromobody fluorescence, dynamic changes of endogenous actin and vimentin upon induction of EMT with the transforming growth factor β (TGF-β) were monitored and quantified for the first time by high-content-imaging. Moreover, by treatment with the vimentin modifying compound Withaferin A (WFA) time- and dose-dependent alterations of vimentin were observed and analyzed.

Taken together, this versatile approach allows detailed studies of the spatiotemporal organization of relevant EMT-biomarkers in living cells. This may provide the basis for novel screening technologies for anti-metastatic therapeutics affecting EMT.

1 INTRODUCTION

1.1 Epithelial-mesenchymal transition (EMT)

The epithelial-mesenchymal transition (EMT) is an evolutionarily conserved cellular reprogramming process during which epithelial cells lose many of their characteristic properties and acquire a mesenchymal phenotype (reviewed in Kalluri and Weinberg, 2009, and Thiery et al., 2009). In healthy tissues, epithelial cells are closely attached by cell-cell adhesion complexes, including tight junctions, adherens junctions, gap junctions and desmosomes (Knights et al., 2012). They are characterized by a polygonal cell shape and an apical-basal polarity. Forming coherent cell layers, epithelial cells face a luminal or external environment with their apical side and are separated from the extracellular matrix (ECM) via the basal lamina (Figure 1.1) (Thiery and Sleeman, 2006). Migration of epithelial cell is only possible within the epithelial layer. By contrast, mesenchymal cells are not organized in cell layers and only focally contact their neighbor cells. They are characterized by an elongated spindle-shaped morphology, a front-rear polarity and a high migratory potential (Hay, 2005). Moreover, mesenchymal cells are known to synthesize and organize components of the ECM, allowing them to migrate and invade into the underlying tissue (Nieto, 2013).
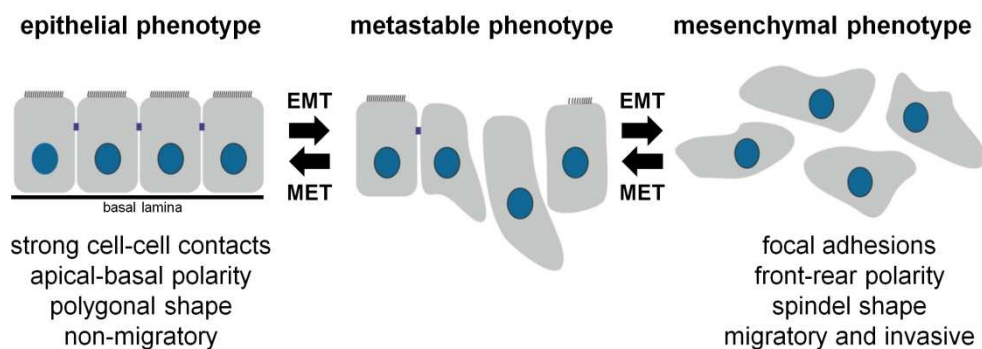
Figure 1.1: Epithelial-mesenchymal transition (EMT). The epithelial-mesenchymal transition (EMT) and its reverse process, the mesenchymal-epithelial transition (MET), allow cells to switch between an epithelial and a mesenchymal phenotype. While epithelial cells are characterized by strong cell-cell contacts, an apical-basal polarity and a polygonal cell shape, mesenchymal cells form only focal adhesions and exhibit a front-rear polarity as well as a fibroblast-like spindle shape (modified from Kalluri and Weinberg, 2009).

During EMT, single cells of the epithelial layer undergo a series of alterations in cell morphology, cytoarchitecture as well as cell migration and adhesion until they gain mesenchymal properties (Figure 1.1) (Lamouille et al., 2014). In some cases, cells can also undergo partial EMT, thereby acquiring a metastable state with epithelial as well as mesenchymal characteristics (Lee et al., 2006, Jordan et al., 2011). EMT-related mechanisms

as well as the reversed process, described as mesenchymal-epithelial transition (MET), are frequent events that occur during embryonic development, tissue regeneration and diseases such as organ fibrosis and tumor progression (Barriere et al., 2015).

1.1.1 EMT in development

In the 1960s, the epithelial-mesenchymal transition was first described by Elizabeth Hay, studying a model of the primitive streak during chick embryogenesis (Hay, 1968). Based on this pioneering work, it is known that the ability of cells to switch from an adherent epithelial phenotype into migratory mesenchymal cells is fundamental in early embryonic stages (Hay, 2005, Lim and Thiery, 2012). During the formation of the three germ layers (gastrulation), cells of a single epithelial layer (epiblast) undergo EMT to constitute mesoderm and endoderm, while cells that remain in the epiblast turn into the ectoderm (Acloque et al., 2009). Later on, EMT and MET processes are also involved in the generation of neural crest cells and their differentiation into derivates such as neurons, glial cells and pigment cells during the development of the nervous system (Dupin et al., 2007). Originating from the early mesoderm, several EMT and MET events, as well as the related process endothelial-mesenchymal transition (EndMT) are required for the morphogenesis of tissues and whole organs, such as pancreas, liver and heart (Johansson and Grapin-Botton, 2002, Tanimizu and Miyajima, 2007, Timmerman et al., 2004). Generally, EMT processes during development are classified as Type 1 EMT (Kalluri and Weinberg, 2009).

1.1.2 EMT in tissue regeneration and organ fibrosis

In adults, processes of Type 2 EMT occur during wound healing. In case of an injury, keratinocytes are activated in response to inflammatory cytokines and undergo partial EMT that allows them to spread and migrate within loose cell-cell adhesions (Arnoux et al., 2008, Yan et al., 2010). However, Type 2 EMT does not only occur in healthy organisms, but is also linked to pathological events, including fibrotic diseases of the liver, kidney, heart and lung (Kalluri and Neilson, 2003). Permanent injuries, such as chronic inflammation, promote ongoing EMT processes. This leads to an increased number of myofibroblasts that arise through EMT and secrete an excessive amount of collagen and other ECM components, resulting in a complete loss of organ function (Liu, 2004, Zeisberg et al., 2007).

1.1.3 EMT in cancer progression

During the last decade, activation of the EMT program has been linked to critical mechanisms in tumor progression, development of circulating tumor cells (CTCs) and metastasis formation (De Craene and Berx, 2013, Barriere et al., 2015). While excessive cell

proliferation and angiogenesis are early events in the progression of epithelial cancers, EMT type 3 processes occur in advanced stages during cancer cell dissemination (Thiery and Lim, 2013). Thereby, single cells originating from primary tumors invade the surrounding tissue and metastasize to distant parts of the body. Epithelial cells that underwent full or partial EMT show an increased resistance to anoikis (Kim et al., 2012) and can cross the ECM to intravasate blood vessels (Nieto, Yu et al., 2013). In this context, it has been shown that certain populations of circulating tumors cells (CTCs) that underwent EMT present properties of migratory cancer stem cells (CSCs), such as self-renewal and the capacity to grow into secondary tumors (Mani et al., 2008), while in other populations, referred as stationary CSCs, stemness properties are suppressed (Ocana et al., 2012, Nieto, 2013, Jung and Yang, 2015). For extravasation and colonization processes of micro- and macrometastases mesenchymal-epithelial transition (MET) processes occur (Chang et al., 2013). This is reflected by high histological similarities between primary and secondary tumors and is consistent with studies, describing mesenchymal-like cells that re-acquire epithelial characteristics but continue to maintain mesenchymal properties, referred as metastable phenotype (Brabletz et al., 2001, Lee et al., 2006, Jordan et al., 2011).

The emerging role of EMT during tumor progression and metastatic development turns it into an attractive target for cancer therapy (reviewed in Davis et al., 2014). In this regard, important EMT marker proteins as well as signaling pathways are of particular interest and will be described in the following sections of the introduction.

1.2 EMT marker proteins

A hallmark of EMT is the change in expression of epithelial and mesenchymal marker proteins (Figure 1.2) (Kalluri and Weinberg, 2009). Most of the epithelial markers are components of junctional complexes: occludin, claudin and zona occludens (ZO) 1-3 are tight junction proteins, while E-cadherin is implicated in adherens junctions and linked to cortical actin via catenins, and cytokeratins are connected to the desmosoms via desmoplakin (Knights et al., 2012, Lamouille et al., 2014). Triggered through extracellular activators such as growth factors and components of the ECM, the expression of so-called EMT transcription factors (TFs), including SNAI1, SNAI2, TWIST, ZEB and others is increased (Peinado et al., 2007). EMT-TFs regulate EMT-relevant gene expression and act as transcriptional repressors of epithelial marker proteins. Along with the loss of epithelial markers, the expression of mesenchymal markers such as N-cadherin, vimentin and fibronectin is increased. This is accompanied by extensive changes in the organization of the actin cytoskeleton, leading to

enhanced cellular motility (Thiery and Sleeman, 2006, Lamouille et al., 2014). Metastable cells that underwent only partial EMT were shown to express epithelial as well as mesenchymal marker proteins (Jordan et al., 2011). The following sections provide a detailed description of four fundamental EMT markers occludin, actin, SNAI1 and vimentin.
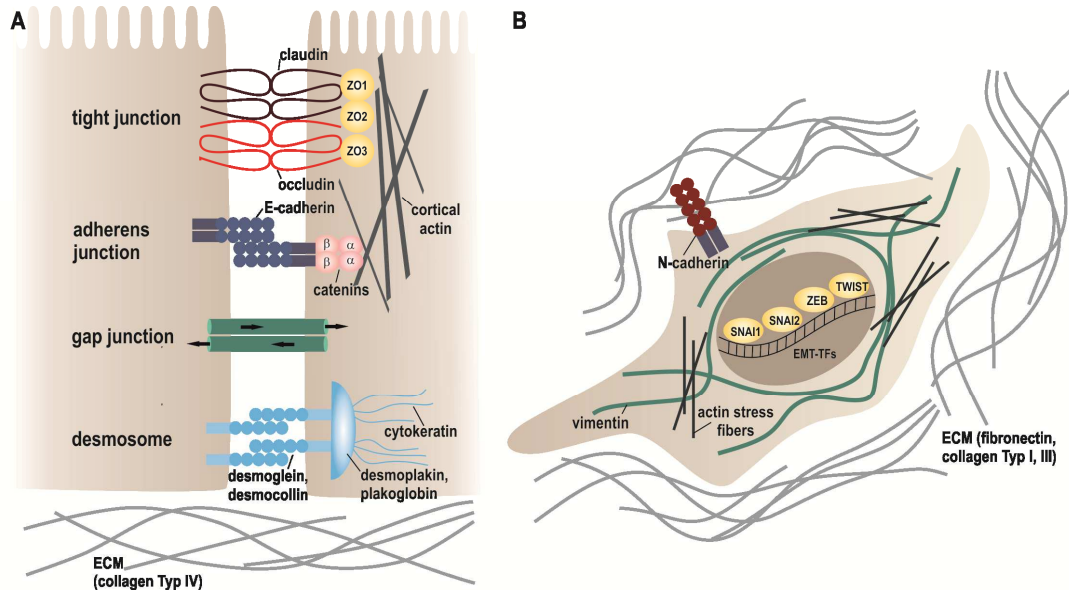
Figure 1.2: Epithelial and mesenchymal markers. (**A**) Epithelial cell with cell junctions and characteristic marker proteins. Epithelial markers comprise the tight junction proteins occludin, claudin, ZO1-3, the adherens junction component E-cadherin, which is connected to cortical actin via β-catenin and α-catenin, the desmosoms associated protein desmoplakin and the intermediate filament cytokeratin. (**B**) Mesenchymal cell and characteristic marker proteins. Mesenchymal markers comprise N-cadherin, the transcription factors SNAI1, SNAI2, ZEB and TWIST, the cytoskeletal elements vimentin and actin stress fibers, as well as the ECM component fibronectin (modified from Lamouille, 2014).

1.2.1 Occludin

Together with other transmembrane linker proteins (e.g. claudins, JAM) and cytoplasmic adaptor proteins (e.g. ZO1-3, vinculin, and cingulin), occludin is an essential component of cellular tight junctions at the apical side of epithelial and endothelial cells (reviewed in Niessen, 2007). The occludin monomer (~65 kDa) consists of a cytoplasmic N- and C-terminus, four transmembrane domains as well as one small intracellular and two extracellular loops (Figure 1.2) (Furuse et al., 1993). The extracellular loops have been shown to be required for cell-cell interactions, while the N- and C- termini are involved in the sealing and barrier function of tight junctions (Chen et al., 1997, Bamforth et al., 1999). Moreover, the extended C-terminal domain interacts with a number of cytoplasmic proteins, including ZO1-3 (Fanning et al., 1998, Itoh et al., 1999, Haskins et al., 1998), junctional adhesion molecule (JAM) (Bazzoni et al., 2000), and vascular adhesion molecule (VAP)-33 (Lapierre et al.,

1999). It is also essential for the dimerization of occludin and was shown to mediate signal transduction (reviewed in Feldman et al., 2005). Regulation of occludin is highly depending on its phosphorylation state: In intact epithelial cells occludin is extensively phosphorylated on Ser and Thr residues, whereas phosphorylation on Tyr residues has been linked to disruption of the tight junctions (Ando-Akatsuka et al., 1996, Raleigh et al., 2011). Since occludin is involved in epithelial adhesion, migration and apoptosis, deregulation of occludin has been associated with diseases such as viral and bacterial infections, inflammatory diseases and tumor progression (Du et al., 2010, Cummins, 2012, Beeman et al., 2012). Decreased occludin levels were found to be a frequent event in a variety of epithelial tumors (Tobioka et al., 2004, Orban et al., 2008, Martin et al., 2010). During EMT, occludin gene expression is repressed by the EMT-TFs SNAI1, SNAI2, TWIST and FoxF1, leading to a tight junction collapse, accompanied by the loss of the epithelial barrier function (Peinado et al., 2007, Yang et al., 2010, Nilsson et al., 2010).

1.2.2 Actin

Microfilaments, consisting of the 42 kDa protein actin, microtubules and intermediate filaments are the three major components of the cytoskeleton. The actin monomer is a globular protein (G-actin) that is able to polymerize into filamentous actin (F-actin) upon regulation through ATP hydrolysis and a number of actin binding proteins, particularly profilin and cofilin (Dominguez and Holmes, 2011). Actin organization is critically involved in migration and invasion of metastatic cancer cells (Yamaguchi and Condeelis, 2007, Ridley, 2011). In epithelial cells, actin filaments are organized in thin cortical bundles linked to the plasma membrane. They are tightly connected to the adherens junctions via α-catenin and β-catenin and to the tight junctions via interaction with the ZO proteins (Niessen, 2007). Hence, changes in the arrangement of cellular junctions dramatically affect the organization of the actin cytoskeleton in epithelial cells. In mesenchymal cells, actin filaments are typically reorganized into thick contractile stress fibers at the ventral cell surface (Godoy et al., 2009, Haynes et al., 2011, Lamouille et al., 2014). During EMT, actin remodeling is controlled by the Rho small GTPases family, including RhoA, Rac and Cdc42, which mediate the formation of actin stress fibers, lamelopodia and filopodia (Woodham and Machesky, 2014, Morris and Machesky, 2015). In this context, increased expression of the actin regulating proteins Arp2/3 and WAVE2 has been reported to correlate with poor prognosis in breast and liver carcinomas (Iwaya et al., 2007). A recent study also suggests that actin reorganization may appear as an upstream regulator of EMT in metastatic cancer cells (Shankar and Nabi, 2015).

1.2.3 SNAI1

As mentioned above, SNAI1 is a mesenchymal marker protein and belongs to the so-called EMT-TFs. SNAI1 (Snail), SNAI2 (Slug) and SNAI3 (Smuc) constitute the Snail family of transcriptional repressors, all comprising a highly conserved C-terminal DNA binding domain with four to six C_2H_2 zinc fingers (Nieto, 2002). The N-terminal SNAG domain of SNAI1 and SNAI2 is responsible for their repressor capacity, while the central domains are highly diverse. SNAI1 comprises a Ser/Pro rich domain, a so-called destruction box domain as well as a nuclear export signal (NES) (Peinado et al., 2007, Wang et al., 2013b). Posttranslational modifications within these regions regulate subcellular localization, protein stability and repressor activity of SNAI1 (Wu et al., 2009b, Vinas-Castells et al., 2010). In particular, phosphorylation of the NES and destruction box domain by GSK3β has been reported to mediate ubiquitin-dependent degradation of SNAI1 (Zhou et al., 2004, Zheng et al., 2013). Most importantly, SNAI1 has been shown to repress the expression of many EMT related target genes, including the epithelial markers E-cadherin, occludin, cytokeratin 17 and 18, claudins and collagen2α1 (Peinado et al., 2007, Lamouille et al., 2014). The mechanism of SNAI1-mediated transcriptional repression was proposed to occur via complex formation with the co-repressor Sin3A and HDAC1/2 (Peinado et al., 2004). Interestingly, SNAI1 also binds to its own promoter, thereby autoregulating its expression (Peiro et al., 2006). Being involved in many EMT regulating signaling pathways (see also section 1.3), SNAI1 plays a critical role in the development of tumor metastasis (Kaufhold and Bonavida, 2014). Recently, it has been reported to contribute to drug resistance and a CSC-like phenotype in metastasizing pancreatic cancer and lung cancer (Zhou et al., 2014, Wang et al., 2014).

1.2.4 Vimentin

One of the most frequently described mesenchymal EMT markers is the 54 kDa protein vimentin. Together with desmin and GFAP, vimentin belongs to the type III class of intermediate filaments and is a major cytoskeletal component of mesenchymal cells, which is mainly involved in tissue integrity and cytoarchitecture (reviewed in Herrmann et al., 2007). The evolutionarily highly conserved protein generally consists of three domains. The N-terminal head domain (aa 1 - 95) is required for vimentin assembly, depending on posttranslational modifications (Sihag et al., 2007). The central helical rod domain (aa 96 – 407) includes three α-helices (coil 1A, 1B and coil 2) which are connected by two linkers (L1 and L12). Finally, the C-terminal tail domain (aa 408 – 488) is essential for the radial compaction and width control of extended filaments (Chernyatina et al., 2012, Herrmann et al., 1996). Assembly and disassembly of vimentin filaments are tightly regulated by the

interplay of numerous kinases that are involved in cell division and migration (Sihag et al., 2007). When dephosphorylated, soluble tetrameric vimentin units self-assemble by lateral association into unit length filaments (ULFs), which anneal longitudinally into higher-order filamentous structures with an approximate thickness of 10 nm after radial compaction (Kirmse et al., 2007). Phosphorylation of vimentin Ser/Thr residues, typically located in the head or tail domain induce vimentin disassembly (Sihag et al., 2007, Snider and Omary, 2014). Vimentin is involved in a number of signaling pathways mediating apoptosis (Byun et al., 2001, Burikhanov et al., 2014), cell migration and invasion (Zhu et al., 2011, Vuoriluoto et al., 2011, Havel et al., 2014). In the context of EMT, ectopic expression of vimentin *in cellulo* has been shown to induce mesenchymal-like cell features (Mendez et al., 2010). Moreover, overexpression of vimentin has been shown to correlate with increased formation of metastases, reduced patient survival and poor prognosis across multiple epithelial cancers, including lung, breast and gastrointestinal tumors (Otsuki et al., 2011, Yamashita et al., 2013, Dauphin et al., 2013).

1.3 EMT signaling

EMT signaling is mediated by various intrinsic factors (e.g. kinases, transcription factors) as well as extrinsic stimuli from the local microenviroment, including growth factors, cytokines, hypoxia and components of the ECM. Thereby the transforming growth factor β (TGF-β) pathway represents the main signaling mechanism. Other pathways involved in EMT constitute receptor tyrosine kinase (RTK), Wnt, Notch, and Hedgehog signaling. All of them activate intracellular kinase cascades that induce EMT-TFs, triggering the repression of epithelial markers and induction of mesenchymal markers (reviewed in Lamouille et al., 2014, Gonzalez and Medici, 2014).

1.3.1 TGF-β-dependent signaling

TGF-β signaling can be activated by three isoforms of TGF-β (TGF-β1, TGF-β2 and TGF-β3) as well as by the bone morphogenic proteins (BMP2-7). Thereby, TGF-β1 is best described in cancer-related EMT signaling (Xu et al., 2009). Ligand binding to the heterotetrameric receptor complex, consisting of TGF-β receptor I (TGF-βRI) and TGF-βRII components, leads to phosphorylation of TGF-βRI by the Ser/Thr kinase activity of TGF-βRII. Subsequently, the transcription factors SMAD2/3 are recruited to the Gly/Ser rich domain of TGF-βRI, followed by phosphorylation of the C-terminal domain of SMAD2/3 which induces complex formation with the transcriptional co-activator SMAD4 (Feng and Derynck, 2005, Gonzalez and Medici, 2014). This SMAD2/3 and SMAD 4 complex translocates into the

nucleus via binding to importins (Yao et al., 2008). Inside the nucleus, the SMAD complex induces the transcription of EMT-TFs directly, by binding to the promoter of SNAI1, ZEB and other EMT-related genes (Vincent et al., 2009). SMAD-dependent TGF-β signaling is negatively regulated by the inhibitory SMAD6 and SMAD7 through interference with SMAD2/3 phosphorylation by TGF-βRI (Imamura et al., 1997, Nakao et al., 1997), as well as by proteasomal degradation mediated by SMAD ubiquitin regulatory factors (Smurfs) (reviewed in Izzi and Attisano, 2004). In addition, TGF-β signaling also induces EMT through a SMAD-dependent activation of the PI3K-Akt pathway, leading to GSK3β inhibition and increased nuclear β-catenin and SNAI1 levels (Medici et al., 2006).
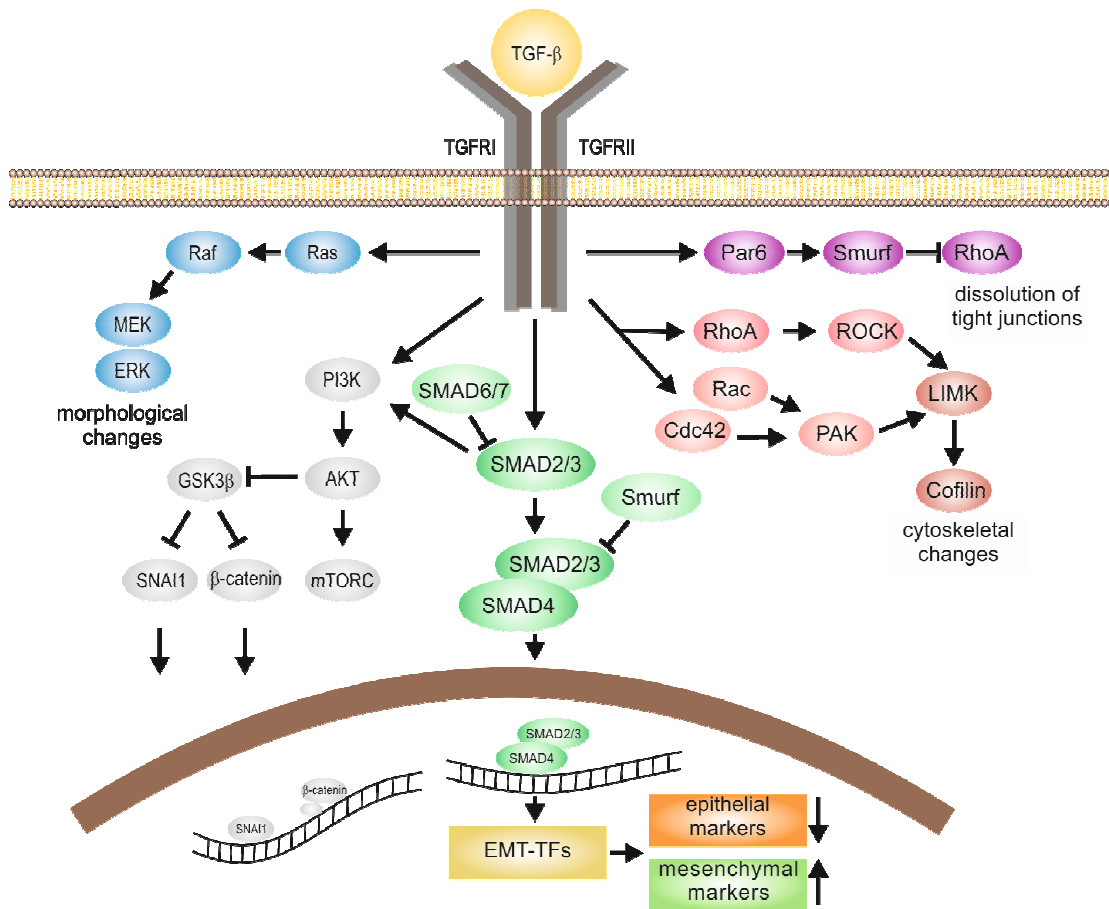
Figure 1.3: Molecular mechanisms of TGF-β induced EMT. Binding of TGF-β to the TGF-β receptor complex leads to activation of SMAD 2/3, that form complexes with SMAD 4 which activate the transcription of EMT-TFs, resulting in the repression of the expression of epithelial markers and activation of the expression of mesenchymal markers. SMAD2/3-dependent signaling can be inhibited by SMAD 6/7 and Smurf. TGF-β mediated activation of the Rho family induces cytoskeletal changes, while RhoA inhibition via Par6 and Smurf leads to the disruption of the tight junctions. TGF-β further induces the Erk MAPK pathway and activates PI3K signaling leading to the activation of Akt and mTORC and to increased nuclear β-catenin and SNAI1 levels through Akt-dependent inhibition of GSK-3β.

Alongside SMAD-dependent signaling, TGF-β is also potent as an activator of non-SMAD pathways, such as signaling through Rho GTPases (RhoA, Rac and Cdc42) to regulate the actin cytoskeleton (Ridley, 2011). Moreover, ubiquitinylation of RhoA via TGF-βRI-dependent phosphorylation of Par6 and activation of Smurf1 induces proteasomal degradation of RhoA and disruption of the tight junctions (Ozdamar et al., 2005). Since TGF-β receptors were shown to have a low Tyr phosphorylation activity next to their Ser/Thr phosphorylation activity, they can also directly activate the PI3K-Akt and MAPK pathways. TGF-β-mediated activation of the PI3K-Akt pathway during EMT leads to an increase in cell size, protein synthesis, motility and invasion mediated through mTOR signaling (Lamouille et al., 2012). Activation of ERK/MAPK signaling cascades have been shown to contribute to a decreased E-cadherin expression and increased expression of fibronectin and vimentin (Xie et al., 2004, Yu et al., 2002).

1.3.2 TGF-β-independent signaling

In addition to TGF-β-dependent signaling, EMT can be induced by a number of other growth factors, including epidermal growth factor (EGF), fibroblast growth factor (FGF), platelet-derived growth factor (PDGF) and insulin growth factor (IGF). All of them stimulate receptor tyrosine kinases (RTKs) that activate signaling pathways mediated by PI3K-Akt, Src and Ras and induce expression of the EMT-TFs (Lemmon and Schlessinger, 2010, Lamouille et al., 2014). Inhibition of GSK3β during Wnt signaling contributes to an increased SNAI1 stability and promotes nuclear accumulation of β-catenin, which activates the transcription factor LEF1 and induces the expression of SNAI1, SNAI2, TWIST and other EMT-related genes (Yook et al., 2006, Fodde and Brabletz, 2007). Moreover, Notch signaling has been shown to activate SNAI1 expression directly and indirectly through induction of hypoxia-inducible factor 1α (HIF-1α) as well as through crosstalk with Wnt, ERK and NF-κB signaling (Miele et al., 2006, Sahlgren et al., 2008). Eventually, Hedgehog signaling induces the expression of EMT-related genes through activation of Gli transcription factors (Li et al., 2006).

1.4 EMT targeting therapeutics

Due to the prominent role of EMT in the development of cancer metastases, the dynamic transition process and its related marker proteins are of particular therapeutic interest (Davis et al., 2014). Moreover, EMT has been associated with the acquisition of therapy resistance, regarding radiation, chemotherapy and small molecule-targeted therapies. For example, resistance to gefitinib and ertolinib in non-small lung cancer cells, or resistance to 5-fluorouracil in breast cancer cells correlates with the acquisition of a mesenchymal phenotype

INTRODUCTION

(Yauch et al., 2005, Zhang et al., 2012). In the development of EMT-targeting pharmaceutics different strategies address (i) the inhibition of extrinsic signals (e.g. TGF-β, EGF) or intrinsic signals (signaling pathway components, e.g. TGF-βRI), (ii) the MET process or (iii) direct targeting of mesenchymal EMT markers (e.g. vimentin, SNAI1) (Davis et al., 2014). The majority of EMT-interfering compounds that are currently investigated in clinical trials, focus on classic drug targets, including receptors, enzymes and transporter proteins (Rask-Andersen et al., 2011). One example is the small molecule and selective inhibitor of TGF-βRI, LY2157299, which is currently tested in a number of phase I-IV clinical trials for its application in hepatocarcinoma, pancreatic cancer and malignant glioma (Kothari et al., 2014, Pasquier et al., 2015).

Few compounds have been identified to directly target mesenchymal EMT biomarkers. N-cadherin can be blocked by a specific peptide (named ADH-1) to prevent tumor progression in pancreatic cancer mice models and has been addressed by a neutralizing antibody to treat myeloma (Shintani et al., 2008, Sadler et al., 2013). Certain dietary and herbal chemopreventive agents, such as resveratrol, 2-hydroxycinnamaldehyde and curcumin are discussed to inhibit EMT via SNAI1-dependent mechanisms (Wang et al., 2013a, Ismail et al., 2013, Huang et al., 2013). The role of vimentin in EMT and tumor progression turns it into an attractive target for cancer therapy (Satelli and Li, 2011). Direct targeting of vimentin by Withaferin A (WFA) has been shown to reduced tumor growth and metastatic spread breast cancer in mice models through inhibition of EMT (Bargagna-Mohan et al., 2007, Yang et al., 2013). Moreover, other compounds such as silibinin or arylquins negatively regulate vimentin resulting in reduced migration and invasiveness or induction of apoptosis in cancer cells (Wu et al., 2009a, Burikhanov et al., 2014).

Currently, most primary screening technologies for EMT-targeting drug discovery at academic institutions rely on cell-based assays and include assay readouts that are mainly based on fluorescence intensity, glow luminescence, and high-content imaging (Comley, 2014, Gupta et al., 2009, Aref et al., 2013). Thereby, antibody-mediated techniques serve as powerful tools to detect prognostic biomarkers, but they are restricted to endpoints experiments and provide no information about dynamic processes. For real-time analyses, ectopic expression of fluorescently labeled EMT markers has been employed (Suzuki et al., 2009, Zhou et al., 2004, Chang et al., 2009, Kajita et al., 2014). However, ectopic expression of the mesenchymal markers SNAI1 and vimentin effect cell shape, motility and invasion or even induces EMT and therefore does not reflect the distribution and dynamic organization of endogenous proteins (Peinado et al., 2004, Moreno-Bueno et al., 2009, Mendez et al., 2010).

12

Based on the importance of EMT markers as prognostic factors and molecular targets for anti-metastatic cancer therapy, there is an ongoing demand for novel strategies to study EMT and its related biomarkers on endogenous levels and in disease-relevant models.

1.5 Intracellular affinity reagents (Intrabodies)

Intracellular affinity reagents have been established to overcome distinct limitations of conventional techniques to investigate spatial and temporal dynamics of cellular structures. Antibodies are valuable tools for innumerable applications, including Western blot, ELISA, mass spectrometry, immunofluorescence etc. However, due to their large size and improper folding in the reducing environment of the cytoplasm, antibody-based detection of endogenous proteins is restricted to fixed and permeabilized samples and does not allow tracing of dynamic processes in living cells. Fluorescent fusion proteins are widely used for live cell imaging of dynamic protein localization, but e.g. posttranslational modifications remain invisible and fusion of large protein tags, including eGFP or mCherry to N- or C-termini can lead to protein mislocalization (Stadler et al., 2013). During the last decades a number of recombinant antibody-derived formats as well as non-antibody structures have been developed, which combine the advantages of antibodies and fluorescent fusion proteins and provide new opportunities to track and manipulate intracellular target structures (Kaiser et al., 2014, Helma et al., 2015).

1.5.1 Non-immunoglobulin scaffolds

Recombinant binding reagents, based on the tenth domain of type III fibronectin (also referred to as monobody), have been described to functionally address intracellular targets, since the fibronectin structure does not depend on intramolecular disulfide bonds (Koide et al., 1998, Gross et al., 2013). Anticalins, derived from lipocalins, are considered to be well suited for targeting of small molecules and conformational epitopes *in vitro* as well as in living cells (Eggenstein et al., 2014, Terwisscha van Scheltinga et al., 2014). The designed ankyrin repeat proteins (DARPins) are the most prominent example for so-called repeat proteins. Containing neither disulfide bridges nor free cysteines, DARPins have been shown to modulate particular enzymes in living cells (Kummer et al., 2012, Pluckthun, 2015). In addition to protein scaffolds, small peptides such as lifeact (17 amino acids), derived from the actin-binding protein (Abp 140), are available for live cell visualization (Riedl et al., 2008, Riedl et al., 2010). Finally, aptamers, consisting of ssDNA or RNA were found to specifically recognize target molecules and serve as intracellular affinity reagents (Kunz et al., 2006, Meyer et al., 2011).

Non Ig-Scaffolds   **Ig-Scaffolds**
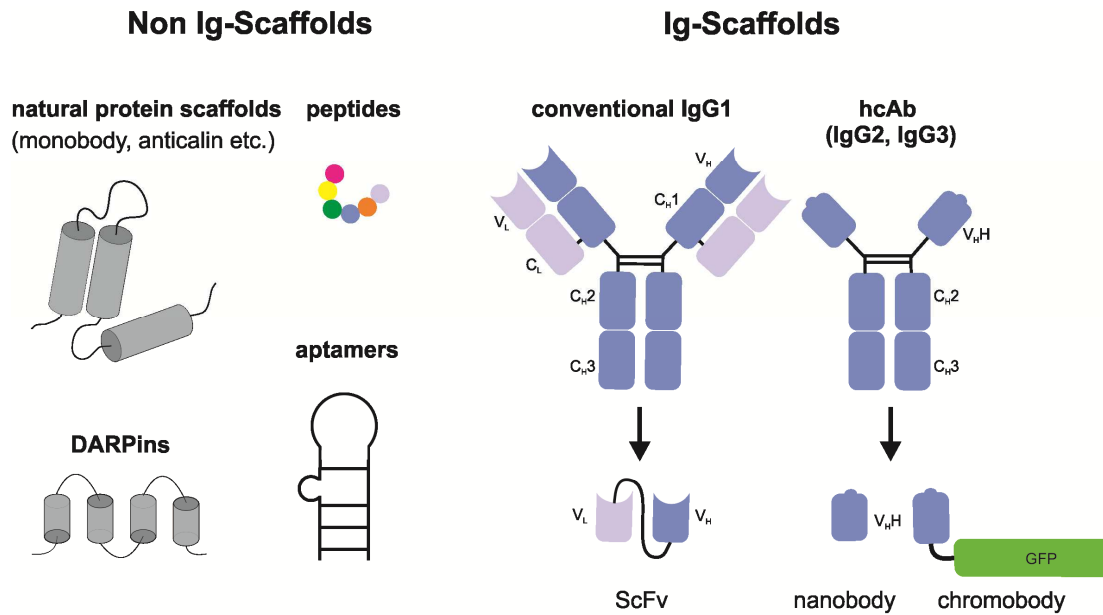
Figure 1.4: Schematic overview of intrabody formats. Intracellular binding reagents such as monobodies and anticalins are derived from naturally occurring non-immunoglobulin structures (Non-Ig scaffolds). Moreover, peptides, designed ankyrin repeat proteins (DARPins) and DNA or RNA aptamers serve as intrabodies. The most commonly IgG-derived intrabody format (Ig-Scaffolds) is the scFv, consisting of a variable heavy and light chain (V_H and V_L), connected by a peptide linker. In some cases single V_H or V_L domains are applied as intrabodies. The V_HH domain (nanobody) is derived from camelid heavy-chain-only antibodies (hcAbs). For fluorescence imaging, the V_HH domain can be fused to fluorescent proteins, resulting in chromobodies.

1.5.2 Immunoglobulin G scaffolds

The Immunoglobulin G (IgG) is the antibody format most commonly used in research and consists of two heavy chains and two light chains, each comprising a variable domain (V_H or V_L respectively). Antigen binding is mediated by six complementary determining regions (CDRs), three of which are located in the V_H and three in the V_L domain (Davies and Metzger, 1983). For intracellular applications, single chain variable fragments (scFvs, ~25 kDa) have been generated by directly connecting the V_H and V_L domain via a flexible peptide linker, typically comprising $(Gly_4/Ser)_{2-4}$ repeats (Bird et al., 1988, Toleikis et al., 2004). However, due to hydrophobic residues on the surface of V_Hs and V_Ls, intracellular expression of these constructs often results in reduced solubility, improper folding and aggregation (Biocca et al., 1990, Cattaneo and Biocca, 1999). More recently, individual studies described modified and fluorescently labeled scFvs for live cell imaging e. g. of α-tubulin (Cassimeris et al., 2013), to trace posttranslational modifications of histones in living cells (Sato et al., 2013a) or for super resolution microscopy (Szent-Gyorgyi et al., 2008, Yates et al., 2013). In addition, few examples of single V_H or V_L domains derived from IgGs have been applied as intrabodies (Colby et al., 2004, Sato et al., 2013a).

1.6 Nanobodies

Currently, the smallest antigen binding reagents based on immunoglobulin fold are single domain antibodies (sdAbs, also referred as nanobodies), derived from heavy-chain-only antibodies (hcAbs) of *Camelidae* (reviewed in Muyldermans, 2013).

1.6.1 Derivation and structure of nanobodies

In addition to the conventional IgG1 (~ 150 kDa) in the serum of camelids (*Vicugna pacos, Camelus bactrianus, Camelus dromedarus* and *Llama glama*) heavy-chain-only antibodies (hcAbs, IgG2 and IgG3, ~ 90 kDa) were discovered (Hamers-Casterman et al., 1993). Other naturally occurring antibodies devoid of light chains were found in cartilaginous fish, including nurse shark (*Ginglymostoma cirratum*), wobbegong and spotted ratfish (*Hydrolagus colliei*) and are called immunoglobulin new antigen receptors (IgNARs) (Greenberg et al., 1995, Rast et al., 1998, Nuttall et al., 2001). hcAbs consist of two identical heavy chains that, unlike heavy chains of conventional IgG1s, comprise only two constant domains (C_H2 and C_H3, but no C_H1), a hinge region and a variable domain (V_HH). Notably, the hinge region of IgG2 is longer than the one of the IgG3 isotype (Woolven et al., 1999). Loss of the C_H1 domain appears through a G-to-A point mutation that provokes the elimination of the C_H1 region by splicing (Nguyen et al., 1999). Consequently, this prevents interaction with the constant region of the light chain (C_L), mediated by C_H1 in IgG1 (Davies and Metzger, 1983).

Devoid of light chains, antigen binding of hcAbs is mediated by the V_HH domain only, resulting in a number of characteristic adaptations. Both V_H and V_HH domains consist of four conserved framework regions (FR1-FR4) linked by three hypervariable CDRs and stabilized by a canonical disulfide bridge between FR1 and FR3 (Cys23-Cys94) and a conserved Trp103 in FR4 (Muyldermans et al., 1994, Desmyter et al., 1996). However, in FR2 the highly conserved hydrophobic residues at the positions Val37, Gly44, Leu45 and Trp47 of the V_H domain are substituted by the more hydrophilic residues Phe/Tyr37, Glu/Gln44, Arg45 and Gly/Phe/Leu47 in the V_HH domain (Kabat and Wu, 1991, Vu et al., 1997, Barthelemy et al., 2008). These changes lead to an increased hydrophilicity of the former light chain interface and a high overall solubility of the V_HH domain (Conrath et al., 2005). Consequently, heavy chains of sdAbs do not associate with the chaperone protein BiP (binding immunoglobulin protein) and escape from the endoplasmic reticulum (Nguyen et al., 2002). Notwithstanding the reduced combinatorial diversity, hcAbs can compete with conventional IgGs regarding their affinities. This may be explained by somatic diversification mechanisms, including hypermutations of single nucleotides, oligonucleotide insertions and

deletions, and gene replacements (Nguyen et al., 2000, Conrath et al., 2003). Many but not all V$_H$H domains exhibit an elongated CDR3 that compensates the loss of three CDRs of the light chain. This extended loop is often stabilized by an additional disulfide bridge between CDR3 and CDR1 (Muyldermans et al., 1994, Desmyter et al., 1996). Commonly, V$_H$H paratopes are thought to form convex structures that bind to cavities like e.g. active sites of enzymes. (De Genst et al., 2006, Jobling et al., 2003). However, some studies have also described V$_H$H domains recognizing small peptides (Klooster et al., 2009, Traenkle et al., 2015).
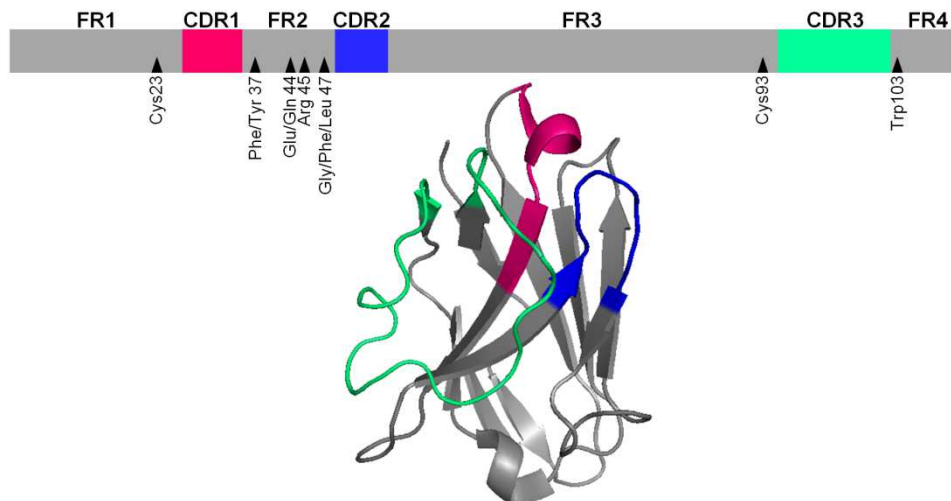
Figure 1.5: V$_H$H structure. The V$_H$H domain consists of four frame work regions (FR1-FR4) and three complementary determining regions (CDR1-CDR3) that are responsible for antigen binding. Highly conserved residues in the framework regions are Cys23 in FR1 that forms a disulfide bridge with Cys93 in FR3, and Trp103 in FR4. The characteristic hallmark residues Phe/Tyr37, Glu/Gln44, Arg45 and Gly/Phe/Leu47 in FR2 provide increased hydrophilicity and overall solubility of the molecule (modified from Muyldermans, 2013).

1.6.2 Nanobody applications in research

Without neglecting the emerging role of nanobodies for therapeutic and diagnostic approaches, nanobodies are attractive tools for various applications in biochemical and cell biological research (reviewed in De Meyer et al., 2014). Most important technological advantages include their small size (~ 13 – 15 kDa, ~ 2 x 4 nm) and the high solubility and stability regarding salt, temperature and pH conditions (Barthelemy et al., 2008, Rothbauer et al., 2008). Moreover, nanobodies comprise only one single domain that can be easily cloned and efficiently expressed in bacterial as well as in mammalian cell systems (Harmsen and De Haard, 2007). Finally, specific nanobodies with comparable affinities to scFv constructs can be readily selected using common screening technologies, such as phage display (Arbabi Ghahroudi et al., 1997, Harmsen and De Haard, 2007, Pardon et al., 2014).

Nanobodies have been immobilized on numerous kinds of matrices, including agarose, magnetic particles, and multi-well plates. Due to the efficient production at low costs and

16

their good regeneration capacity, they are highly attractive for immunoaffinity purification of endogenous proteins (Klooster et al., 2007). Nanobody-mediated precipitation of ectopically expressed or endogenous targets has been performed to analyze protein-protein interactions (Rothbauer et al., 2008, Traenkle et al., 2015), as well as interactions between proteins and DNA by chromatin immunoprecipitation (ChIP) (Nguyen-Duc et al., 2013). For sensitive detection of target proteins in complex samples nanobody-based sandwich immunoassays have been developed (Zhu et al., 2014). Due to their smaller size compared to conventional antibodies, a closer spatial proximity of the fluorophore and the target structure can be achieved by immunostaining with fluorescently labeled nanobodies, which has been exploited for super resolution microscopy (Ries et al., 2012). Moreover nanobodies have been applied to facilitate structural analyses by x-ray crystallography, since they can stabilize crystallization of membrane proteins or large protein complexes (Rasmussen et al., 2011, Abskharon et al., 2014, Pardon et al., 2014).

Most importantly nanobodies are well suited to modulate and trace intracellular target structures within living cells. Intramolecular disulfide bridges are not necessarily required for correct nanobody folding, allowing efficient expression of functional nanobodies even in the reducing environment of the cytoplasm. Intracellular expressed nanobodies (intrabodies) have been applied to affect enzyme activity (Lauwereys et al., 1998, Jobling et al., 2003), to induce conformational changes (Kirchhofer et al., 2010), to trigger targeted protein degradation (Caussinus et al., 2012), to manipulate genes in individual cells (Tang et al., 2013), and to trace endogenous protein localization in living cells and whole organisms as so-called chromobodies (Rothbauer et al., 2006, Burgess et al., 2012, Helma et al., 2012a, Panza et al., 2015, Traenkle et al., 2015). Chromobodies are chimeric fusion proteins consisting of a nanobody moiety and a fluorescent protein e.g. the green fluorescent protein (GFP) (Chalfie et al., 1994, Tsien, 1998). The first described and most prominent chromobody example is the red fluorescent GFP-chromobody that has been shown to co-localize with and trace dynamic changes of GFP-labeled proteins, independently of the subcellular compartment (Rothbauer et al., 2006, Schornack et al., 2009). Other chromobodies have been developed to visualize the nuclear lamina and monitor apoptosis (lamin-chromobody), to follow the progression of the cell cycle (PCNA-chromobody) or to address non-endogenous targets such as morphogenesis of HIV (Zolghadr et al., 2012, Burgess et al., 2012, Helma et al., 2012b). Recently, a chromobody specific for the Wnt signaling component β-catenin has been applied for high content imaging (Traenkle et al., 2015).

1.7 Aims and objectives

The reversible cellular reprogramming process epithelial-mesenchymal transition (EMT) plays an emerging role for the development of novel anti-metastatic therapeutics. Hence, there is ongoing need for novel techniques to study EMT and its related biomarkers at an endogenous level in disease-relevant models. Overcoming the drawbacks of conventional antibodies and expression of ectopic fusion proteins, the chromobody technology allows tracking of endogenous biomarkers in living cells, without affection cell viability and function of the target protein.

The aim of this work was, to develop chromobody-based cellular models, to monitor and quantify dynamic changes during the process of EMT by high content imaging, thereby providing the basis for novel screening approaches to identify EMT affecting compounds. This requires the selection of camelid-derived single domain antibodies (nanobodies) against significant EMT markers followed by detailed biochemical and cell biological characterization of nanobodies and chromobodies, and the development of a reliable phenotypic readout for high-content imaging.

2 MATERIAL AND METHODS

2.1 Material

2.1.1 Chemicals and solutions

chemical / solution	manufacturer
10x RIPA Buffer	ChromoTek, Martinsried, Germany
10x T4 DNA-Ligase Reaction Buffer	New England Biolabs
2-Propanol	Carl Roth GmbH & Co. KG, Karlsruhe, Germany
2x YT Medium (2xYT)	Carl Roth GmbH & Co. KG, Karlsruhe, Germany
3,3',5,5'-Tetramethylbenzidin (TMB)	Carl Roth GmbH & Co. KG, Karlsruhe, Germany
5x Phusion HF- Buffer	New England Biolabs GmbH, Frankfurt, Germany
6x DNA Loading Dye	Thermo Scientific GmbH, Schwerte, Germany
Acetic Acid, 99-100%	Carl Roth GmbH & Co. KG, Karlsruhe, Germany
Acetone	Carl Roth GmbH & Co. KG, Karlsruhe, Germany
Acrylamide Bisacrylamide	Carl Roth GmbH & Co. KG, Karlsruhe, Germany
Agarose, molecular biology grade	Serva Electrophoresis GmbH, Heidelberg, Germany
Ammoniumperoxodisulfat (APS)	Carl Roth GmbH & Co KG, Karlsruhe
Ampicillin	AppliChem GmbH, Darmstadt, Germany
ATTO dye (NHS Ester)	ATTO-TEC GmbH, Siegen, Germany
Blasticidin	Carl Roth GmbH & Co. KG, Karlsruhe, Germany
β−Mercaptoethanol	Carl Roth GmbH & Co. KG, Karlsruhe, Germany
BSA	Sigma-Aldrich Chemie Gmbh, Munich, Germany
Color Silver Stain Kit	Thermo Scientific GmbH, Schwerte, Germany
Coomassie Brilliant Blue G250, R250	Serva Electrophoresis GmbH, Heidelberg, Germany
DAPI (4,6-diamiddino-2-phenylindole)	Roche Diagnostics GmbH, Mannheim, Germany
Di-sodium hydrogen phsophat	Merck KgaA, Darmstadt, Germany
DMEM, high glucose, with phenolred	Life Technologies GmbH, Darmstadt, Germany
DMEM/HAMs F12	Life Technologies GmbH, Darmstadt, Germany
DMSO ≥99 %	Sigma-Aldrich Chemie Gmbh, Munich, Germany
DNAse I	AppliChem GmbH, Darmstadt, Germany
dNTP Solution Mix	New England Biolabs GmbH, Frankfurt, Germany
EDTA	AppliChem GmbH, Darmstadt, Germany
Estradiol	Sigma-Aldrich Chemie Gmbh, Munich, Germany
Ethanol, absolut	Sigma-Aldrich Chemie GmbH, Munich, Germany
Ethanol, denatured	Carl Roth GmbH & Co. KG, Karlsruhe, Germany
Ethidiumbromid-Solution (0,025 %)	Carl Roth GmbH & Co. KG, Karlsruhe, Germany
Fetal Bovine Serum	Life Technologies GmbH, Darmstadt, Germany
Formaldehyde (37%)	Sigma-Aldrich Chemie GmbH, Munich, Germany
G418	Life Technologies GmbH, Darmstadt, Germany
GeneRuler 1 kb plus DNA Ladder	Thermo Scientific GmbH, Schwerte, Germany
Gentamycin (50 mg/ml)	PAA Laboratories GmbH, Pasching, Austria
Glucose D(+)	Carl Roth GmbH & Co. KG, Karlsruhe, Germany
Glycine	Carl Roth GmbH & Co. KG, Karlsruhe, Germany
Hoechst 33342 Solution	Life Technologies GmbH, Darmstadt, Germany
Hydrochloric acid 37%	AppliChem GmbH, Darmstadt, Germany
Hydrogen Peroxide	Fluka Chemie AG, Germany
Hygromycin	Carl Roth GmbH & Co. KG, Karlsruhe, Germany
Hyperphage (M13K07ΔpIII)	Progen Biotechnik GmbH, Heidelberg, Germany

Imidazol	Sigma-Aldrich Chemie GmbH, Munich, Germany
Insulin	Sigma-Aldrich Chemie Gmbh, Munich, Germany
Isopropyl-beta-D-thiogalaktopyranosid (IPTG)	Diagonal GmbH, Münster, Germany
Kanamycin	Carl Roth GmbH & Co. KG, Karlsruhe, Germany
L-glutamine	Sigma-Aldrich Chemie Gmbh, Munich, Germany
Lipofectamin 2000	Life Technologies GmbH, Darmstadt, Germany
Lipofectamin LTX	Life Technologies GmbH, Darmstadt, Germany
Luria Broth (LB) Medium	Carl Roth GmbH & Co. KG, Karlsruhe, Germany
Lysozyme	AppliChem GmbH, Darmstadt, Germany
Magnesium chloride	Sigma-Aldrich Chemie Gmbh, Munich, Germany
Methanol, min. 99 %	Carl Roth GmbH & Co. KG, Karlsruhe, Germany
Midiprep System PureYield Plasmid	Promega GmbH, Mannheim, Germny
Milkpowder, Blotting Grade	Carl Roth GmbH & Co. KG, Karlsruhe, Germany
NEB- Buffer 1-4	New England Biolabs GmbH, Frankfurt, Germany
NHS-activated SepharoseTM 4 Fast Flow	GE Healthcare, Uppsala, Sweden
NucleoSpin Gel and PCR Clean-up Kit	Macherey-Nagel, Düren Germany
NucleoSpin Plasmid Kit	Macherey-Nagel, Düren Germany
NP-40	Carl Roth GmbH & Co. KG, Karlsruhe, Germany
PageRuler™ Prestained Protein Ladder Plus	Fermentas GmbH, St.Leon-Rot, Germany
Penicillin Streptomycin	Life Technologies GmbH, Darmstadt, Germany
Phenylmethanesulfonylfluoride (PMSF)	SERVA Electrophoresis GmbH, Heidelberg, Germany
Phosphate Buffered Saline (PBS), 1x	Sigma-Aldrich Chemie GmbH, Munich, Germany
Phusion™ High-Fidelity DNA Polymerase	New England Biolabs GmbH, Frankfurt, Germany
Pierce protein free blocking buffer	Thermo Scientific GmbH, Schwerte, Germany
Polyacrylamide mix 30%	Carl Roth GmbH & Co. KG, Karlsruhe, Germany
Polyethyleneimine	Sigma-Aldrich Chemie GmbH, Munich, Germany
Ponceau S	Sigma-Aldrich Chemie Gmbh, Munich, Germany
Potassium chloride	Sigma-Aldrich Chemie Gmbh, Munich, Germany
Protease Inhibitor Mix M	SERVA Electrophoresis GmbH, Heidelberg, Germany
Resazurin (alamarBlue®)	AbD Serotec, Puchheim, Germany
Restrictionenzymes	New England Biolabs GmbH, Frankfurt, Germany
RNase A (10 mg/ml)	AppliChem GmbH, Darmstadt, Germany
Roti Phenol	Carl Roth GmbH & Co. KG, Karlsruhe, Germany
Roti Phenol/Chloroform/Isoamylalcohol	Carl Roth GmbH & Co. KG, Karlsruhe, Germany
Rubidium chloride	Carl Roth GmbH & Co. KG, Karlsruhe, Germany
Select Agar	Invitrogen GmbH, Karlsruhe, Germany
Sodium bicarbonate	Sigma-Aldrich Chemie Gmbh, Steinheim, Germany
Sodium carbonate	Sigma-Aldrich Chemie Gmbh, Steinheim, Germany
Sodium chloride	Carl Roth GmbH & Co. KG, Karlsruhe, Germany
Sodium dodecyl sulfate (SDS)	Carl Roth GmbH & Co. KG, Karlsruhe, Germany
Sulfuric acid, 96 %	Carl Roth GmbH & Co. KG, Karlsruhe, Germany
T4 Ligation Kit	New England Biolabs GmbH, Frankfurt, Germany
TEMED	Carl Roth GmbH & Co.KG, Karlsruhe, Germany
TGF-β1	Peprotec Inc., Hamburg, Germany
Tris (trisaminomethane)	Carl Roth GmbH & Co. KG, Karlsruhe, Germany
Triton X-100	Carl Roth GmbH & Co.KG, Karlsruhe, Germany
Trypsin/EDTA (1:250)	PAA Laboratories GmbH, Cölbe, Germany
Tween 20	Carl Roth GmbH & Co.KG, Karlsruhe, Germany
Withaferin A (WFA)	Merck Millipore, Darmstadt, Germany

2.1.2 Devices

device	manufacturer
ÄKTA FPLC system UPC 900	GE Healthcare, Uppsala, Sweden
Autoklave VX-95	Systec GmbH, Wettenberg, Germany
Cell Observer SD	Zeiss AG, Oberkochen, Germny
Centrifuge 5415R	Eppendorf AG, Hamburg, Germany
Centrifuge 5424	Eppendorf AG, Hamburg, Germany
Centrifuge 5810R	Eppendorf AG, Hamburg, Germany
Centrifuge Megafuge 1.0R	Heraeus Instruments, Hanau, Germany
Centrifuge Universal 2S	Hettich GmbH & Co KG, Tuttlingen, Germany
Confocal lasser scanning microscope LSM510	Zeiss AG, Oberkochen, Germny
CO_2-Incubator CB150	Binder GmbH, Tuttlingen, Germany
Elektrophoresis Chamber	Bio-Rad Laboratories GmbH, München, Germany
Envision 2102 Multilabel Reader	PerkinElmer, Rodgau, Germany
GFL water bath 1002	GFL, Burgwedel, Germany
GFL water bath 1083	GFL, Burgwedel, Germany
High-content microscope MetaXpressXL system	Molecular devices, Biberach, Germany
Incubator shaker C25	New Brunswick Scientific, Nürtingen, Germany
INTAS UV documentation system	INTAS, Goettingen, Germany
Light microscope TMS-F	Nikon, Duesseldorf, Germany
Magnet stirrer RCTbasic	IKA-Werke GmbH, Staufen, Germany
Microscope Axiovert 200M	Zeiss AG, Oberkochen, Germny
Microscope Olympus CKX 41	Olympus, Hamburg, Germny
Multipipet plus	Eppendorf AG, Hamburg, Germany
Mupid One electrophoresis unit	NIPPON Genetics EUROPE GmbH, Dueren, Germany
Neubauer chamber	Brand, Wertheim, Germany
Overhead rotator	Bachofer, Reutlingen, Germany
PCR device Primus 96 plus	MWG Biotech AG, Ebersberg, Germany
pH meter	Mettler-Toledo GmbH, Giessen, Germany
PHERAstar plate reader	BMG Labtech, Offenburg, Germany
Photometer	Eppendorf AG, Hamburg, Germany
Pipet HandyStep	Brand GmbH & Co KG, Wertheim, Germany
Pipets 10 µl, 20 µl, 100 µl, 200 µl, 1000 µl	Brand GmbH & Co KG, Wertheim, Germany
Pipettboy	Integra BioSciences, Fernwald, Germany
Pipette, 8-Kanal, 0,5 µl - 10 µl	Eppendorf AG, Hamburg, Germany
Plate-Incubator	Heraeus Instruments, Hanau, Germany
Power supply gel elektrophoresis MP-300V	Major Science, USA
PowerPac Basic Power Supply	Bio-Rad Laboratories GmbH, München, Germany
Scale AE160	Mettler-Toledo GmbH, Giessen, Germany
Scale BP 3100S	Sartorius AG, Göttingen, Germany
Scale CPA225D-0CE	Sartorius AG, Göttingen, germany
Scale XS205 DualRange	Mettler-Toledo GmbH, Giessen, Germany
Semi-Dry transfer cell	Bio-Rad Laboratories GmbH, München, Germany
Sonifier Sonopuls HD60/UW60	Bandelin, Berlin, Germany
Spectrometer NanoDrop 2000	Thermo Scientific, Schwerte, Germany
Steril hood	BDK GmbH, Sonnenbühl-Genkingen, Germany
Thermomixer comfort	Eppendorf AG, Hamburg, Germany

| Typhoon Trio Scanner | GE Healthcare, Uppsala, Sweden |
| Vortex Genie 2 | Scientific Industries, Karlsruhe, Germany |

2.1.3 Consumables

consumable	manufacturer
µClear 96-well microplate	Greiner Bio-One, Frickenhausen, Germany
µ-slide, 8-well, uncoated	Ibidi GmbH, Martinsried, Germany
96 well assay block	Thermo Scientific GmbH, Schwerte, Germany
Amersham Protan 0,45 µm Nitrocellulose	GE Healthcare, Uppsala, Sweden
Amicon® Ultra Centrifugal Filter Devices	Millipore S.A.S., Molsheim, France
Assay Block, 96-well, 2 ml	Schubert & Weiss, Munich, Germany
Blotting Paper Grad 703	Bio-Rad Laboratories GmbH, Munich, Germany
Cell Culture Flasks T-25, T-75, T-125	Corning GmbH, Wiesbaden, Germany
Cell Culture Plates, p100	Corning GmbH, Wiesbaden, Germany
Cryotubes, 1,8 ml	Greiner Bio-One, Frickenhausen, Germany
Desalting Column PD-10	GE Healthcare, Uppsala, Sweden
Falcon Tubes (15 and 50 ml)	Sarstedt AG & Co., Nümbrecht, Germany
Falcon-Tubes 15ml und 50ml	Greiner Bio-One, Frickenhausen, Germany
Filtorpur S 0.45	Sarstedt AG & Co., Nümbrecht, Germany
Filtropur S 0.2	Sarstedt AG & Co., Nümbrecht, Germany
GFP-multiTrap, GFP-Trap, RFP-Trap	ChromoTek GmbH, Martinsried, Germany
HisTrap™ FF column, 1 ml	GE Healthcare, Uppsala, Sweden
LoBind tubes	Eppendorf, Hamurg, Germany
Multiwell plate: 6, 12, 24, 48, 96 well, steril	Corning GmbH, Wiesbaden, Germany
NHS-activated Sepharose 4 Fast Flow	GE Healthcare, Uppsala, Sweden
Nitrocellulose Membrane	Bio-Rad Laboratories GmbH, Munich, Germany
PageRuler Plus Prestained Protein Ladder	Thermo Scientific, Schwerte, Germany
Parafilm	Brand GmbH & Co. KG, Wertheim, Germany
PCR-Reaction tube, 200 µl/500 µl	Sarstedt AG & Co., Nümbrecht, Germany
PD-10 desalting column	GE Healthcare, Uppsala, Sweden
Petridish, 145 x 20 mm	Greiner Bio-one, Frickenhausen, Germany
Petridish, 92 x 16 mm	Sarstedt AG & Co., Nümbrecht, Germany
pH Indicatorstrips, pH 0-14	Merck KGaA, Darmstadt, Germany
Pipettes (2, 5, 10 und 25 ml)	Sarstedt AG & Co., Nümbrecht, Germany
Pipettetips (10, 20, 200, 1000, 1250 µl)	Starlab GmbH, Hamburg, Germany
Protino® Ni-NTA Agarose	Macherey-Nagel, Düren, Germany
Reaction tube 1,5 ml / 2 ml (steril)	Sarstedt AG & Co., Nümbrecht, Germany
Superdex 75 10/300 GL	GE Healthcare, Uppsala, Sweden
syringe (2, 5, 10, 20, 50 ml)	B. Braun Melsungen AG, Melsungen, Germany
syringe filters (0.22 µM)	Carl Roth GmbH & Co. KG, Karlsruhe, Germany
Tips for repeating pipette	Eppendorf AG, Hamburg, Germany
Typhoon TRIO	GE Healthcare Life Sciences
UV cuvettes	Brand GmbH & co KG, Wertheim, Germany

2.1.4 Antibodies

Following primary and secondary antibodies were applied.

2.1.4.1 Primary antibodies

antibody (species)	manufacturer
anti-GFP 3H9 (rat, mAb)	ChromoTek, Munich, Germany
anti-RFP 3F5 (mouse, mAb)	ChromoTek, Munich, Germany
anti-GAPDH (rabbit, pAb)	Santa Cruz, Dallas, USA
anti-His$_6$ (mouse, mAb)	GE Healthcare, Uppsala, Sweden
anti-TagRFP (rabbit, mAb)	evrogen, Moscow, Russia
anti-vimentin clone V9 (mouse, mAb)	Sigma-Aldrich Chemie GmbH, Munich, Germany
anti-occludin (rabbit, pAb)	Life Technologies GmbH, Darmstadt, Germany
anti-SNAI1, SN9H2 (rat, mAb))	Cell Signaling, NEB, Frankfurt, Germany
anti-SNAI1, H130 (rabbit, pAb)	Santa Cruz, Dallas, USA
anti-SNAI1 (rabbit, pAb)	Abcam, Cambridge, UK
anti-M13 (mouse, mAb), HRP conjugate	GE Healthcare, Uppsala, Sweden

2.1.4.2 Secondary antibodies

antibody (species)	manufacturer
anti-mouse (goat) Alexa 488/546/647 conjugates	Life Technologies GmbH, Darmstadt, Germany
anti-rabbit (goat) Alexa 488/546/647 conjugates	Life Technologies GmbH, Darmstadt, Germany
anti-rat (goat) Alexa 488/546/647 conjugates	Life Technologies GmbH, Darmstadt, Germany

2.1.5 Oligonucleotides

Following oligonucleotides were applied for polymerase chain reactions. All oligonucleotides were synthesized by Metabion AG (Martinsried, Germany).

oligonucleotide	sequence
OCLN-His-fwd	5'-AAG GAT CCA GCC GCC ATG AAC TTT GAG ACA CCT TCA AAA AG-3'
OCLN-His-rev	5'-AAA AGC TTC TAG TGA TGG TGA TGG TGA TGT GTT TTC TGT CTA TCA TAG TCT CC-3'
OCLN-GST-fwd	5'-AAG GAT CCA ACT TTG AGA CAC CTT CAA AAA GAG-3'
OCLN-GST-rev	5'-AAG AAT CCC TAT GTT TTC TGT CTA TCA TAG TCT CCA-3'
SNAI1-His-fwd	5'-AAG GAT CCA GCC GCC ATG CCG CGC TCT TTC CTC G-3'
SNAI1-His-rev	5'-AAG AAT CTC AGC GGG GA CATCCT G-3'
SNAI1-GST-fwd	5'-AAG GAT CCC CGC GCT CTT TCC TCG-3'
SNAI1-GST-rev	5'-AAG GAT CCC CGC GCT CTT TCC TCG-3'
VIM-His-fwd	5'-AAG GAT CCA GCC GCC ATG TCC ACC AGG TCC GTG TC-3'
VIM-His-rev	5'-AAA AGC TTT TAG TGA TGG TGA TGG TGA TGT TCA AGG TCA TCG TGA TGC-3'
VIM-GFP-fwd	5'-AAG GGT ACC TCC ACC AGG TCC GTG TCC-3'
VIM-rod-fwd	5'-AAA GGT ACC AAG AAC ACC CGC ACC AAC GAG-3'
VIM-tail-fwd	5'-AAA GGTA CCA GCA GGA TTT CTC TGC CTC TTC C-3'
VIM-head-rev	5'-AAA GGA TCC TCA GAA CTC GGT GTT GAT GGC-3'
VIM-rod-rev	5'-AAG GGA TCC TCA CTC CTC GCC TTC AG CAG-3'
VIM-rev	5'-AAG GGA TCC TCA TTC AAG GTC ATC GTG ATG C-3'
VIM-mCherry-fwd	5' AAA AGC TTA GGT GGA GGA GGT TCT TCC ACC AGG TCC GTG TC-3'
SNAI1-GFP-fwd	5'-AAA AGC TTT AGG TGG AGG AGG TTC TCC GCG CTC TTT CCT CG-3'
SNAI1-cherry-fwd	5'-AAA AGC TTA GGT GGA GGA GGT TCT CCG CGC TCT TTC CTC G-3'
SNAI1-rev	5'-AAG GTA CCT CAG CGG GGA CAT CCT GAG CAG CCG G-3'

OCLN-GFP-fwd	5'-AAA AGC TTT AGG TGG AGG AGG TTC TTC ATC CAG GCC TCT TG-3'
OCLN-cherry-fwd	5'-AAA AGC TTA GGT GGA GGA GGT TCT TCA TCC AGG CCT CTT G-3'
OCLN-rev	5'-AAG GTA CCC TAT GTT TTC TGT CTA TCA TAG TCT CC-3'
$attB$-V$_H$H-fwd	5'-GGG GAC AAG TTT GTA CAA AAA AGC AGG CTG GCC ATG GCT CAG GTG CAG CTG GTG-3'
$attB$-GFP-rev	5'-GGG GAC CAC TTT GTA CAA GAA AGC TGG GTT TAC TTG TAC AGC TCG TCC ATG CCG-3'
V$_H$H-I-fwd	5'-GGG GAG ATC TCC GGC CAT GGC TCA GGT GCA GCT GGT GGA GTC TGG-3'
V$_H$H-II-fwd	5'-GGG GAG TTC TCC GGC CAT GGC TCA GGT GCA GCT GCA GGA GTC TGG-3'
V$_H$H-III-fwd	5'-GGG GAG ATC TCC GGC CAT GGC TCA TGT GCA GCT GCA GGA GTC TGG-3'
V$_H$H-I-rev	5'-GGG GGA AGC TTC TTG AGG AGA CGG TGA CCT GCA T-3'
V$_H$H-II-rev	5'-GGG GGA AGC TTC TTG AGG AGA CGG TGA CCT GGG-3'
V$_H$H-III-rev	5'-GGG GGA AGC TTC TGC TGG AGA CGG TGA CCT GGG T-3'
Biv-I-fwd	5'-GGC CCA GCC GGC CAT GGC TC-3'
Biv-I-rev	5'-CTC CAC CTG AGG AGA CGG TGA CCT GGG-3'
Biv-II-fwd	5'-CGG TGG ATC GGT GGC GGA GGT AGC GCT CAG GTG CAG CTG GTG GGA G-3'
Biv-II-rev	5'-CAG TGA ATT CTA TTA GTG ATG GTG ATG GTG-3'

2.1.6 Vectors

Following vector backbones were used for molecular cloning of DNA constructs.

vector	manufacturer
pRSETB	Addgene, Cambridge, USA
pGEX-6P-1	Addgene, Cambridge, USA
pEGFP-N1	Clontech, Mountain View, USA
pEGFP-C1	Clontech, Mountain View, USA
pHEN4	(Arbabi Ghahroudi et al., 1997)
pHEN6	(Conrath et al., 2001)
pLenti-V5-DEST	Life Technologies GmbH, Darmstadt, Germany
pENTR	Life Technologies GmbH, Darmstadt, Germany
pDONR	Life Technologies GmbH, Darmstadt, Germany
pHEN6-Biv	provided by ChromoTek-GmbH, Martinsried, Germany
pmCherry-C1	provided by ChromoTek-GmbH, Martinsried, Germany

2.1.7 DNA constructs

Following DNA constructs were generated by molecular cloning, using the indicated oligonucleotides, vector backbones and restriction sites.

plasmid	vector backbone	oligonucleotides	restriction sites
VIM-His$_6$	pRSET-B	VIM-His-fwd/VIM-His-rev	BamHI/HindIII
SNAI1-His$_6$	pRSET-B	SNAI1-His-fwd/ SNAI1-His-rev	BamHI/HindIII
OCLN-His$_6$	pRSET-B	OCLN-His-fwd/ OCLN-His-rev	BamHI/HindIII
GST-SNAI1	pGEX-6P-1	SNAI1-GST-fwd/ SNAI1-GST-rev	BamHI/EcoRI
GST-OCLN	pGEX-6P-1	OCLN-GST-fwd/ OCLN-GST-rev	BamHI/EcoRI

all nanobodies	pHEN6	direct restriction from pHEN4	SfiI/BstEII or NcoI/BstEII
all chromobodies	pEGFP-N1	V_HH-I-III fwd/V_HH-I-III-rev-	BglII/HindIII
VB6-VB6	pHEN6-Biv	Step 1: Biv-I-fwd/Biv-I-rev Step2: Biv-II-fwd/Biv-II-rev	Step 1: NcoI/Bsu36 Step 2: BamHI/EcoRI
GFP-OCLN	pEGFP-C1	OCLN-GFP-fwd/OCLN-rev	HindIII/KpnI
GFP-SNAI1	pEGFP-C1	SNAI1-GFP-fwd/SNAI1-GFP-rev	HindIII/KpnI
GFP-VIM	pEGFP-C1	VIM-GFP-fwd/VIM-rev	KpnI/BamHI
GFP-head	pEGFP-C1	VIM-GFP-fwd/VIM-head-rev	KpnI/BamHI
GFP-rod	pEGFP-C1	VIM-rod-fwd/VIM-rod-rev	KpnI/BamHI
GFP-tail	pEGFP-C1	VIM-tail-fwd/VIM-rev	KpnI/BamHI
mCherry-OCLN	pmCherry-C1	OCLN-mCherry-fwd/OCLN-rev	HindIII/KpnI
mCherry-SNAI1	pmCherry-C1	SNAI1-mCherry-fwd/SNAI1-GFP-rev	HindIII/KpnI
mCherry-VIM	pmCherry-C1	VIM-mCherry-fwd/VIM-rev	HindIII/KpnI
pENTR-VB6	pENTR	attB-V_HH-fwd/attB-GFP-rev	Gateway cloning
pLenti-VB6	pLenti-V5-DEST	-	Gateway cloning
pENTR-Actin-CB	pENTR	attB-V_HH-fwd/attB-GFP-rev	Gateway cloning
pLenti-Actin-CB	pLenti-V5-DEST	-	Gateway cloning

All resulting constructs were sequenced and expression was tested in *E.coli* XL1 Blue or *E.coli* BL21 for bacterial expression constructs or in HEK293T for mammalian expression constructs and analyzed by Western blot analysis.

2.2 Methods

2.2.1 Molecular biological methods

2.2.1.1 Polymerase chain reaction

In order to amplify DNA fragments and to introduce selective restriction sites, polymerase chain reaction (PCR) was performed. The reaction typically contained the template DNA, two specific oligonucleotides (see section 2.1.5), deoxynucleotide triphosphates (dNTPs) mix, reaction buffer and the thermostable DNA Phusion polymerase (Table 2.1). PCR amplification was carried out according to similar programs as shown in Table 2.2 and repeated in ~30 cycles.

Table 2.1: Typical PCR reaction

	volume	final conc.
5x HF buffer	10 µl	1x
dNTP mix (10 mM)	1 µl	200 µM/dNTP
forward primer	1 µl	200 nM
reverse primer	1 µl	200 nM
Phusion polymerase	1 µl	0.08 U/µl
template DNA	50 ng	1 ng/µl
ddH$_2$O	ad 50 µl	

Table 2.2: Typical PCR program

	temp.	time	cycles
initial denaturation	94 °C	30s	1
denaturation	94 °C	15 s	
annealing	58 °Cs	15 s	30
extension	72 °C	20 s	
final extension	72 °C	8 min	1
end	4 °C	∞	

2.2.1.2 Restriction analysis

Digestion of DNA fragments and plasmids was performed using restriction endonucleases from New England Biolabs following the manufacturer's guidelines. For analytical digestion 500 ng – 1 µg DNA were used and 2.5 – 5 µg for preparative digestion.

2.2.1.3 Agarose gel electrophoresis

DNA samples including PCR fragments and DNA digestions were separated and analyzed by agarose gel electrophoresis. To this end, 5x DNA loading dye was added to the samples, which were separated using a 1 % agarose gel in 1x Tris-Acetate-EDTA (TEA)-buffer, containing 0.025 µg/ml ethidium bromide (EtBr). For precise sizing of DNA fragments, GeneRuler 1kb plus DNA ladder (Thermo scientific) was used. Detection of EtBr-stained DNA fragments was performed with an Intas UV system (Intas Science Imaging). For molecular cloning, DNA fragments were cut from the gel and purified by means of the NucleoSpin Gel and PCR clean-up Kit (Macherey-Nagel) following the manufacturer's guidelines. For elution H$_2$O was used instead of the recommended elution buffer.

2.2.1.4 DNA Ligation

During molecular cloning, ligation of digested and purified DNA fragments was performed using the T4 DNA ligase system (New England Biolabs). Thereby a molar 1:3 ratio of

purified vector and insert was deployed (Table 2.3). Ligations were incubated at 16 °C overnight and subsequently transformed into *E. coli* XL1 blue cells.

Table 2.3: Typical ligation reaction.

	amount / volume
10x T4 Ligase buffer	1 µl
T4 Ligase	1 µl
vector	~150 ng
insert	~50 ng
ddH$_2$O	ad 10 µl

2.2.1.5 Transformation of bacteria

For transformation of bacteria, 250 µl of chemical competent *E. coli* XL1 blue cells or *E. coli* BL21 were thawed on ice. Subsequently, ~50-100 ng plasmid DNA or 5 µl ligation samples were added and incubated for 30 min on ice. Heat shock was performed for 45 s at 42 °C followed by additional incubation on ice for 2 min. After culturing for 1 h at 37 °C in 250 ml SOC medium, cells were plated on selection agar and incubated overnight at 37 °C.

2.2.1.6 Preparation of plasmids

Transformed *E. coli* XL1 blue cells were cultured overnight at 37 °C in 5 ml LB-medium for plasmid preparation of small DNA amounts and in 50 ml LB medium for high DNA amounts in presence of appropriate antibiotics. Preparation of small DNA amounts was performed with the NucleoSpin® Plasmid Kit (Macherey-Nagel), while high DNA amounts were isolated with the Midiprep System PureYield Plasmid Kit (Promega) following the respective manufacturer's protocol. DNA concentration was determined by measuring the absorbance at 260 nm using a NanoDrop2000 spectrometer (Thermo Scientific).

2.2.1.7 Gateway cloning

Construction of the plasmids pLenti-VB6-CB and pLenti-Actin-CB was performed using the Gateway technology system (Life Technologies) according to the manufacturer's protocol. Briefly, chromobody sequences were amplified using the *attB*-V$_H$H-fwd and *attB*-GFP-rev primers and shuttled into the pDONR vector by a BP recombination reaction (Table 2.4) at room temperature overnight. The reaction was stopped by adding 2 µl proteinase K solution (2 µg/µl) at 37 °C for 10 min. After transformation into *E. coli* XL1 blue and isolation by plasmid preparation the resulting entry clone was added to a LR recombination reaction (Table 2.5) at room temperature overnight, to shuttle the chromobody construct into the pLente-V5/DEST vector. LR reaction was stopped by 2 µl proteinase K solution (2 µg/µl) at 37 °C for 10 min.

MATERIAL AND METHODS

Table 2.4: BP recombination reaction

component	volume
attB PCR product	2 µl
pDONR (150 ng/µl)	2 µl
5 x BP Clonase buffer	4 µl
BP Clonase	4 µl
TE buffer, pH 8	ad 16 µl

Table 2.5: LR recombination reaction

component	volume
entry clone	2 µl
pLenti-V5/DEST (150 ng/µl)	2 µl
5 x LR Clonase buffer	4 µl
LR Clonase	4 µl
TE buffer, pH 8	ad 16 µl

2.2.2 Biochemical methods

2.2.2.1 Preparation of phage particles

A phage library representing the whole V_HH repertoires of an alpaca, immunized with OCLN-His_6, SNAI1-His_6 and VIM-His_6 was used for the preparation of phage particles. Alpaca immunization, cloning of the V_HH library into the pHEN4 vector and transformation of TG1 cells was performed by ChromoTek GmbH (Martinsried, Germany), who kindly provided the completed TG1 phage library. To produce phage particles, TG1 cells containing the phagemids were cultured at 37 °C in 2xYT, containing 100 µg/ml ampicillin and 2 % (w/v) glucose (2xYT-amp/glu), until reaching a logarithmic growth phase, when the M13K07 helper phage (Progen) was added for infection. After additional 30 min, cells were harvested by centrifugation, followed by resuspension of the cell pellet in 2xYT medium containing 100 µg/ml ampicillin and 25 µg/ml kanamycin (2xYT-amp/kana) and incubated at 37 °C overnight. Subsequently, the produced phage particles expressing V_HH domains on their surface were harvested from the supernatant by precipitation with 20 % polyethylene glycol (PEG) 6000 for 1 h on ice, followed by centrifugation (30 m in, 4000 rpm, 4°C). Finally, the phage pellet was resuspended in 1 x PBS and stored at 4 °C for further until further use.

2.2.2.2 Solid phase panning

To enrich phage particles expressing V_HH domains specific for occludin, SNAI1 and vimentin, two consecutive rounds of solid phase panning were performed. Initially, phage particles were pre-cleared by incubation with immunotubes, previously blocked with 5 % (w/v) nonfat dry milk in 1xPBS (5 % MBPS), to remove unspecifically binding phages. Pre-cleared phages were then added to immunotubes coated with 20 µg of purified GST-occludin, GST-SNAI1 and VIM-His_6. After 2 h incubation at room temperature, weakly binding phages were removed by washing 10 times with TBST (0.05 % Tween 20 in 1 x PBS), while the last washing step was performed with 1 x PBS. Bound phages were eluted with 100 mM triethylamine (pH 10) and eluted phages were immediately neutralized with 1 M Tris/HCL (pH 7.4). These phages were used to re-infect *E. coli* TG1 cells for a second panning round. Thereafter, re-infected TG1 cells were plated on agar plates (2xYT-amp/glu) and enrichment

of phages carrying antigen specific V_HHs was determined by comparative analysis of colonies, containing phagemides, derived from uncoated control tubes or from tubes, coated with the respective antigen.

2.2.2.3 Phage-ELISA

Phage ELISA was performed to analyze the binding specificities of monoclonal phage clones resulting from solid phase panning. Phage particles derived from single TG1 colonies were prepared in 2 ml cultures in 96-well format. Purified antigens (GST-OCLN, GST-SNAI1 and VIM-His$_6$) were coated on microtiter plates (10 µg/well) and blocked with 5% MPBS. Monoclonal phage particles were added and incubated for 2 h at room temperature. Subsequently, plates were washed 3 times with TBST (0.05 % Tween in tris buffered saline) and additional 3 times with 1 x PBS. Detection of specifically bound phages was performed using a HRP-conjugated anti-M13 monoclonal antibody (GE-Healthcare).

2.2.2.4 Protein expression in E.coli

Expression of OCLN-His$_6$, SNAI1-His$_6$, VIM-His$_6$, GST-occludin and GST-SNAI1 was carried out in *E.coli* BL21 cells, while XL1 blue cells were used for the expression of nanobodies. Generally, 2 l cultures were grown at 37 °C in LB medium containing appropriate antibiotics and protein expression was induced at OD_{600} 0.6-0.8 by adding 0.5 mM isopropyl β-D-1-thiogalactopyranoside (IPTG) overnight at 30 °C. IPTG is a structural analog of lactose that permanently binds to the *lacI* repressor and allows constant protein expression of genes controlled by the *lac*-promoter. The next day, cells were harvested by centrifugation (5000 x g, 10 min, 4 °C) and pellets were resuspended in binding buffer (1x PBS, 0.5 M NaCl, 20 mM imidazol, pH 8 for His$_6$ tagged proteins and 1 x PBS for GST-tagged proteins). If required, resuspended pellets were stored at - 20 °C until further use.

Standard lysis of bacteria was performed in binding buffer containing additional DNaseI (1 µg/ml), phenylmethanesulfonylfluoride (PMSF 0.5 mM), 1 x protein inhibitor mix B (Serva) and lysozyme (0.1 mg/ml). After 1 h incubation at 4 °C on an end-over end rotor, cell suspensions were sonicated 10 x 20 pulses. Cells expressing VIM-His$_6$ were lysed under denaturing conditions (40 mM NaHCO$_3$, 1 % SDS, 300 mM NaCl, 20 mM β-mercaptoethanol, pH 9.6) for 1 h at 37 °C followed by sonication (10 x 20 pulses). Finally, insoluble components were separated by centrifugation (20 000 x g, 20 min, 4 °C) and supernatants were filtered through a 0.45 µm filter. Supernatants derived from VIM-His$_6$ expressing cells were diluted 1:4 previous to protein purification.

2.2.2.5 Protein purification

Purification of His$_6$-tagged proteins

His$_6$-tagged proteins were purified by immobilized metal ion affinity chromatography (IMAC) using a Ni^{2+}- nitrilotriacetic acid (NTA) matrix and an ÄKTA purifier FPLC-system (GE Healthcare). 1 ml HisTrap FF (GE Healthcare) columns were equilibrated in binding buffer (5 column volumes, CV) and the flow rate during the entire purification process was set to 1 ml/min. For purification of vimentin-His$_6$ an alternative binding puffer (2 x PBS), 0.125 % SDS, 5 mM β-mercaptoethanol, 5 mM imidazole, pH 8.0) was used. Elution was performed by applying an imidazole gradient (Elution buffer: 1x PBS, 0.5 M NaCl, 500 mM imidazol, pH 6.8) and eluted proteins were collected in 500 µl fractions.

Purification of GST-tagged proteins

GST-tagged proteins were purified by means of an ÄKTA purifier FPLC-system (GE Healthcare), using columns with glutathione-agarose matrix. 1 ml GSTrap FF (GE Healthcare) columns were equilibrated in 1 x PBS (5 column volumes, CV) and the flow rate during the entire purification process was set to 1 ml/min. Elution was performed by applying a two-step gradient with elution buffer (50 mM Tris-HCl pH 8.0, 10 mM reduced gluthatione) and eluted proteins were collected in 500 µl fractions.

2.2.2.6 Gel filtration and protein desalting

Gel filtration chromatography was performed using an ÄKTA purifier FPLC-system and a Superdex 75 gelfiltration column (GE Healthcare). The column was equilibrated in 1 x PBS (2 CV) and the flow rate during the entire purification process was set to 0.5 ml/min. 2 ml of the peak fractions resulting from affinity chromatography were applied to the column and proteins were collected in 500 µl fractions. Desalting of VIM-His$_6$-containing fractions into PBS was carried out with PD-10 Desalting Columns (GE Healthcare) according to the manufacturer's protocol.

2.2.2.7 Immobilzation of nanobodies on sepharose beads

2 mg of purified nanobodies (2 mg/ml) in 1 x PBS were coupled to 1 ml NHS-activated sepharose according to the manufacturer's protocol.

2.2.2.8 Labeling of nanobodies with organic dyes

Coupling of nanobodies to the NHS-activated organic dye ATTO488 (ATTOTEC) was performed according to the manufacturer's protocol. Subsequently, unbound dye was removed by separation with PD-10 Desalting Columns (GE Healthcare) according to the

manufaturer's protocol. Degree of labeling (DOL) was determined by absorption spectroscopy according the instructions provided by ATTOTEC (www. ATTOTEC.com).

2.2.2.9 Mammalian cell lysis

Mammalian cells were washed 3 times with 1 x PBS and harvested from 10 cm cell culture dishes by centrifugation (200 g, 5 min, 4 °C). Snap-frozen cell pellets were stored at -20 °C until further use. For analysis of occludin or vimentin, cell lysis was performed in 200 µl RIPA buffer (10 mM Tris/Cl pH 7.5, 150 mM NaCl, 0.1 % SDS, 1 % Triton X-100, 1 % Deoxycholate, 5 mM EDTA, 1 µg/ml DNaseI, 2.5 mM $MgCl_2$, 2 mM PMSF, 1x protease inhibitor mix M (Serva)), while for analysis of SNAI1 standard lysis buffer (10 mM Tris/Cl pH 7.5; 150 mM NaCl; 0.5 mM EDTA; 0.5% NP-40) was used. Pellets were homogenized by repeated pipetting for 40 min (20 x, every 10 min) on ice and incubated for additional 10 min in a sonication ice bath, if RIPA buffer was used. After centrifugation (10 min at 18,000 x g) protein concentrations of supernatants were determined by BCA Protein Assay (Thermo Scientific) according to the manufacturer's protocol.

2.2.2.10 SDS-PAGE and Western blot

Denaturing polyacrylamid gel electrophoresis (SDS-PAGE) was performed to allow size-dependent separation of proteins. Samples, containing 1 x sample buffer (0.1 % 2-Mercaptoethanol, 0.0005 % Bromophenol blue, 10 % Glycerol, 2 % SDS in ddH_2O) were denaturated at 95 °C for 5 min. Separation using a BioRad electrophoresis system was applied at 150 – 200 V in running buffer (25 mM Tris/HCl, 1,92 M glycine in ddH_2O) . Gels were prepared according to Table 2.6 and 2.7.

Table 2.6: Separation gel components

component	final conc.
Acrylamide	8-15 % (w/v)
Bisacrylamide	0.08-0.3 % (w/v)
Tris/HCl pH 8.8	375 mM
SDS	0.1 %
APS	0.05 % (w/v)
TEMED	0.1 % (v/v)

Table 2.7: Stacking gel components

component	final conc.
Acrylamide	5 % (w/v)
Bisacrylamide	0.33 % (w/v)
Tris/HCl pH 6.8	60 mM
SDS	0.1%
APS	0.05% (w/v)
TEMED	0.1% (v/v)

Separated proteins were either stained with Coomassie Brilliant Blue or transferred from the SDS-gel to a nitrocellulose membrane by Western blotting.

For Coomassie staining, Coomassie solution (0.3 % Coomassie Blue R 250, 50 % methanol, 10 % acetic acid in ddH_2O) was added for 30 min followed by removal of excessive dye with

destaining solution 1 (50 % ethanol, 10 % acetic acid in H$_2$O) for 1 h and destaining solution 2 (10 % ethanol, 5 % acetic acid) overnight.

During Western blotting proteins were transferred from SDS-gels to nitrocellulose membranes by semi-dry blotting system (BioRad) at 150 mM per gel for 1.5 - 2 h. Subsequently, total protein on membranes was stained reversibly with Ponceau S solution (0.5 % Ponceau S, 10 % acetic acid in ddH$_2$O). For specific protein detection membranes were incubated overnight at 4 °C with primary antibodies (see section 2.1.4.1), diluted in MTBST (5 % nonfat dry milk in TBST (0.05 % Tween in tris buffered saline)) or in 5 % bovine serum albumin (BSA) in TBST according to the manufacturer's guidelines. The next day, membranes were washed 3 times with TBST for 5 min followed by incubation with a fluorescently labeled secondary antibody (see section 2.1.4.2) diluted in MTBST for 1 h at room temperature. After additional washing steps (3 x TBST), membranes were dried and fluorescent signals were detected on a Typhoon-Trio laser scanner (GE Healthcare).

2.2.2.11 Immunoprecipitation

Supernatants derived from mammalian cells (see section 2.2.2.9) were adjusted with dilution buffer (10 mM Tris/Cl pH7.5, 150 mM NaCl, 0.5 mM EDTA, 2 mM PMSF) to 0.5 ml. 10 µl (2 %) were removed for later analysis of the input fraction. Precipitation was performed at 4 °C for 16 h on an end-over-end rotor using 30 µl of nanobodies immobilized on sepharose beads. As negative control a non-related nanobody (specific for bovine serum albumin) was used. After centrifugation (2 min, 2500 x g, 4°C) the supernatant was removed. 10 µl (2 %) of the supernatant was used for later analysis of the non-bound (flow through) fraction. The bead pellet was washed two times in 0.5 ml dilution buffer, resuspended in 2x sample buffer and boiled for 10 min at 95°C. Finally, 1 % of the input, 1 % of the non-bound and 10 % of the bound fractions were analyzed by SDS-PAGE followed by Western blot analysis as described in section 2.2.2.10.

2.2.2.12 Intracellular-immunoprecipitation

1 x 10^6 – 1 x 10^7 HEK293T cells were transiently transfected with equal amounts of expression vectors encoding for VB3-CB, VB6-CB (vimentin-chromobodies) or eGFP. Transfection efficiency was monitored the next day by fluorescence microscopy and cells were harvested 24 h after transfection. Cell pellets were lysed (see section 2.2.2.9) and chromobodies or eGFP were precipitated using the GFP-Trap (ChromoTek) as described in 2.2.2.11.

2.2.3 Cell culture methods

2.2.3.1 Culturing of mammalian cell lines

All cell culture techniques were carried out under sterile conditions on a laminar flow hood. Cryopreserved cells (10 % DMSO in culture medium) were thawed in a 37°C water bath. Cell were separated from thawing medium by centrifugation (100 x g, 5 min), transferred into fresh culture medium and grown at 37 °C, 5 % CO_2 and 95 % humidity in T75 or T125 culture flasks. HEK293T, HEK293-FT, HeLa, Huh7, BHK (clone 2) and MDCK were cultured in DMEM (high glucose, pyruvate) supplemented with 10 % fetal bovine serum (FBS), 200 mM glutamine and antibiotics. HEK293-FT culture medium additionally contained 500 µg/ml G418 (Sigma Aldrich). A549 cells were cultured in DMEM/F-12 (high glucose, pyruvate) supplemented with 10 % FBS, 200 mM glutamine and antibiotics. MCF7 cells were cultured in DMEM (high glucose, pyruvate) supplemented with 2 mM glutamine, 10% fetal bovine serum, antibiotics, 1 µM estradiol and 1 U/ml insulin. A549_VB6-CB cells were maintained in A549 medium supplemented with 80 µg/ml hygromycin (PAA), while A549_Actin-CB medium contained 4 µg/ml blasticidin (Carl Roth GmbH). Huh7_Actin-CB were cultured in Huh7 medium supplemented with 5 µg/ml blasticidin. Subconfluently grown cells were passaged every 2-3 days using trypsin/EDTA. Primary hepatocytes, provided by the group of Prof. Andreas Nüssler were cultured as described previously (Schyschka et al., 2013).

2.2.3.2 Cell seeding and compound treatment

Prior to cell seeding, cells were trypsinized and counted using a Neubauer chamber. For biochemical techniques cells were seeded in 10 cm culture dishes and grown to 95 % confluence. For microscopical use, between $2x10^3$ and $8x10^3$ cells were seeded in µClear 96-well plates (Greiner) and grown for 24 to 72 h. For time-lapse imaging and high-content imaging, cells were seeded in antibleaching DMEM-gfp medium (evrogen). For FRAP analyses, $1.5x10^4$ cells were seeded in µ-slide 8-well chamber (Ibidi) and grown overnight.

Compound treatment with 5 ng/ml TGF-β1 (Peprotech) or 50 - 500 nM Withaferin A (WFA, Merck Millipore) was performed up to 72 h.

2.2.3.3 Transfection

Transient transfection was carried out either with Lipofectamine LTX (Life Technologies) or polyethyleneimine (PEI, Sigma Aldrich). HeLa, BHK and Hek293T cells were transfected with PEI working solution (0.4 mg/ml PEI, 300 mM NaCl in ddH_2O, pH 7 for Hek293T, pH 10 for HeLa, BHK). DNA-PEI complexes were prepared, using max. 200 ng DNA and 1.5 µl

MATERIAL AND METHODS

PEI in 20 µl DMEM for 96-well format or 24 µg DNA and 180 µl PEI in 600 µl DMEM for 10 cm culture dishes, and incubated for 15 min at room temperature. Subsequently, complexes were added to the cells and incubated for 24 h at 37 °C, 5 % CO_2 and 95 % humidity.

Transfection of A549 cells was carried out with Lipofectamine LTX according to the manufacturer's protocol. Briefly, for 96-well format 100 ng DNA, 0.4 µl Lipofectamine LTX and 0.1 µl PLUS reagent were diluted in 20 µl OptiMEM (Life Technologies), incubated for 30 min at room temperature and added to the cells for 24 h.

2.2.3.4 Lentiviral transduction

Lentiviral transduction was performed to allow stable integration of genes in the genome of desired cell lines. Lentiviral particles were prepared, using the ViraPower lentiviral expression systems (Life Technologies), according to the manufacturer's protocol. Briefly, HEK293-FT cells cultured in T125 flasks were transfected with the ViraPower packaging mix and desired pLenti/V5-DEST plasmids. Supernatants, containing virus particles were collected 48 h and 72 h after transfection and residual cell fragments were removed by centrifugation (3000 x g, 15 min, 4 °C), followed by filtering through 0.45 µm pore size filters. Subsequently, virus particles were concentrated by ultracentrifugation (50 000 x g, 90 min, 4 °C), resuspended in 100 µl of 1 % BSA in 1 x PBS and stored at – 80 °C until further use.

Cells were transduced, by adding 20 µl concentrated phage particles (5 x 10^7 transducing units / ml) per well (12 well plate) and incubated for 24 h at 37 °C, 5 % CO2 and 95 % humidity. Medium was replaced by fresh culture medium 24 h after transduction.

2.2.3.5 Generation of stable cell lines

For the generation of stable cell lines, cells were transduced with lentiviral particles containing pLenti/V5-DEST plasmids coding for chromobodies. After transduction, cells were subjected to a two-week selection period with appropriate antibiotics (hygromycin or blasticidin). Single-cell separation in 96-well plates (1 cell / well), as well as cell sorting of polyclonal cell lines with equal expression levels was performed by fluorescence active cell sorting (FACS) (conducted by FACS core facility, University of Tuebingen, Hill campus). For the selection of monoclonal cell lines and single clones were analyzed microscopically, regarding the level of chromobody expression.

2.2.3.6 Resazurin assay

A549 cells were transiently transfected with plasmids coding for VB3-CB, VB6-CB or GFP. 72 h post transfection, cells were incubated with culture medium containing resazurin (Sigma Aldrich, 10 µg/ml final concentration) for 1 h. Fluorescence was measured at 570 nm and 600 nm with a PHERAstar plate reader (BMG Labtech). Student's t-test was performed for statistical analysis.

2.2.3.7 Wound healing and transwell invasion assay

For wound healing assays, A549-wt or A549_VB6-CB cells were seeded in 12-well plates and grown to 90 % confluence. Three scratch wounds per well were applied with a 200 µl pipette tip and non-adherent cells were washed twice with PBS. Fresh medium with or without 5 ng/ml TGF-β was added and cells were cultured for 48 h. Phase-contrast images were taken immediately (0 h), 24 h and 48 h after wounding with a Cell Observer SD (Zeiss), 10 x magnification. Open wound areas were determined with the *TScratch automated analysis* software (Geback et al., 2009). For statistical analysis student's t-test was used.

For invasion assays, polycarbonate membrane transwell inserts (8 µM pre size, 0.33 cm^2, Corning) for 24-well plates were coated with 0.4 mg/ml growth factor reduced Matrigel (BD Biosciences) according to the manufacturer's guidelines. A549-wt or A549_VB6-CB cells were seeded at $5x10^4$ cells per well on Matrigel-coated inserts in FBS free medium in presence or absence of TGF-β and 10 % FBS was added to the bottom wells of the chambers. After 24 h and 48 h cells were washed with PBS, fixed with 100 % Methanol for 15 min and stained with crystal violet (1 % crystal violet, 10 % ethanol in H$_2$O) for 30 min. Non-invading cells were swiped off and phase-contrast images were taken with Cell Observer SD (Zeiss), 10 x magnification. The percentage of invading cells was determined with ImageJ software.

2.2.3.8 Immunocytochemistry

For immunocytochemistry cells cultured in µClear 96-well plates were washed twice with 1 x PBS and fixed with 4 % paraformaldehye (PFA) in 1 x PBS for 15 min at room temperature. Subsequently, cells were washed twice with 1 x PBS and blocked and permeabilized with 3 % BSA, 0.1 % Triton X-100 in PBS for 30 min. Incubation with primary antibodies or ATTO488 labeled nanobodies, diluted in 3 % BSA in PBS was carried out at 4 °C overnight. After additional washing steps (3 x with 0.02 % Tween in PBS, PBST), secondary antibodies diluted in 3 % BSA in PBS were incubated for 1 h at room temperature. Finally, cells were counterstained with 0.02 µg/ml 4,6-diamidino-2-phenylindole (DAPI, Sigma Aldrich) for 1 min and washed 3 times with PBST. Multiwell plates were stored in PBS at 4 °C.

2.2.3.9 Fluorescent-2-hybrid (F2H) assay

Based on a *lac* operator system, the fluorescent-2-hybrid assay was carried out to analyze intracellular protein interactions as described by Zolghadr et al. (Zolghadr et al., 2008). 7×10^3 BHK (clone2) cells were seeded in µClear 96-well plates and transfected with plasmids coding for one bait and one prey protein, labeled with two different fluorescent proteins. 24 h-interactions were analyzed microscopically.

2.2.3.10 Classic microscopy

For initial selection of the chromobodies and for co-localization studies, images were acquired with an Axiovert 200M (Carl Zeiss Microscopy GmbH) and 40 x magnification in combination with AxioVision 4.7.1.0 imaging software (Carl Zeiss Microscopy GmbH).

Morphological studies of A549 wildtype (A549-wt) and A549-VB6-CB were performed with a Cell Observer SD (Carl Zeiss Microscopy GmbH), 10 x magnification in combination with the Zen2 blue edition software (Carl Zeiss Microscopy GmbH).

Images for F2H analyses were acquired with an ImageXpress micro XL system (Molecular Devices), 20 x magnification in combination with MetaXpress software (64 bit, 5.1.0.41, Molecular Devices).

2.2.3.11 Fluorescence recovery after photobleaching (FRAP)

For fluorescence recovery after photobleaching (FRAP) experiments, HeLa cells cultured in µ-slide 8-well chambers were transiently transfected with the plasmids coding for eGFP-vimentin (GFP-VIM), VB3-CB or VB6-CB. FRAP recordings were performed with a Zeiss confocal laser scanning microscope (CLSM 510 Meta) in combination with the LSM510 4.0 SP2 software. Images were acquired using a 488 nm Argon laser and 63 x magnification. For photobleaching the laser was set to 50 % output and 100 % transmission to bleach a 5 x 5 µm region of interest for 1.7 s. Confocal imaging series were acquired with 1 % laser transmission and the pinhole opened to 1.5 Airy units. Generally, 5 prebleach and 145 postbleach images were recorded with 294 ms time intervals. Normalized mean fluorescence intensities were corrected for background and for total loss of fluorescence over time. Fluorescence recovery curves were fitted with Origin 7.5 using an exponential function, given by $I(t) = A\left(1 - e^{-kt}\right)$, where *I(t)* is the signal intensity dependent on time, *A* is the end value of intensity, *k* is the time constant. Half-times of recovery were determined by $t_{1/2} = \frac{\ln 0.5}{-k}$. For statistical analysis two-tailed Student's t-test was used.

2.2.3.12 Time-lapse imaging

For time-lapse series, A549_VB6-CB cells were seeded in µclear 96-well plates in antibleaching DMEM-gfp medium and stimulated with TGF-β (5 ng/ml) for 48 h. Subsequently, TGF-β was removed and cells were cultivated for additional 45 h. Images were acquired in 3 h time intervals with of an ImageXpress micro XL system (Molecular Devices), 40 x magnification in combination with the MetaXpress software (64 bit, 5.1.0.41, Molecular Devices).

2.2.3.13 Image segmentation and analysis

For high content analyses, A549_Actin-CB, Huh7_Actin-CB and A549_VB6-CB were plated in µClear 96-wells plates and treated with TGF-β and/or WFA (see section 2.2.3.2). Images were acquired with an ImageXpress micro XL system and analyzed by the MetaXpress software (64 bit, 5.1.0.41, Molecular Devices). For automated nuclear segmentation, nuclei of live cells were stained by addition of 2 µg/ml Hoechst33258 (Sigma Aldrich) to the cell culture medium. Automated segmentation of vimentin and actin was carried out using the MetaXpress Custom Module Editor (CME 5.1) software (Molecular Devices).

Prior to the segmentation of vimentin, images were processed using a Top Hat filter (size: 30 pixels, shape: circle). Subsequently, a modified version of the "find fibers" tool was applied, based on the fluorescence of VB6-CB to segment vimentin fibers including identification of single segments and branch points. Thereby the following settings were used: minimum fiber width: 0.1 µm, maximum fiber width: 50 µm, intensity above local background (IALB): 150 grey levels. Fibers shorter than 20 fiber length units were excluded from the final readout by applying a filter mask. Nuclei were segmented by means of the "Count Nuclei" tool (fast algorithm, minimum width 6 µm, maximum width 40 µm, IALB 500 grey levels). Eventually, the total number of fiber segments was divided by the number of segmented nuclei of the entire cell population. For each condition ~300 cells were analyzed. Data derived from WFA experiments were normalized to the untreated control (0 nM WFA). Standard errors were calculated from three independent experiments and Student's t-test was used for statistical analysis.

Prior to the segmentation of actin stress fibers, images were processed using a Top Hat filter (size 5 pixels, shape circle). Stress fibers were segmented using an adapted version of the "find fibers" tool based on the fluorescence of Actin-CB. Settings were applied as follows: minimum fiber width: 0.2 µm, maximum fiber width: 5 µm, IALB: 200 grey levels. To identify only straight fibers the ellipsed form factor (EFF = fiber length / fiber width) was calculated and only fibers $\geq$ 3 fiber length units and EFF $\leq$ 5 were included for the final

readout. Nuclei were segmented by means of the "Count Nuclei" tool (fast algorithm, minimum width 6 µm (A549); 7 µm (Huh7), maximum width 40 µm, IALB 500 grey levels). Eventually, the total number of stress fibers was divided by the number of segmented nuclei of the entire cell population. For each condition ~300 cells were analyzed. Standard errors were calculated from three independent experiments and Student's t-test was used for statistical analysis.

3 RESULTS

To generate a chromobody-based cellular system that allows monitoring of endogenous EMT markers multiple steps were required in order to visualize and quantify effects of EMT-targeting compounds by high-content imaging in real time (Figure 3.1). First, the antigens occludin, SNAI1 and vimentin were produced for immunization and nanobody screening (1). Subsequently, alpacas were immunized with the respective antigens (2) and a phagemide library comprising the V_HH repertoire of the immunized animals was generated (3). This library was used to screen for V_HHs (nanobodies), specific for occludin, SNAI1 and vimentin (4). Based on these selections, nanobodies and respective chromobodies were characterized in various biochemical and cell biological assays (5). Finally, chromobody-based cellular systems were generated for high content-imaging (6) and precise algorithms were developed and validated to allow quantification of effects of EMT-modulating compounds by means of a phenotypic high-content imaging readout (7).
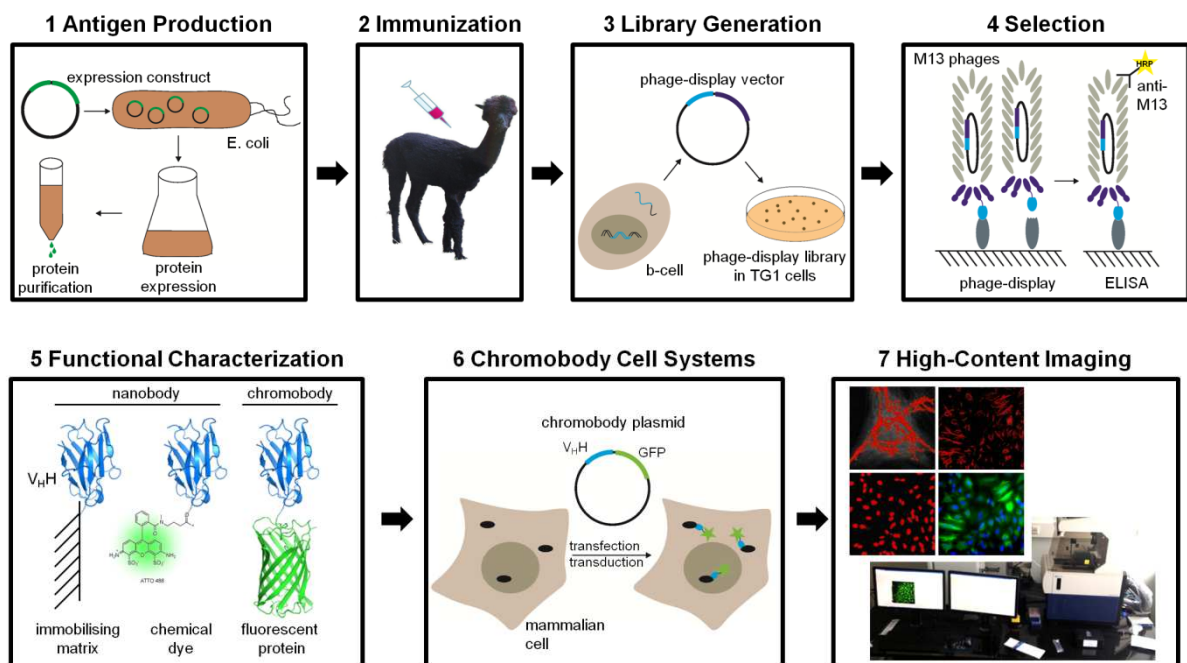

Figure 3.1: Schematic overview of the development and applications of nanobodies and chromobodies specific for EMT marker proteins.

3.1 Selection of single domain antibodies (nanobodies) against the EMT marker proteins occludin, SNAI1 and vimentin

For the development of nanobodies specific for the EMT marker proteins occludin, SNAI1 and vimentin, the antigens required for alpaca immunization were produced. Therefore the cytoplasmic C-terminal domain of occludin (aa372 - aa522) as well as the full-length sequence of SNAI1 and vimentin were fused to a C-terminal His_6-tag (resulting constructs are referred to as OCLN-His_6; SNAI1-His_6, VIM-His_6) and recombinantly produced in *E. coli* BL21. After immobilized metal affinity chromatography (IMAC) followed by size exclusion the three purified antigens were pooled and analyzed by SDS-PAGE followed by staining with Coomassie Brilliant Blue (Figure 3.2). Within ten weeks, one alpaca was repeatedly immunized with the pool of purified antigens. Three days after the last boost ~ 200 ml blood were collected (conducted by Stefan Nüske, LMU Munich), followed by the isolation of peripheral blood mononuclear cells (PBMCs). The cDNA of PBMCs served as template to amplify the nanobody sequences, which were transferred into a phagemide library comprising ~ 2×10^7 cfu/ml, representing the $V_H H$ repertoire of the immunized animal (conducted by Jaqueline Bogner, ChromoTek GmbH).
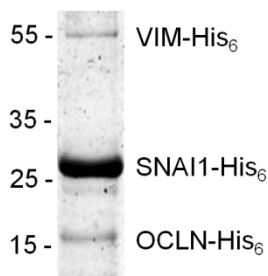

Figure 3.2: Antigens for immunization. Purified antigens VIM-His_6, SNAI1-His_6 and OCLN-His_6 were pooled and 2µg of the pooled fraction was separated by SDS-PAGE, followed by Coomassie staining.

In order to select nanobodies, specific for EMT markers from this library, phage display with two panning cycles, followed by phage ELISA was performed. To this end, the production of phages, expressing the nanobody repertoire as fusions of the pIII coat protein, was induced by infection with the Hyperphage M13K07ΔpIII. For each cycle of biopanning GST-tagged occludin (aa372 –aa522) and SNAI1 (GST-OCLN, GST-SNAI1) as well as VIM-His_6 were passively absorbed to block polystyrene immunotubes and pre-cleared phages were added overnight. Unbound phages were removed, followed by elution of specifically bound phages, which were used to reinfect *E.coli* TG1 cells. To test the specificity of the enriched clones, at least 47 monoclonal phages per antigen were analyzed by solid-phase phage ELISA. Therefore, the antigens as well as the control proteins GST for GST-tagged proteins and GFP-His_6 for His_6-tagged proteins were coated on 96-well microtiter plates. Later on, binding of the monoclonal phage clones was detected with a HRP-conjugated antibody, specific for the

M13 coat protein (Figure 3.3). The results show that for occludin 31 positive clones with signals at least five-fold higher than the respective negative control were identified (Figure 3.3 A), while for SNAI1 23 and for vimentin 21 positive clones were obtained (Figure 3.3 B and C). This indicates a successful selection of EMT marker specific nanobodies.
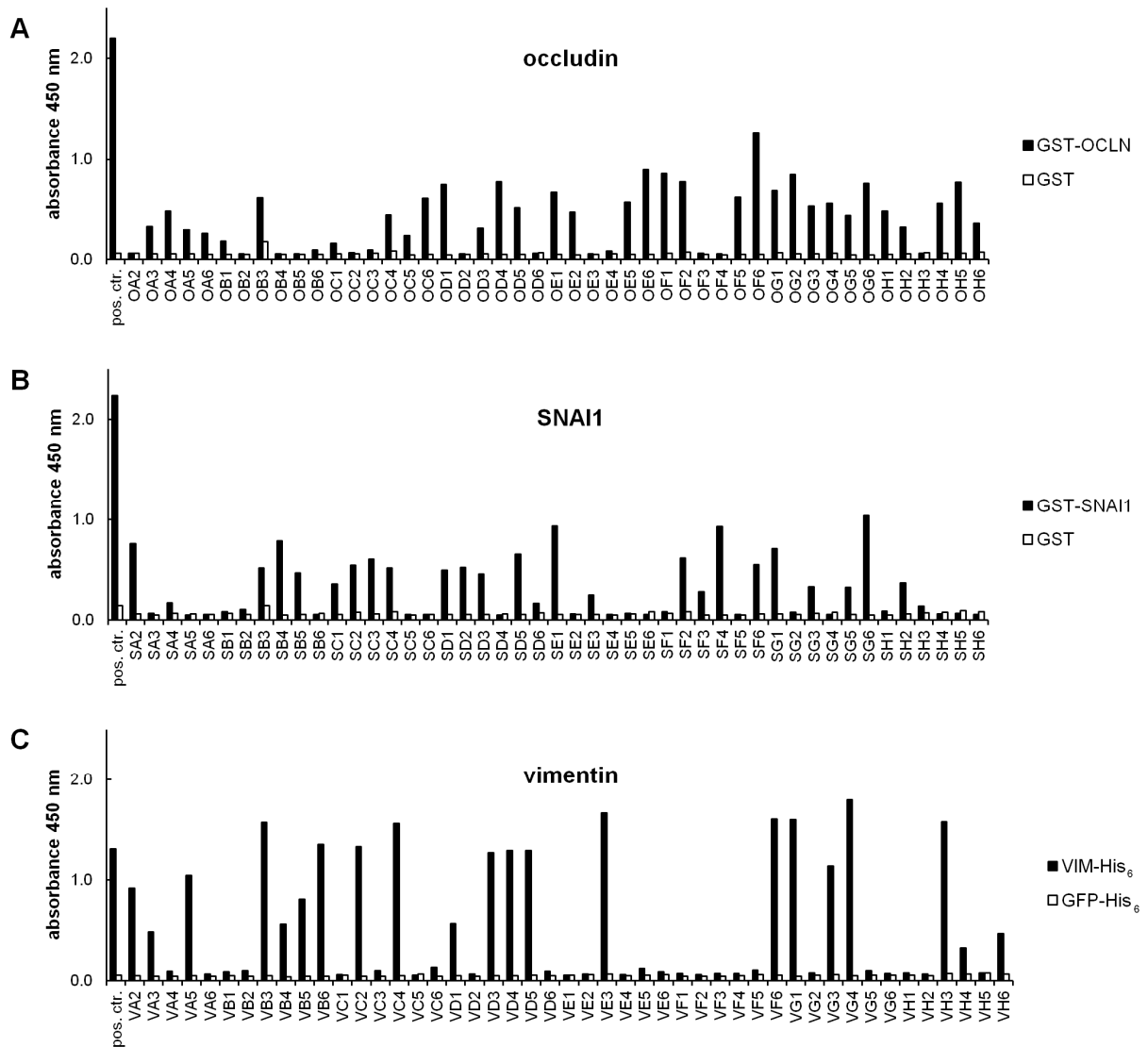

Figure 3.3: Profile of ELISA measurements of eluted phage clones binding to occludin, SNAI1 or vimentin. (**A**) Occludin: Purified GST-OCLN, RFP (pos. ctr.) or GST (neg. ctr.) was immobilized on a 96-well microtiter plate and 47 enriched monoclonal phages resulting from biopanning against occludin (aa372 - aa522) were tested by ELISA. (**B**) SNAI1: Purified GST-SNAI1, RFP (pos. ctr.) or GST (neg. ctr.) was immobilized on a 96-well microtiter plate and 47 enriched monoclonal phages resulting from biopanning against full-length SNAI1 were tested by ELISA. (**C**) Vimentin: Purified VIM-His$_6$, RFP (pos. ctr.) or GFP-His$_6$ (neg. ctr.) was immobilized on a 96-well microtiter plate and 47 enriched monoclonal phages resulting from biopanning against full-length vimentin were tested by ELISA. (**A-C**) Phages expressing a V$_H$H specific for RFP served as positive control (pos.ctr.) For detection an HRP-conjugated α-M13 phage antibody was used. Shown is the absorbance measured at 450 nm.

RESULTS

Since, due to the enrichment process, some of the identified positive ELISA clones might comprise identical amino acid sequences, analyses of all positive nanobody sequences were performed. The alignment of the protein sequences resulted in two unique occludin-nanobodies (OF6-NB and OG1-NB), six unique SNAI1-nanobodies (SA2-NB, SB4-NB, , SG1-NB, SG6-NB, SF2-NB and SF4-NB) and eight unique vimentin-nanobodies (VB3-NB, VB6-NB, VC4-NB, VF6-NB, VE3-NB, VG1-NB, VG4-NB and VH3-NB) (Figure 3.4). From previous studies it is known that $V_H H$ domains carry hydrophilic amino acids in framework 2 (FR2) instead of the highly conserved hydrophobic amino acids of V_{HS} that promote the interaction with the V_{LS} of conventional IgGs (Muyldermans et al., 1994, Harmsen et al., 2000). These substitutions at the positions V37F/Y, G44E/Q, L45R and W47G/L were described as so-called hallmark residues (Vu et al., 1997). While all occludin and SNAI1-nanobodies, as well as the vimentin-nanobodies VB3-NB, VE3-NB, VF6-NB and VG1-NB were verified as $V_H H$ domains, closer inspection of the hallmark residues revealed that VB6-NB, VC4-NB, VG4-NB and VH3-NB are V_H domains most likely derived from conventional IgGs.

The two occludin-nanobodies OF6-NB and OG1-NB are highly similar and differ in only seven amino acids located mainly in the CDR1 (Figure 3.4 A). Unlike SNAI1 and vimentin-nanobodies, OF6-NB and OG1-NB exhibit an extended CDR3 loop comprising 14 amino acids, including an additional cysteine residue. These observations have already been described for other $V_H H$ domains suggesting a compensation of the lacking light chain by an extended CDR3 that is stabilized by an additional disulfide bond between FR2 and CDR3 (Muyldermans et al., 1994, Desmyter et al., 1996, Conrath et al., 2003).

Sequence analyses of the six unique SNAI1-nanobodies revealed that the CDR1 regions are rather heterologous, while CDR2 and CDR3 differ in maximally one amino acid (Figure 3.4 B). In addition, minor varieties in the framework regions exist.

As mentioned previously, only VB3-NB, VE3-NB, VF6-NB and VG1-NB are $V_H H$ domains derived from heavy-chain-only antibodies (hcAbs), while VB6-NB, VC4-NB, VG4-NB and VH3-NB are V_{HS} derived from conventional IgGs of the immunized animal. Apart from relatively divers CDR1s and few single amino acid exchanges the $V_H Hs$ are broadly homologous. By contrast the CDRs of the V_{HS} are rather diverse and show small variances in the total sequence length.

A

```
                    FR1                    CDR1           FR2          CDR2                      FR3                                    CDR3              FR4
OF6    QVQLVESGGGLAQPGGSLRLSCAASG FAIDLTTLG WFRQAPGKGREGVS CISASGVA TLYDDSVKGRFTISRDDAKNTVYLQMNDLKPDDTAVYYCAA DGPDKLATDCREDSYDY WGQGTQVTVSS 126
OG1    QVQLVESGGGLVQPGGSLTLSCVASG FTFDLSSMG WFRQAPGKEREGVA CISASGVA TLYDDSVKGRFTISRDDAKNTVYLQMNDLKPDDTAVYYCAA DGPDKLATDCREDSYDY WGQGTQVTVSS 126
       **********.****** ***.*** *::**::::* ******* ****: ******* ********************************************* ***************** **********
```

B

```
                    FR1                    CDR1           FR2          CDR2                      FR3                                 CDR3              FR4
SA2    QVQLVESGGGLVQPGGSLRLSCAFSG FSFDLHAIG WFRQTPGKERELVA AITKGG-K TYHADSVKGRFTISRDKGSNTVYLQMNSLKPEDTAMYYCAA GEVA-------DQGYDN WGQGTQVTVSS 118
SB4    QVQLVESGGGLAQPGGSLRLSCAASG FAIDLITLG WFRQAPGKERELVA AILRGG-K TYHADSVKGRFTISRDKNTNTLYLQMNSLKPDDTGMYYCAA GEVE-------DRGYDN WGQGTQVTVSS 118
SF2    QVQLVESGGGLVQPGESLRLTCVVSG DTLDYYAVG WFRQAPGKERGLIA AITRGG-K TYHADSVKGRFTISRDRVANVVYLQMSGLRPDDTAMYYCAA GEVA-------DQGYDN WGQGTQVTVSS 118
SG1    QVQLVESGGGSVQAGDSLRLSCVASG STAVISAMG WFRQAPGKERSLIA AITRGG-K TYHADSVKGRFTISKDKTANTVYLQMRLLQPEDTAIYYCAA GEVE-------GRGYDN WGQGTQVTVSS 118
SF4    QVQLVESGGGLVQAGGSLRLSCAASR --SDLGAMG WYRQAPGKERVLVA AILRGG-K TYYDDSVRGRFTISRDKNTNTLYLQMDNLNADDTAMYYCAA GEVE-------GRGYDN WGQGTQVTVSS 118
SG6    QVQLVESGGGSVQAGGSLRLSCVVSG NIFSLNAMG WYRQAPGKERELVA AILRGG-K TYHADSVRGRFTISRDKNTNTLYLQMNNLKPDDTGMYYCAA GEVE-------DRGYDN WGQGTQVTVSS 118
       ********** .*.* ****:*. *      ::* *.**:***** *:* ** :** * **: ***:*****:*: :*.****  *..:**.:***** ***      .:**** **********
```

C

```
                    FR1                    CDR1           FR2          CDR2                      FR3                                 CDR3              FR4
VB3    QVQLVESGGGSVQAGDSLRLSCAASG NTFSIKVMG WYRQAPGKQRELVA VSTNSGAS VNYANSVKGRFTISIDSVKKTTYLQMNSLKPEDTAVYFCNA YDG---------RYEDY YGQGTQVTVSS 117
VE3    QVQLVESGGGLVQPGGSLRLSCAASG STFRIRTMG WYRQAPGKQRELVA VSTNSGGS VNYADSVKGRFTISIDSVKKTTDLQMNSLKPEDTAVYYCNA YDS---------DYLDY YGQGTQVTVSS 117
VF6    DVQLVESGGGLVEAGGSLRLSCAASG RTFSPYVMG WYRQAPGNQRELVA VSTNSGAS VNYANSVKGRFTISIDSVKKTTYLQMNSLKPEDTAVYFCNA YDG---------RYEDY YGQGTQVTVSS 117
VG1    DVQLVESGGGLVQAGGSLKLSCKASG STYSIHVYG WYRQAPGKQRELVA VSTNSGAS VNYANSVKGRFTISIDSVKKTTYLQMNSLKPEDTAVYFCNA YDG---------RYEDY YGQGTQVTVSS 117

VB6    QVQLVESGGGLVQSGGSLTLTCAASG FTFSAASMR WVRQVPGKGLEWVA TIDGTGAN SYYSESAKGRFTISRDNARNTLRLQMNNLKPDDTAVYYCAN FG-------R-----NY WGKGTQVTVSS 114
VC4    QVQLVESGGGLVQPGGSLRLSCLASG FSFGSYRMH WVRQVPGKGLEWVA GISSGGGT TYYADSVKGRFTISRDNAKNMLYLQMNNLQPEDTAVYYCLG G---------DWAD---- WGQGTQVTVSS 114
VG4    QVQLVESGGGLVQPGGSLRLSCVASG FTFSDYWMY WVRQAPGKGLEWVS GISPGG-T TTYADSVKGRFTTSRDNTRNTLYLQMNELKPEDTAVYYCAK DL------NWVDSDDY WGRGTQVTVSS 118
VH3    QVQLVESGGGLAQPGGSLRLSCAASG FTFSSYAMS WVRQAPGKGLEWVS GITSGGSS TYYASSVKGRFTISRDNTKNTLYLQMDNLKSDDTAVYYCAK A---------WGSASSS RGQGTQVTVSS 117
       :********* .:.*.** *:* ***  ::       * **.**: * *:    *. .   *:.*.***** * *..:: ***:.*::*****:*              *:********
```

```
37    F/Y  (VHH)    V  (VH)         * fully conserved
44    E/Q  (VHH)    G  (VH)         : strongly similar
45    R    (VHH)    L  (VH)         . weakly similar
47    G/L  (VHH)    W  (VH)
```

Figure 3.4: Amino acid sequence alignment of unique nanobodies specific for occludin (A), SNAI1 (B) or vimentin (C). Hallmark residues at the positions 37, 44, 45 and 47 (Kabat numbering (Kabat and Wu, 1991)) of V_HH and V_H sequences are displayed as white letters on black (V_HH) or dark grey (V_H) background and non-identical residues are highlighted in light grey. * indicates positions with fully conserved residues, : indicates conservation between groups of strongly similar properties and . indicates conservation between groups of weakly similar properties.

In summary, biopanning of the phagemide library derived from an alpaca immunized with recombinant occludin, SNAI1 and vimentin and subsequent screening by phage-ELISA, followed by sequence analysis of the positive phage clones resulted in a successful selection of two unique occludin-nanobodies, six unique SNAI1-nanobodies and eight unique nanobodies specific for vimentin.

3.2 Characterization and identification of intracellular functional EMT-chromobodies

For the development of a nanobody-based cellular EMT model, the intracellular functionality of fluorescently labeled nanobodies (chromobodies) is absolutely indispensable. The general strategy to characterize and select suitable EMT nanobodies was therefore to primarily generate so-called "chromobodies" by fusing the coding sequences of all unique nanobodies to fluorescent proteins (e.g. eGFP) (Figure 1.4.). To perform co-localization studies as initial tests, these chromobodies were introduced in mammalian cells, together with expression plasmids coding for the respective antigen, fused to a distinguishable fluorescent protein. Only chromobody candidates that co-localize with the ectopically expressed antigens were selected for further validation by biochemical and cell biological assays, including Western blot, immunofluorescence, immunoprecipitation, intracellular-immunoprecipitation and live-cell imaging.

3.2.1 Occludin-nanobodies and -chromobodies

3.2.1.1 Preselection of occludin-chromobodies

Starting from 31 positive ELISA clones, sequence analysis showed that the two unique sequences of OF6-NB and OG1-NB were strongly enriched. Both nanobodies were genetically fused to eGFP, resulting in OF6- and OG1-chromobody (OF6-CB and OG1-CB), and transiently expressed in mammalian cells. To investigate the intracellular expression and distribution of OF6-CB and OG1-CB, HeLa cells were co-transfected with full-length occludin fused to mCherry (mCherry-OCLN) and one of the chromobody constructs (Figure 3.5 A). The images show that mCherry-OCLN was integrated into the tight-junctions among endogenous occludin and predominately located at the plasma membrane of transfected cells. While OF6-CB co-localized with mCherry-OCLN at the plasma membrane indicating potential intracellular binding of the chromobody to ectopically expressed occludin, OG1-CB showed no co-localization, but was rather diffusely distributed throughout nucleus and cytoplasm (Figure 3.5 A).

In a next step, both chromobodies (OF6-CB, OG1-CB) were single-expressed in MDCK and MCF7 cells (Figure 3.5 B). These epithelial cell lines express high levels of endogenous occludin at the plasma membrane, as illustrated by immunostaining of occludin with a conventional occludin antibody (α-OCLN-IgG). Apart from a very slight accumulation of OF6-CB at the plasma membrane of MDCK cells, both occludin-chromobodies showed a rather diffuse distributional pattern and no resemblance to endogenous occludin. This suggests that only a minor fraction of OF6-CB binds to endogenous occludin in these cells, while OG1-CB does not recognize endogenous occludin at all.
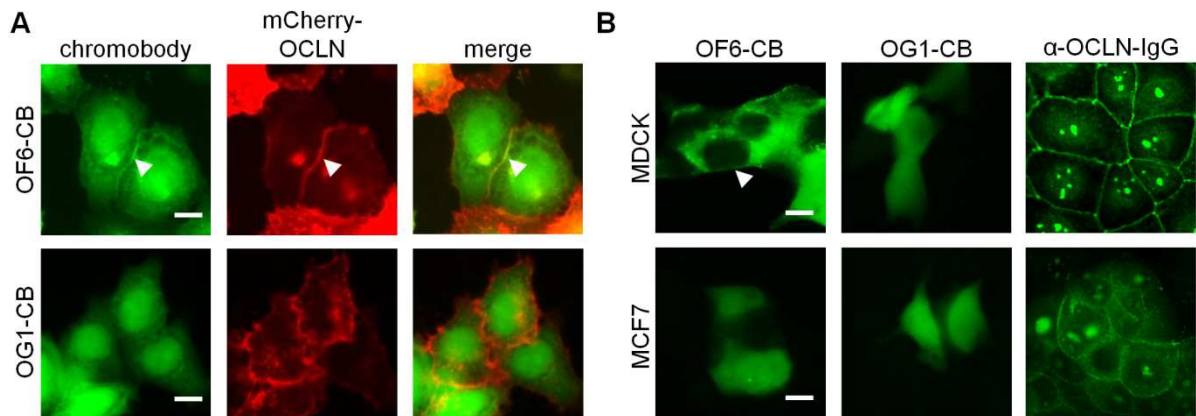
Figure 3.5: Intracellularly expressed occludin-chromobodies OF6-CB and OG1-CB only partially co-localize with their respective antigen. (**A**) Co-localization analysis of OF6-CB (upper panel) or OG1-CB (lower panel) with ectopically expressed mCherry-tagged occludin (mCherry-OCLN). Co-localization sites of OF6-CB and mCherry-OCLN at the plasma membrane are marked by white arrows. (**B**) Co-localization analysis of occludin-chromobodies with endogenous occludin. MDCK cells (upper panel) and MCF7 cells (lower panel) were transfected with OF6-CB or OG1-CB or stained with an anti-occludin antibody (α-OCLN-IgG) as control. The white arrows mark accumulation of the chromobody at the plasma membrane. Shown are representative images from independent experiments (N = 3). Scale bars: 20 µm.

Based on these preliminary results the binding moiety of the OF6-CB, referred to as OF6-NB, was subjected to further biochemical characterization

3.2.1.2 *Functional characterization of OF6-NB/CB*

Occludin is an integral membrane protein that contributes to the stabilization of tight junctions and barrier function of cells (Furuse et al., 1993, Chen et al., 1997). It interacts with numerous binding partners (e.g. ZO1-3, VAP-33, JAM and CLMP) and is tightly regulated by a number of posttranslational modifications, while dysregulation of occludin is often accompanied by diseases such as cancer and inflammatory diseases (Feldman et al., 2005, Raleigh et al., 2011, Beeman et al., 2012). In this context, an occludin-specific nanobody for

biochemical applications would be of particular interest, even if the priority of this work was to identify functional chromobodies for intracellular approaches.

Since OF6-CB has been shown to partially co-localize with ectopically expressed occludin, OF6-NB was found to be a promising candidate for biochemical analyses. To investigate OF6-NB in immunological applications, it was recombinantly produced in *E. coli* XL1 blue. For efficient periplasmic protein expression, the coding sequence of OF6-NB was cloned into the bacterial expression vector pHEN6. The latter is equivalent to the pHEN4 vector (Arbabi Ghahroudi et al., 1997), but carries a C-terminal His_6-tag instead of the HA-tag and geneIII (Conrath et al., 2001). After affinity purification via immobilized metal affinity chromatography (IMAC), followed by size exclusion chromatography, purity of OF6-NB was determined by SDS-PAGE, followed by Coomassie Blue staining. Only fractions with purities higher than 90 % were pooled and used for the following analyses (data not shown).

To test whether OF6-NB is applicable for Western blot, the purified nanobody was chemically coupled to the fluorescent dye ATTO488 provided as N-Hydroxysuccinimide (NHS)-ester (referred as $OF6_{ATTO488}$). For the experimental approach the purified C-terminal domain of occludin (aa372 – aa522) fused to GST (GST-OCLN), as well as soluble lysates derived from HEK293T cells expressing mCherry-OCLN were analyzed by immunoblotting using $OF6_{ATTO488}$ for detection (Figure 3.6 A). Clear signals at the expected sizes of ~ 45 kDa for GST-OCLN and ~ 87 kDa for mCherry-OCLN suggest that $OF6_{ATTO488}$ recognizes a linear epitope located in the C-terminal domain of occludin.
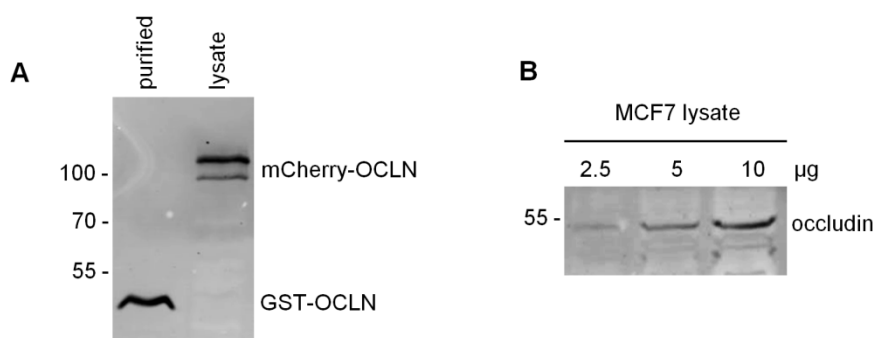

Figure 3.6: Fluorescently labeled OF6-NB recognizes occludin on Western blots. (**A**) Purified recombinant GST-OCLN and full lysates of HEK293T cells expressing mCherry-OCLN were subjected to SDS-PAGE followed by immunoblotting, using OF6-NB, conjugated with the fluorescent dye ATTO488 ($OF6_{ATTO488}$) (N = 3). (**B**) Increasing amounts of soluble protein fractions derived from MCF7 cells were subjected to SDS-PAGE followed by immunoblotting, using $OF6_{ATTO488}$ (N = 3). Shown are representative blots from independent experiments. (N = 3).

In addition, increasing amounts of soluble protein fractions of MCF7 lysates, containing endogenous occludin were separated by SDS-PAGE, followed by immunoblot analysis (Figure 3.6 B). Detection with OF6$_{ATTO488}$ showed signals with increasing intensities in relation to the total amount of loaded protein, as were observed with a conventional occludin antibody (data not shown). This indicates that OF6$_{Atto488}$ is functional to detect denatured endogenous occludin on immunoblots.

During the last years, various immobilized nanobodies have been shown to efficiently precipitate their respective antigens and have been described repeatedly as efficient tools for (co-)immunoprecipitation studies (Rothbauer et al., 2008, Fridy et al., 2014, Traenkle et al., 2015). Consequently, purified OF6-NB was coupled to functionalized sepharose beads, thereby generating a so-called OF6-trap. For immunoprecipitation, whole cell lysates from HEK293T cells, transfected with GFP-labeled occludin (GFP-OCLN) or from MCF7 cells, expressing high amounts of endogenous occludin were incubated with the OF6-trap. Subsequently, input, flow-through and bound fractions were subjected to SDS-PAGE, followed by immunoblotting using antibodies against GFP and occludin for detection (Figure 3.7). The results show that GFP-OCLN (Figure 3.7 A) as well as endogenous occludin (Figure 3.7 B) was precipitated by the OF6-trap and detected in the respective bound fractions. These findings indicate that OF6-NB recognizes and binds endogenous occludin.
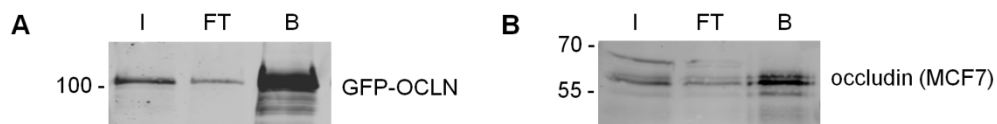

Figure 3.7: Immunoprecipitation (IP) of occludin with OF6-trap (**A**) Immunoprecipitation of ectopically expressed occludin. Whole cell lysates of HEK293T cells expressing GFP-OCLN were incubated with immobilized OF6-NB (OF6-trap). Input (I), flow-through (FT) and bound (B) fractions were subjected to SDS-PAGE, followed by immunoblotting specific, using a GFP antibody for detection. (**B**) Immunoprecipitation of endogenous occludin. MCF7 cells (lower panel) were incubated with the OF6-trap and Input (I), flow-through (FT) and bound (B) fractions were subjected to SDS-PAGE, followed by immunoblotting, using a conventional occludin antibody for detection. (**A, B**) Shown are representative blots from independent experiments (N = 3).

Since initial co-localization studies have shown a potential interaction between the intracellular expressed OF6-CB and occludin, this was studied by a second biochemical assay, called intracellular-immunoprecipitation (IC-IP). For this approach the chromobody is expressed in living cells and forms complexes with its cognate antigen. Subsequently cells are lysed and the chromobody is precipitated, using its fluorescent moiety as an affinity tag. The

bound fraction is analyzed by Western blotting using antigen and chromobody specific antibodies.

To test whether the OF6-CB is functional in IC-IP, HEK293T, cells were co-transfected with mCherry-OCLN and OF6-CB or GFP as negative control. Soluble protein fractions of lysed cells were subjected to pulldown experiments using the GFP-trap to precipitate the GFP moiety of the chromobody as an affinity tag. Subsequently, input, flow-through and bound fractions were analyzed by immunoblotting with antibodies against GFP and occludin. The results show that ectopically expressed mCherry-OCLN as well as endogenous occludin was clearly enriched in the bound fractions of the GFP-trap after pulldown of OF6-CB, compared to the bound fractions of GFP alone (Figure 3.8). This indicates that OF6-CB binds to overexpressed and endogenous occludin in living cells. This is somewhat surprising, since intracellular binding could not be visualized by fluorescence microscopy.
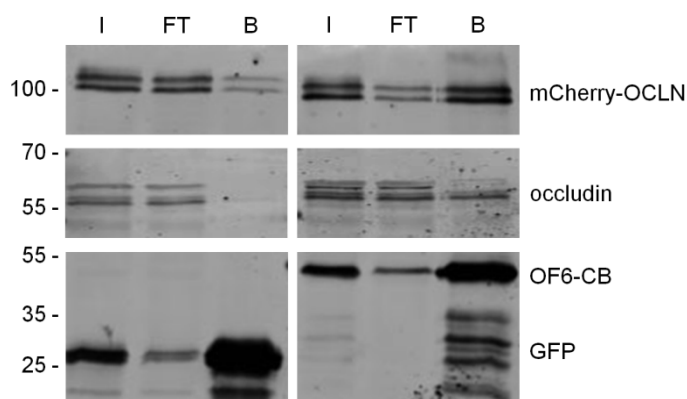

Figure 3.8: Intracellular-immunoprecipitation (IC-IP) of endogenous occludin with OF6-CB. Lysates from HEK293T cells, co-expressing mCherry-OCLN together with GFP (left panel) or OF6-CB (right panel) were subjected to immunoprecipitation using the GFP-trap. Input (I), flow-through (FT) and bound fractions (B) were analyzed by immunoblotting with antibodies against mCherry (upper panel) occludin (middle panel) and GFP (lower panel). Shown are representative blots from independent experiments (N = 3).

Taken together, characterization of the occludin-nanobodies, obtained by phage display, resulted in one functional occludin-nanobody OF6-NB, which is applicable in Western blot and immunoprecipitation. In the chromobody format the OF6-CB binds to occludin in living cells as shown by intracellular-immunoprecipitations. However, image analyses indicated that it is not suited to visualize endogenous occludin in living cells by microscopy.

3.2.2 SNAI1-nanobodies and -chromobodies

3.2.2.1 Preselection of SNAI1-chromobodies

Potential SNAI1-specific nanobodies were converted into the chromobodies SA2-CB, SB4-CB, SF2-CB, SF4-CB, SG1-CB and SG6-CB by genetic fusion of each nanobody sequence to eGFP, as described in the previous section. To investigate the intracellular expression and distribution of all six SNAI1-chromobodies, HeLa cells were transiently co-transfected with mCherry-tagged SNAI1 (mCherry-SNAI1) and one of the chromobody constructs (Figure 3.9 A). Since SNAI1 is a transcription factor and comprises a nuclear localization signal (NLS) (Mingot et al., 2009), ectopically expressed mCherry-SNAI1 was mainly located in the nucleus of transfected cells (Figure 3.9 A). All SNAI1-chromobodies could be readily expressed and co-localized with mCherry-SNAI1 within the nucleus, suggesting potential intracellular recognition of ectopically expressed SNAI1. However, all chromobodies additionally exhibit a diffusive distribution in the cytoplasm of transfected cells (Figure 3.9 A).

To investigate whether the SNAI1-chromobodies indeed recognize endogenous SNAI1, each chromobody as well as GFP was single-expressed in Hela cells (Figure 3.9 B) and the distributional pattern of each chromobody was compared to GFP and to antibody stainings with three different IgG antibodies, specific for SNAI1 (Figure 3.9 C). All SNAI1-chromobodies were distributed throughout the entire cell and showed a slight nuclear accumulation, very similar to solely expressed GFP. Surprisingly, the patterns of the three IgG antibodies α-SNAI1, Sn9H2 and H130 strongly differed from each other, even though they are not stated to address distinct SNAI1 fractions. While α-SNAI1 was mainly located in the cytoplasm of the cells, Sn9H2 showed a clear nuclear staining and H130 equally stained cytoplasm and nucleus (Figure 3.9 C). These observations allow no reliable interpretation of the "real" localization of endogenous SNAI1 and therefore cannot be used for a comparable analysis of the chromobody distributions. In additional studies with A375 cells, a cell line described to express high levels of endogenous SNAI1 (Kajita et al., 2004), similar results were obtained (data not shown).

Based on these findings an additional experimental approach had to be applied to investigate, whether the selected SNAI1-nanobodies recognize and bind SNAI1 in living cells.
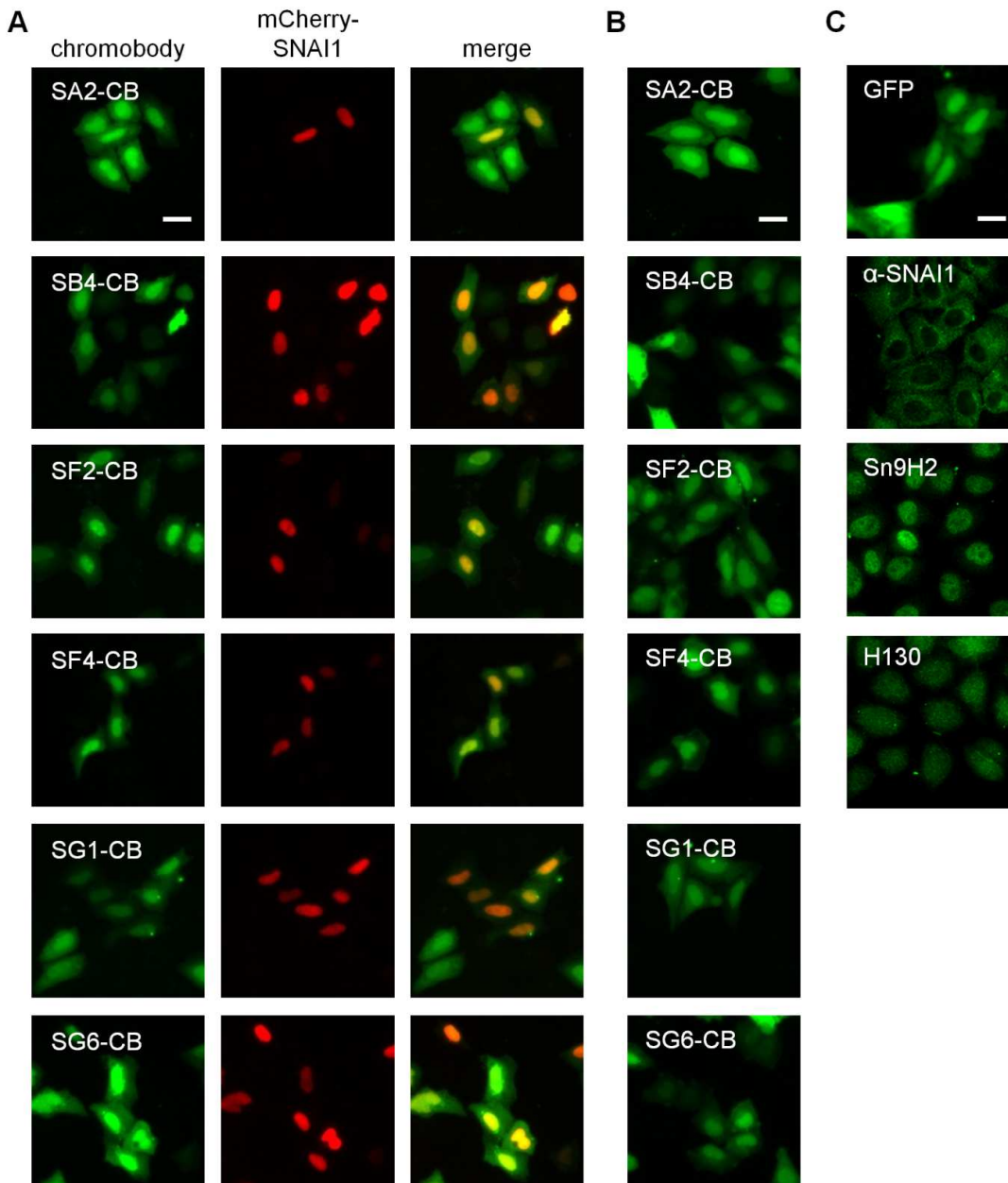
Figure 3.9: SNAI1-chromobodies exhibit no clear intracellular binding. (**A**) Co-expression. HeLa cells were co-transfected with one of the following chromobodies: SA2-CB, SB4-CB, SF2-CB, SF4-CB, SG1-CB or SG6-CB (green) and mCherry-labeled SNAI1 (mCherry-SNAI1, red). (**B**) Single expression of SNAI1-chromobodies in HeLa cells. (**C**) Controls. HeLa cells expressing GFP (GFP) or stained with three different anti-SNAI1 antibodies (α-SNAI1, Sn9H2 and H130). (**A-C**) Shown are representative images from independent experiments (N =3). Scale bars, 20 µm.

Recently, with the so-called fluorescent two-hybrid (F2H) assay, a novel approach to visualize protein-protein interactions in living cells, has been developed (Zolghadr et al., 2008). Based on a modified *lac* repressor system stably integrated into the Baby Hamster Kidney (BHK) cell line, transient transfection of a fluorescently labeled bait construct, comprising the *lac*-repressor (*LacI*), leads to focal enrichment of the fluorescence at a defined

spot. No interaction between bait and prey protein is indicated by a defined spot of the bait protein, but diffuse distribution of the prey construct, labeled with a distinguishable fluorescent protein, whereas an interaction becomes visible as co-localization of both fluorescent signals, derived from the bait and prey protein at the precise spot.

The previous results showed that the SNAI1-chromobodies somehow co-localize with mCherry-SNAI1 within the nucleus of double transfected HeLa cells. This might be due to an intracellular interaction of each chromobody and its antigen, but could also be explained by a coincidental distribution of both constructs. To test, whether the SNAI1-chromobodies directly interact with mCherry-SNAI1 in living cells, a modified F2H assay was applied by performing triple transfection experiments (Figure 3.10).
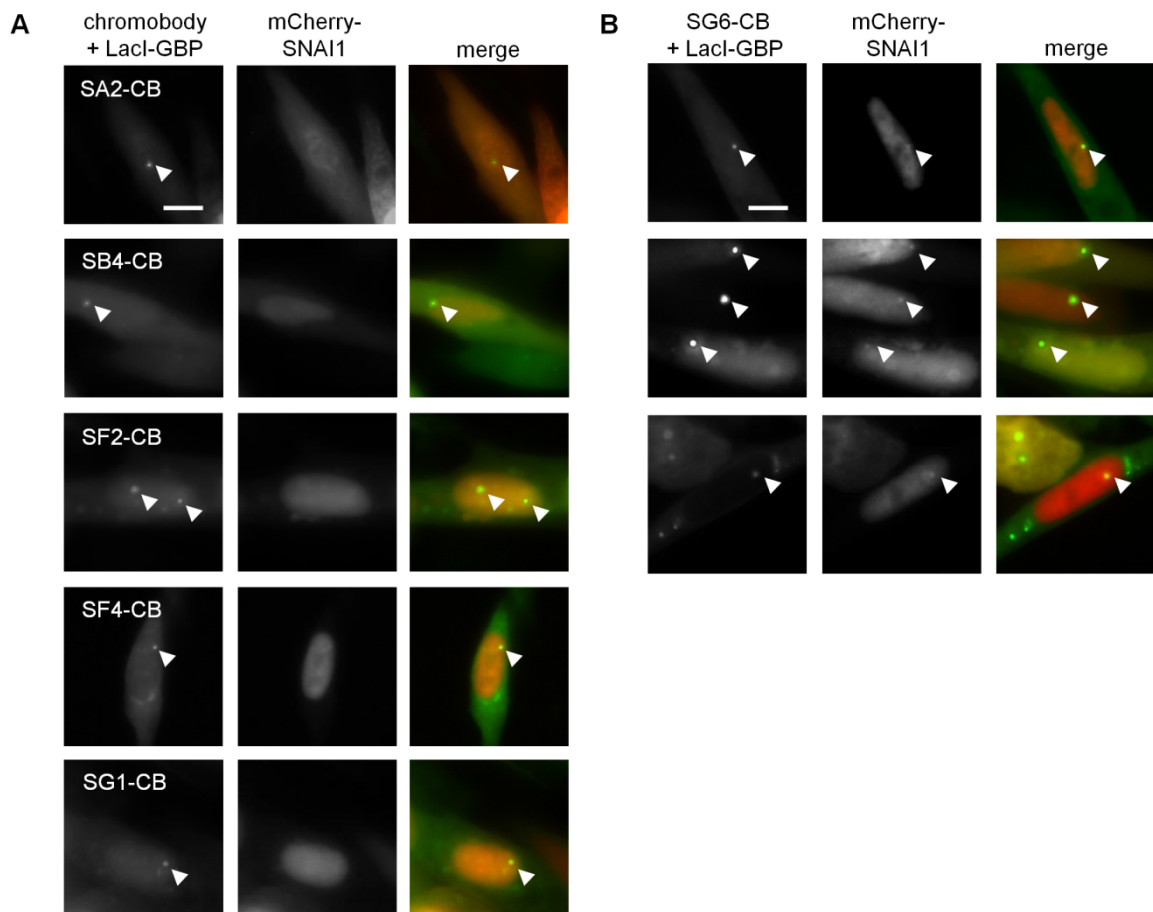

Figure 3.10: F2H analysis of SNAI1-chromobodies SA2-CB, SB4-CB, SF2-CB, SF4-CB, SG1-CB (A) and SG6-CB (B). BHK cells containing lac operator repeats were triple transfected with *LacI*-GBP, one of the chromobody constructs and mCherry-SNAI1. Chromobodies were immobilized to the lac operator array mediated by *LacI*-GBP, resulting in defined spots (highlighted by white arrows, chromobody + *LacI*-GBP). Chromobodies binding to mCherry-SNAI1 can be detected as co-localization of defined spots in both channels (highlighted by white arrows, middle column, mCherry-SNAI1). Shown are representative images from independent experiments (N = 3). Scale bars: 20 µm.

RESULTS

Each chromobody construct (bait) was immobilized to the lac operator array through co-transfection with an invisible construct, comprising the GFP binding protein fused to *LacI* *(LacI*-GBP). Hence, both constructs together (chromobody + *LacI*-GBP) appeared as a distinct green spot in the nucleus. Transfection of the third construct mCherry-SNAI1 (prey) resulted in a dispersed distribution in presence of the chromobodies SA2-CB, SB4-CB, SF2-CB, SF4-CB and SG1-CB, suggesting no interaction between these constructs (Figure 3.10 A). By contrast, transfection of mCherry-SNAI1 and SG6-CB (+ *LacI*-GBP) showed a focal enrichment of both chromobody and mCherry-SNAI1 at the same defined position (Figure 3.10 B). This indicates an interaction between these constructs and strongly suggests that SG6-CB, but none of the other SNAI1-chromobodies, recognizes ectopically expressed SNAI1 in living cells.

3.2.2.2 *Functional characterization of SG6-NB/CB*

To verify intracellular binding of SG6-CB to mCherry-SNAI1, intracellular-immunoprecipitation (IC-IP) was performed. Therefore, HEK293T cells were co-transfected with mCherry-SNAI1 and SG6-CB or GFP as negative control. Soluble protein fractions were subjected to pulldown experiments, using the GFP-trap in combination with the GFP moiety of the chromobody as an affinity tag. Input and bound fractions were then analyzed by immunoblotting with antibodies against GFP (Figure 3.11, lower panel) and mCherry (Figure 3.11, upper panel). The results show that GFP as well as SG6-CB were precipitated in the respective bound fraction. While only a minor amount of mCherry-SNAI1 was detected in the bound fraction of GFP, indicating a slight unspecific interaction between mCherry-SNAI1 and GFP, mCherry-SNAI1 was strongly co-precipitated in the bound fraction of SG6-CB. These findings strongly support the results of the F2H experiments showing that SG6-CB intracellularly binds to ectopically expressed SNAI1. Unfortunately, due to the lack of reliable SNAI1 antibodies, the IC-IP results provide no information, whether SG6-CB also binds to endogenous SNAI1.
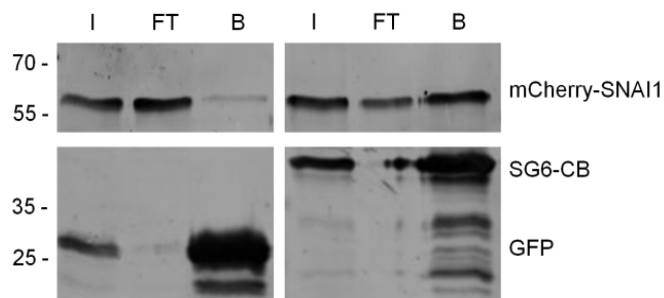

Figure 3.11: Intracellular-immunoprecipitation (IC-IP) of ectopically expressed SNAI1 with SG6-CB. Lysates from HEK293T cells co-expressing mCherry-SNAI1 and SG6-CB or GFP were subjected to immuno-precipitation with the GFP-Trap. Input (I), flow-through (FT) and bound fractions (B) were analyzed by immunoblotting with antibodies against mCherry (upper panel) and GFP (lower panel). Shown are representative blots from independent experiments (N = 3).

Regarding the dissatisfying results for commercially available SNAI1 antibodies, there is a

substantial need for SNAI1 specific binding molecules functional in biochemical approaches including Western blot, immunoprecipation and immunofluorescence. Hence, a nanobody covering these applications would be a highly valuable tool for researchers in this field.

To test whether SG6-NB is functional in the mentioned biochemical applications, the nanobody was produced and purified from bacteria as described for OF6-NB in section 3.2.1.2. Subsequently, purified SG6-NB was immobilized on sepharose beads, thereby generating a so-called SG6-trap. For functionality tests, whole cell lysates of HEK293T cells transfected with GFP-SNAI1 were incubated with the SG6-trap. Subsequently, input, flow-through and bound fractions were subjected to SDS-PAGE followed by immunoblotting (Figure 3.12). The results show that GFP-SNAI1 was only partly detectable in the bound fraction of the SG6-trap. Repeated experiments showed no antigen enrichment in the bound fraction of the SG6-trap under any conditions. From that it may be concluded that there is only a transient interaction between the SG6-NB and SNAI1 or that immobilization of the SG6-NB results in a non-functional binding molecule.
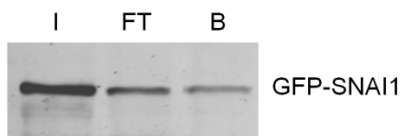

Figure 3.12: Immunoprecipitation (IP) of ectopically expressed SNAI1 with SG6-trap. Whole cell lysates of HEK293T cells expressing GFP-SNAI1 were incubated with immobilized SG6-NB (SG6-trap). Input (I), flow-through (FT) and bound (B) fractions were subjected to SDS-PAGE followed by immunoblotting. Antibodies specific for GFP were used for detection (N = 3).

Finally, the applicability of a fluorescently labeled SG6-nanobody (SG6$_{ATTO488}$) was tested in Western blot and immunofluorescence (IF). Extensive analyses, applying different experimental outlines, showed that SG6$_{ATTO488}$ is not functional in any of these applications (data not shown).

In summary, co-localization studies with SNAI1-chromobodies and mCherry-SNAI1 allowed no reliable interpretation on the functionality of the tested chromobodies. By performing F2H and IC-IP studies, SG6-CB was found to recognize ectopically expressed SNAI1 intracellularly. SG6-NB precipitates low levels of ectopically expressed SNAI1 in IP experiments, but is not applicable for other biochemical applications. Due to the lack of reliable SNAI1 antibodies, it remains unclear, whether SG6-CB also binds to endogenous SNAI1 and consequently SG6-CB was not used any further with regard to the envisaged intracellular EMT studies.

3.2.3 Vimentin-nanobodies and -chromobodies

3.2.3.1 Preselection of vimentin-chromobodies

To preselect suitable candidates, in order to trace morphological changes of vimentin in a cellular EMT chromobody model, potential vimentin specific chromobodies were generated based on the eight unique vimentin-nanobody sequences. Intracellular expression and distribution of all GFP-labeled chromobodies were analyzed in living cells as described for occludin- and SNAI1-chromobodies. Therefore, Hela cells were either co-transfected with mCherry-labeled vimentin (mCherry-VIM) (Figure 3.13 A) or transfected with a single chromobody construct (Figure 3.13 B). Cells expressing GFP only or stained with an IgG antibody against vimentin served as controls (Figure 3.13 C).
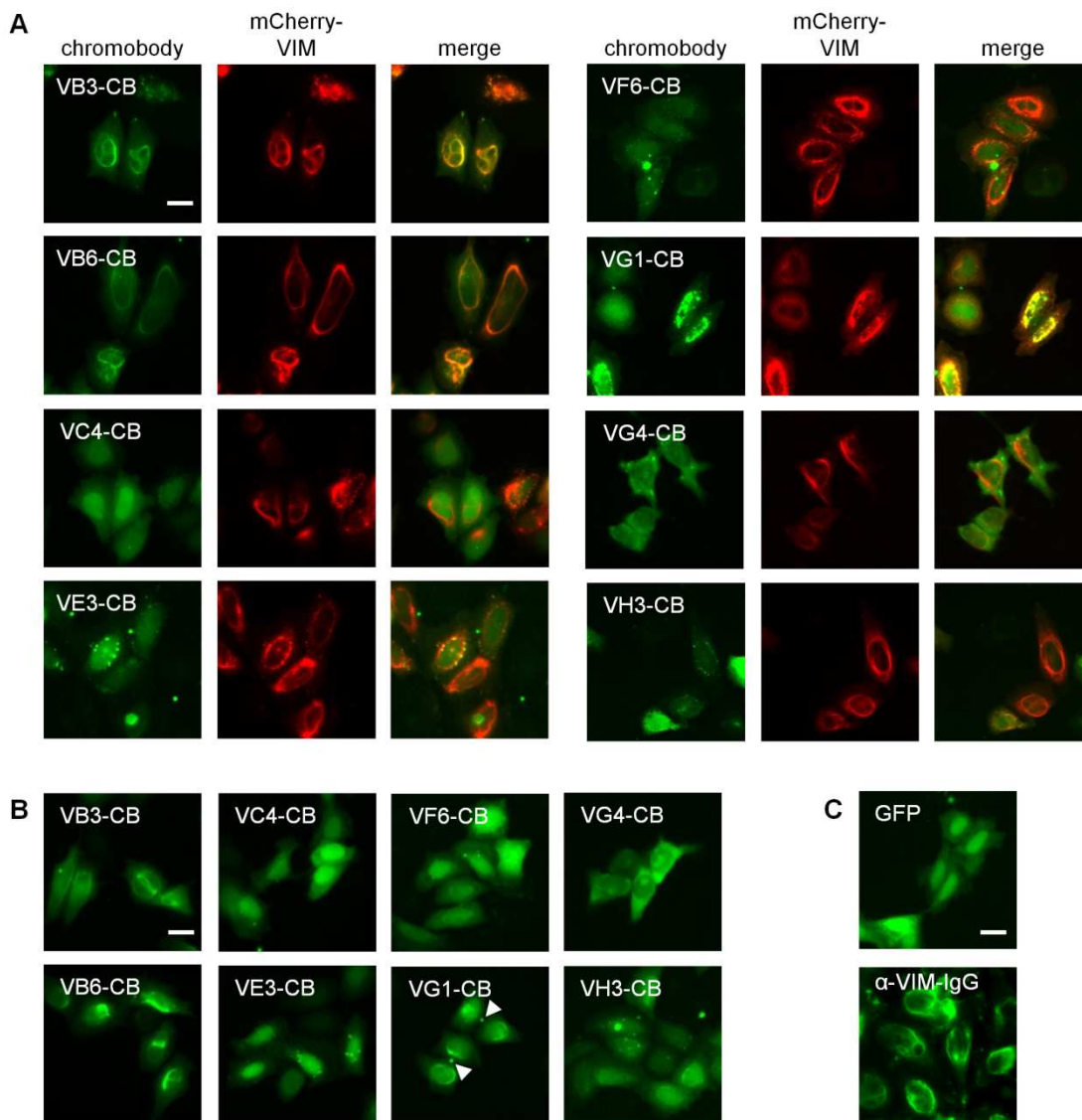

Figure 3.13: Intracellularly expressed vimentin-chromobodies VB3-CB, VB6-CB and VG1-CB co-localize with vimentin. (**A**) Co-localization analysis of chromobodies with ectopically expressed vimentin. HeLa cells were co-transfected with one of the following chromobodies: VB3-CB, VB6-CB, VC4-CB, VE3-CB, VF6-CB,

VG1-CB, VG4-CB or VH3-CB and mCherry labeled vimentin (mCherry-VIM). (**B**) Single expression of vimentin-chromobodies in HeLa cells. Structures, reminiscent of the midbody are marked by white arrows. (**C**) Controls. HeLa cells were transfected with GFP (GFP) or stained with a conventional vimentin antibody (α-VIM IgG). Shown are representative images from independent experiments (N = 3). Scale bars, 20 µm.

Image analysis revealed that mCherry-VIM assembles into endogenous vimentin structures and was localized in perinuclear region of the cytoplasm in the majority of transfected cells. Remarkably, most of the eight chromobody candidates did not co-localize with those structures. While the chromobodies VC4-CB, VF6-CB and VG4-CB were rather diffusely distributed similar to solely expressed GFP, VE3-CB and VH3-CB strongly aggregated independently of presence or absence of co-expressed mCherry-VIM. Only the chromobodies VB3-CB VB6-CB and VG1-CB truly co-localized with mCherry-VIM (Figure 3.13 A) and displayed a filamentous pattern that resembles the distribution of endogenous vimentin in single transfected HeLa cells (Figure 3.13 B). This suggests that these three chromobodies recognize ectopically expressed as well as endogenous vimentin in living HeLa cells. However, for VG1-CB focal enrichment of the chromobody fluorescence between the majority of dividing cells was observed (Figure 3.11 B, white arrows), indicating that VG1-CB recognizes additional structures apart from vimentin (e.g. structures of the midbody reviewed in Steigemann and Gerlich, 2009). Consequently, only VB3-CB and VB6-CB were identified as most promising candidates for the following biochemical and cell-biological studies.

3.2.3.2 *Biochemical characterization of vimentin-nanobodies VB3-NB and VB6-NB*

In the previous section VB3-CB and VB6-CB were identified as potential vimentin-chromobodies for the intracellular envisaged applications. Since the assumption that the chromobody binding moieties VB3-NB and VB6-NB recognize vimentin, is based on optical microscopic analysis only, the following section focuses on detailed characterization of both nanobodies on a biochemical level. To this end, VB3-NB and VB6-NB were recombinantly produced and purified as previously described for OF6-NB in section 3.2.1.2.

In the first part of the biochemical characterization of VB3-NB and VB6-NB, the purified nanobodies were chemically coupled to the organic dye ATTO488 (VB3$_{ATTO488}$, VB6$_{ATTO488}$) resulting in a degree of labeling (DOL) of 1 for VB3-NB and 0.8 for VB6-NB. To test, whether VB3$_{ATTO488}$ and VB6$_{ATTO488}$ are applicable to detect vimentin in direct immunofluorescence, co-staining experiments with the ATTO488-labeled nanobodies and an established vimentin antibody were performed (Figure 3.14 A-C).

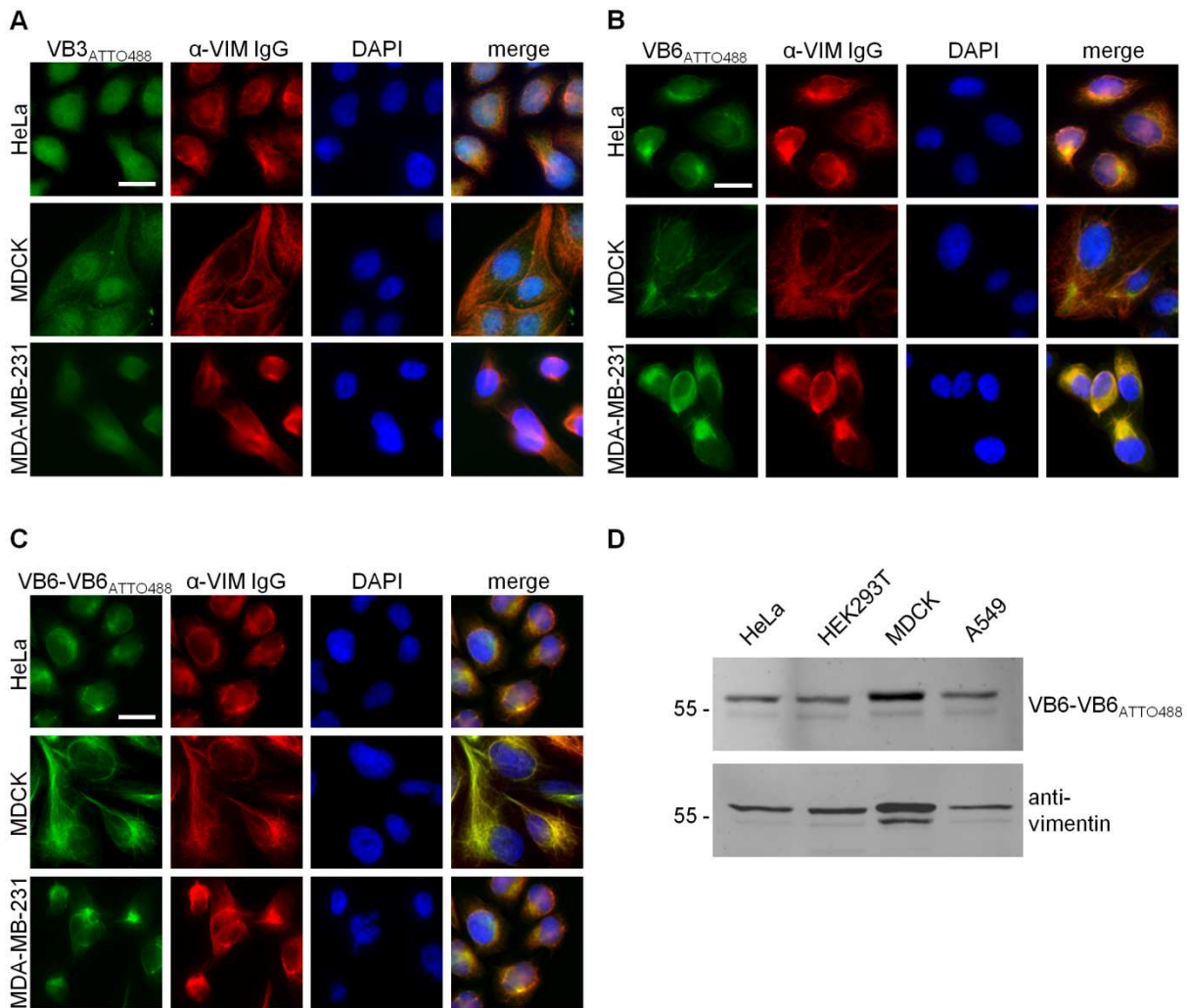**Figure 3.14: Immunofluorescence and immunoblotting with dye-labeled vimentin-nanobodies.** (**A-C**) Co-staining of HeLa, MDCK, and MDA-MB-231 cells with VB3$_{ATTO488}$ (**A**), VB6$_{ATTO488}$ (**B**) and VB6-VB6$_{ATTO488}$ (**C**) together with a conventional anti-vimentin antibody (α-VIM-IgG). HeLa, MDCK and MDA-MB-231 cells were fixed and stained with the respective ATTO488-labled nanobody (green). For co-staining α-VIM-IgG (clone V9) was used (red). Nuclei were stained with DAPI (blue). Shown are representative images from independent experiments (n = 9; N = 3). Scale bars: 20 µm. (**D**) Comparative immunoblot analysis of vimentin using VB6-VB6$_{ATTO488}$ for direct detection or α-VIM-IgG as control. 20 µg of soluble protein fractions derived from HeLa, HEK293T, MDCK or A549 cells were subjected to SDS-PAGE followed by immunoblotting. For detection VB6-VB6$_{ATTO488}$ or α-VIM-IgG (clone V9) were used (N = 4).

For co-staining, three cell lines from different origins were tested: HeLa and MDCK, both originating from epithelial tissue (cervix or kidney) and representing an epithelial phenotype, yet expressing distinct levels of vimentin (Cogli et al., 2013, Phua et al., 2009) and MDA-MB-231, originating from metastatic tissue and frequently described as cell line with a mesenchymal-like phenotype, expressing various mesenchymal marker proteins including vimentin(Vuoriluoto et al., 2011). The results show that VB3$_{ATTO488}$ did not co-localize with α-VIM-IgG, but was rather localized in the nucleus of MDCK cells or diffusely distributed in

nucleus and cytoplasm of HeLa and MDA-MB-231 cells (Figure 3.14 A). By contrast, VB6$_{ATTO488}$ clearly co-localized with α-VIM-IgG in all cell lines, indicating that VB6$_{ATTO488}$ recognizes vimentin in these cells (Figure 3.14 B). In repeating experiments, residual background signals were detected with VB6$_{ATTO488}$. To increase the avidity of the binding molecule, a bivalent nanobody was generated, by connecting two identical VB6 domains by a flexible (Gly$_4$Ser)$_3$ linker. Co-staining with the ATTO488-labeled bivalent nanobody VB6-VB6$_{ATTO488}$ and α-VIM-IgG showed a broad signal overlap at vimentin filaments in all tested cell lines (Figure 3.14 C). Moreover, compared to VB6$_{ATTO488}$, staining with VB6-VB6$_{ATTO488}$ was drastically improved, distinguished by an increase in signal intensity at filamentous structures and a concomitant decrease of unspecific background.

Another application for dye-labeled nanobodies is the direct detection of proteins in immunoblotting. To test whether the vimentin-nanobodies are functional in Western blot, 20 µg of cell lysates from four cell lines expressing differing levels of vimentin were separated by SDS-PAGE, followed by immunoblotting. While in one experiment vimentin was detected with a control vimentin antibody (α-VIM-IgG), in a second experiment VB6-VB6$_{ATTO488}$ was used for detection (Figure 3.14 D). The results show that through direct detection with VB6-VB6$_{ATTO488}$ similar binding patterns as with α-VIM-IgG in combination with a fluorescently labeled secondary antibody were observed, indicating that VB6-VB6$_{ATTO488}$ recognizes denatured vimentin in immunoblotting. No signals in Western blot analyses could be detected with the monovalent nanobodies VB3$_{ATTO488}$ and VB6$_{ATTO488}$ (data not shown).

To extend the biochemical characterization of the vimentin-nanobodies, VB3-NB, VB6-NB and VB6-VB6-NB were covalently immobilized on sepharose beads generating so-called vimentin-traps (VB3-trap, VB6-trap and VB6-VB6-trap). In the following section, these vimentin-traps were tested for their ability to precipitate endogenous vimentin as well as ectopically expressed vimentin domains from a number of cell lysates (Figure 3.15). Equal amounts of the soluble protein fractions derived from HeLa, HEK293T, MDCK and A549 cells were incubated with equal amounts of the indicated vimentin-traps. Input fractions as well as bound fractions were subjected to Western blot analysis to detect possibly precipitated endogenous vimentin (Figure 3.15 A). The results show that all nanobodies bound endogenous vimentin, but with varying efficiencies. The highest amounts of vimentin were detected in the bound fractions of VB3-trap independently of the origin of the lysates. By contrast, both VB6-trap and VB6-VB6-trap, bound only minor amounts of vimentin even though slightly more vimentin was precipitated with VB6-VB6-trap than with the monovalent

RESULTS

VB6-trap. The data resulting from the previous biochemical characterization of the vimentin-nanobodies clearly suggest that both, VB3-NB and VB6-NB, bind to endogenous vimentin. However, it is not explained which domain is addressed by the nanobodies.

In the next step it was analyzed whether VB3-CB and VB6-CB bind to a distinct domain of vimentin. In section 1.2.4 of the introduction, the structure and mechanisms of assembly and disassembly of vimentin filaments are described. Briefly, the vimentin monomer consists of an N-terminal head domain (aa 1 – 95), a central helical rod domain (aa 96 – 407) and a C-terminal tail domain (408 – 488). To identify the binding site of VB3-NB and VB6-NB, the three mentioned vimentin domains were genetically fused to GFP (Figure 3.15 B).
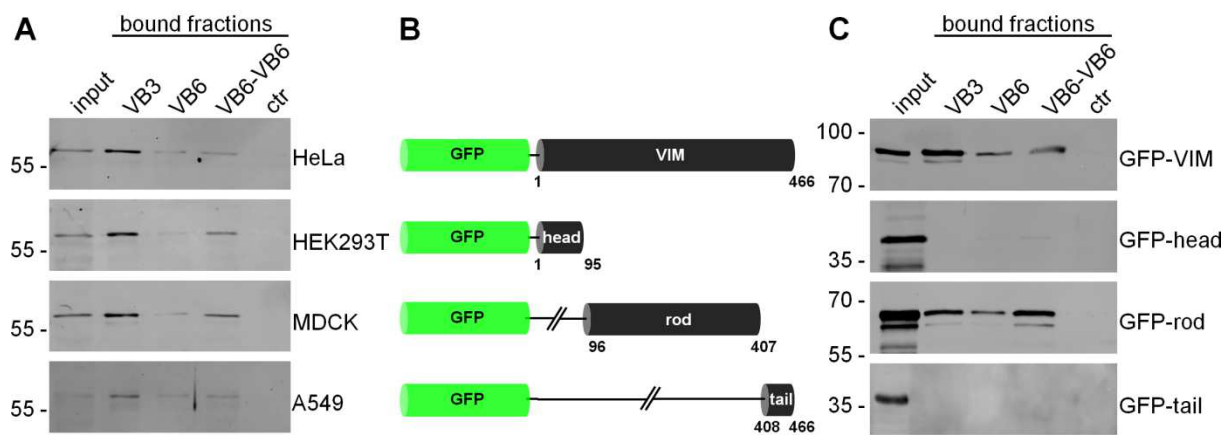

Figure 3.15: Immunoprecipitation of vimentin with immobilized vimentin-nanobodies (vimentin-traps). (**A**) Precipitation of endogenous vimentin. After incubation of the protein lysates from HeLa, HEK293T, MDCK and A549 cells with the VB3-, VB6-, VB6-VB6-trap or a non-related trap (GFP-trap, ctr), input and bound fractions were separated by SDS-PAGE and analyzed by immunoblot with α-VIM-IgG (clone V9). (N = 3). (**B**) Schematic overview of vimentin domains fused to GFP. (**C**) Vimentin domain mapping. HEK293T cells were transfected with the indicated constructs and subjected to immunoprecipitation with vimentin-traps or with a non-related trap (ctr) followed by Western blot analysis of input and bound fractions with an anti-GFP antibody. (N = 3).

For the domain mapping, immunoprecipitation with lysates derived from HEK293T cells expressing the GFP-fusion constructs (Figure 3.15 B) and the immobilized vimentin-nanobodies was performed and respective input and bound fractions were analyzed by Western blot using an antibody against GFP (Figure 3.15 C). As expected, all nanobodies precipitated full-length vimentin. Moreover, the results revealed that all nanobodies also bound to the rod-domain, while none of the nanobodies precipitated the head or tail domain. These findings indicate that the epitopes of VB3-NB and VB6-NB are both located in the rod domain of vimentin.

Taken together, the biochemical characterization of the identified vimentin-nanobodies confirmed that VB3-NB and VB6-NB both recognize endogenous vimentin. Moreover, additional studies, performed by Ulrich Rothbauer, have shown that both nanobodies bind their antigen with high affinities (VB3: 11 nM; VB6: 37 nM) (data not shown). Yet, the two nanobodies differ regarding their applicability for the tested methods. While immobilized VB3-NB efficiently binds natively folded vimentin in immunoprecipitation, VB6$_{ATTO488}$ is more applicable for direct immunofluorescence staining of vimentin in fixed cells. Generation of a bivalent VB6-VB6$_{ATTO488}$ strongly improved the visualization of vimentin by immunofluorescence staining and allowed the detection of vimentin in immunoblotting experiments.

3.2.3.3 *Intracellular characterization of vimentin-chromobodies VB3-CB and VB6-CB*

In section 3.2.3.1 VB3-CB and VB6-CB were shown to visualize vimentin-like filamentous structures in HeLa cells. The subsequent biochemical characterization has proved vimentin as target of both binding molecules. Consequently, the following section focuses on detailed analyses of intracellular binding properties and functionality of VB3-CB and VB6-CB. Thereby, intracellular localization and distribution as well as effects of the chromobodies on cell viability are addressed in particular.

As described previously, intracellular-immunoprecipitation (IC-IP) is a powerful method to analyze chromobody targets in living cells. To test whether VB3-CB and VB6-CB intracellularly bind to vimentin, HEK293T cells were transiently transfected with plasmids coding for VB3-CB, VB6-CB or GFP as a negative control and soluble protein fractions were subjected to pulldown analysis using the GFP-Trap as described in the previous sections. Subsequently, input and bound fractions were analyzed by immunoblotting, using antibodies against vimentin and GFP (Figure 3.16).
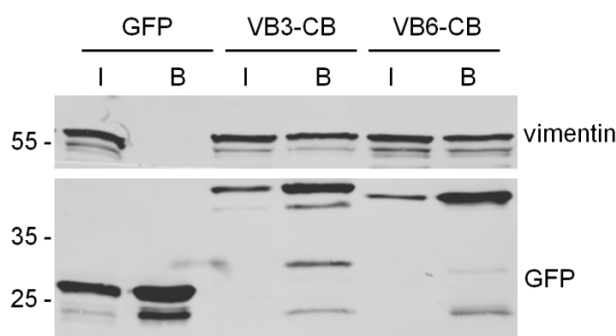

Figure 3.16: Intracellular-immunoprecipitation (IC-IP) of vimentin. Lysates of HEK293T cells expressing indicated chromobodies (VB3-CB; VB6-CB) or GFP were subjected to immunoprecipitation with the GFP-Trap. Input (I) and bound fractions (B) were analyzed by immunoblot with α-VIM-IgG (upper panel) and anti-GFP antibody (lower panel). Shown are representative immunoblots from independent experiments (N = 3).

RESULTS

Detection with a GFP antibody (lower panel, GFP) clearly exhibits the enrichment of GFP as well as both chromobodies in the respective bound fractions. Moreover, the results show that vimentin was co-precipitated with VB3-CB and VB6-CB, while no vimentin was detected in the bound fraction of the negative control (upper panel, vimentin). This indicates specific binding of both chromobodies to vimentin upon intracellular expression.

To test whether intracellular chromobody expression might have cytotoxic effects, cell viability was measured by performing a resazurin-based assay. To this end, A549 cells were transfected with plasmids coding for VB3-CB, VB6-CB or GFP as control and grown in culture media, while resazurin was added 72 h after transfection. Since viable cells continuously reduce the blue colored resazurin to the red colored resorufin, cell viability, deduced by this color change was measured after 1 h incubation with resazurin (Figure 3.17). The results show that compared to the control (GFP) no significant changes in cell viability could be determined for VB3-CB and VB6-CB.
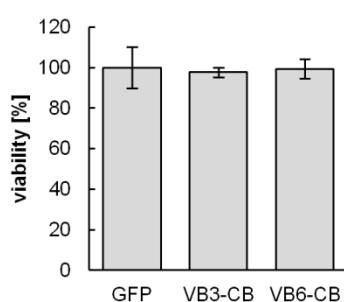

Figure 3.17: Resazurin assay. A549 cells were transiently transfected with VB3-CB, VB6-CB or GFP, grown for 72 h and incubated with resazurin reagent for 1 h at 37 °C. Absorbance was measured at 570 nm and 600 nm. Depicted viability values represent relative mean fluorescence intensities and standard deviation determined for transfection triplicates (± stds). Viability of GFP-transfected cells was set to 100 %. For statistical analysis Student's t-test was used.

As mentioned above, a considerable number of studies on vimentin currently rely on fluorescently labeled vimentin (Chang et al., 2009, Kajita et al., 2014). However, it has been reported that ectopic expression of vimentin induces changes in cell shape, motility and adhesion and therefore might not reflect the distribution and dynamic organization of endogenous vimentin (Mendez et al., 2010). To compare the intracellular distribution of the vimentin-chromobodies and fluorescently labeled vimentin (GFP-VIM), a statistical relevant number of HeLa cells expressing GFP-VIM, VB3-CB or VB6-CB were analyzed by fluorescence imaging (Figure 3.18). All constructs visualized filamentous structures, but a large number of cells expressing GFP-VIM exhibited bright fluorescent granules, resulting from unspecific accumulation of overexpressed protein (Figure 3.18 A). Statistic evaluation, including the information of more than 300 cells per construct, revealed that GFP-VIM formed aggregates in ~ 80 % of transfected cells, while the percentage of cells with fluorescent granules was significantly decreased upon expression of VB3-CB (~ 25 %) or VB6-CB (~ 14 %) (Figure 3.18 B).
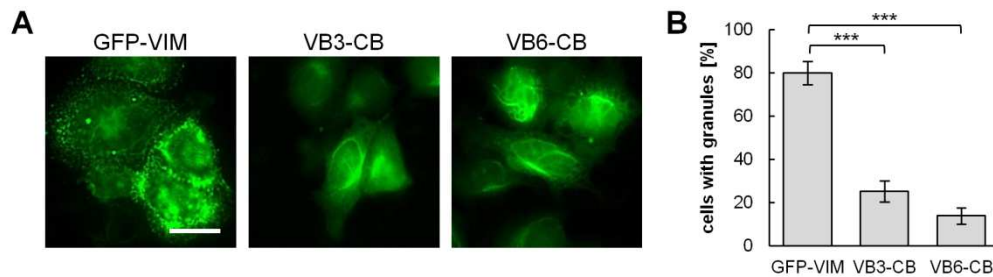
60

Figure 3.18: Vimentin-chromobodies have a low tendency to aggregate upon intracellular expression. (**A**) Representative images of HeLa cells expressing GFP-VIM, VB3-CB or VB6-CB from three independent experiments. Scale bar: 20 µm. (**B**) Quantification of cells with fluorescent aggregates upon expression of GFP-VIM, VB3-CB or VB6-CB. Columns represent the percentage of cells displaying fluorescent granules (total number of analyzed cells > 300). Values represent the means of three independent transfections ± stds. For statistical analysis Chi-squared test was used, ***P < 0.001.

During the last decade, it has been shown that chromobodies with transient binding properties are highly suited for intracellular visualization of endogenous proteins, since transient binding is likely to be accompanied by minimal interference with the distribution and function of the target structures (Rothbauer et al., 2006). For intrabodies targeting other cytoskeletal target structures, such as lamin, α-tubulin and F-actin, intracellular binding properties have been investigated by fluorescence recovery after photobleaching (FRAP) (Rothbauer et al., 2006, Cassimeris et al., 2013, Panza et al., 2015). Thereby, small regions within cells expressing a fluorescently labeled intrabody are bleached and fluorescence recovery is measured over time. A fast recovery indicates a transient binding mode, given that the target structure itself exhibits only minor dynamics. Here, FRAP analysis was applied to investigate intracellular antigen-binding dynamics of the vimentin-chromobodies (Figure 3.19).

Defined regions in HeLa cells expressing VB3-CB, VB6-CB or GFP-VIM were photobleached and fluorescence recovery within the indicated regions was measured over time (Figure 3.19 A). In agreement with previous studies, describing a slow turnover of fluorescently labeled vimentin within several minutes (Chang et al., 2009, Helfand et al., 2011), only ~ 10 % of GFP-VIM fluorescence recovered after 30 s. Compared to GFP-VIM, significantly higher total recoveries were determined for both chromobodies. Total recovery obtained for VB3-CB amounted ~ 60 %, while VB6-CB fluorescence recovered to ~ 85 % within the same time period (Figure 3.19 B). This illustrates that the high fluorescence recoveries obtained for both chromobodies reflect a rapid association/dissociation rate and is not due to the dynamic turnover of endogenous vimentin filaments. Nevertheless, the differing total recoveries and half times of recovery measured for VB3-CB ($t_{1/2}$ = 4.3 s) and

VB6-CB ($t_{1/2}$ = 3.9 s) demonstrate a slightly faster recovery rate and indicate a more transient binding mode of VB6-CB compared to VB3-CB. Hence, VB6-CB was selected for all following intracellular applications.
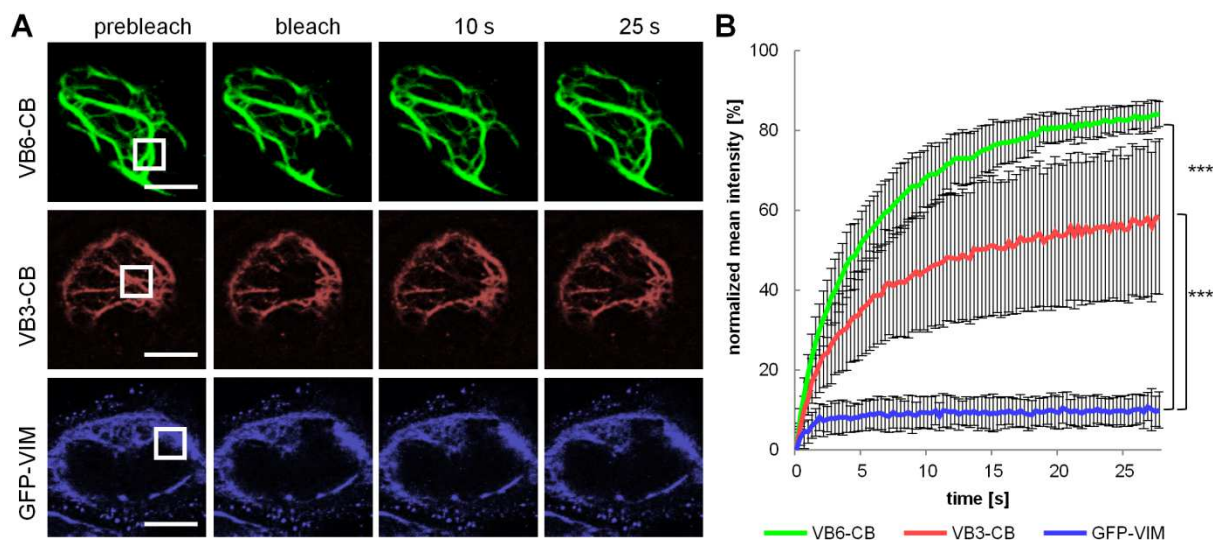

Figure 3.19: Fluorescence recovery after photobleaching analysis of vimentin-chromobodies and GFP-VIM. (A) HeLa cells expressing VB6-CB (green), VB3-CB (red) or GFP-VIM (blue) were photobleached within the indicated regions (white box) and images were recorded over time. Shown are representative pseudo color images before and after photobleaching. Scale bars: 10 µm. **(B)** Quantitative evaluation of FRAP data showing mean values of fluorescence recovery within photobleached regions of ten individual cells. VB6-CB (green) recovered to 84.1 ± 3.1 % with a halftime of 3.9 s, the recovery of VB3-CB (red) amounted to 58.4 ± 19.5 % with a half time of 4.3 s. (n = 10; N = 1). Data are represented as mean ± stds. For statistical analysis students t-test was used, ***P<0.001.

Finally, it was tested whether VB6-CB is suited to visualize vimentin in higher resolution in different cell types. Hence, the chromobody was introduced in various cell lines or cell types including HeLa cells and primary human hepatocytes. VB6-CB expressing cells were subjected to confocal microscopy (Figure 3.20). The images showed a clear outline of cellular vimentin fibers in all tested cells.
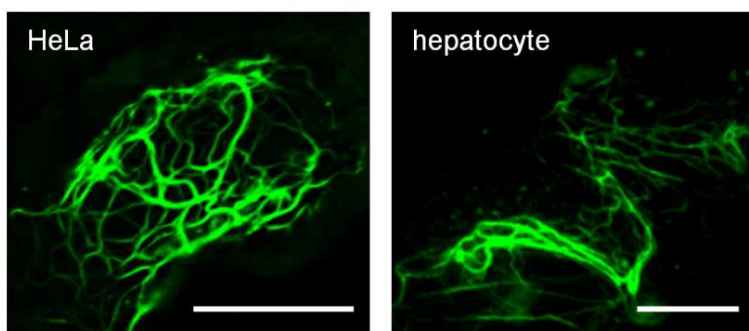

Figure 3.20: Confocal images of a HeLa cell and a primary human hepatocyte expressing VB6-CB. (A) HeLa cells were transfected with VB6-CB coding sequence. **(B)** Primary hepatocytes were transduced with lentiviruses coding for VB6-CB. Shown are representative confocal images from independent transfections/transductions (n = 15; N = 3). Scale bars: 20 µm.

In summary, the results of the intracellular characterization of the vimentin-chromobodies revealed that both, VB3-CB and VB6-CB, recognize vimentin upon intracellular expression. Moreover, both vimentin-chromobodies show no cytotoxic effects and can be solubly expressed in living cells without unspecific accumulation. FRAP analysis revealed that VB6-CB binds to vimentin more transiently that VB3-CB. Since the more transient binding mode of VB6-CB might influence the functionality and dynamic organization of endogenous vimentin to a lower extent, this chromobody was selected for all further intracellular approaches. Taken together, VB6-CB is suggested to be a highly suited novel tool for intracellular imaging of the EMT marker protein vimentin.

3.3 Development of chromobody-based EMT models for high content imaging

As mentioned previously, epithelial-mesenchymal transition (EMT) is a highly dynamic process that occurs during metastasis formation (Richardson et al., 2012, Thiery and Sleeman, 2006, Lamouille et al., 2014). In this context, the identification of novel compounds that modulate EMT during tumor progression is of particular interest for novel therapeutic approaches, targeting the formation of metastases. To date, screening strategies to select novel EMT affecting compounds mainly rely on endpoint readouts regarding gene expression, cell viability and migration (Gupta et al., 2009, Li et al., 2011, Chua et al., 2012). Hence, there is a high demand for assays depicting the dynamics of EMT in disease relevant cellular models in real time.

In the previous sections detailed biochemical and cell biological analyses of novel identified nanobodies and chromobodies against the EMT marker proteins occludin, SNAI1 and vimentin were performed. The data conclude that nanobodies and chromobodies against these cellular targets are applicable as biochemical research tools including Western blot, immunoprecipitation or intracellular-immunoprecipitation. However, image analysis of cells expressing occludin and SNAI1 specific chromobodies indicated that none of these chromobodies are suited to visualize dynamic changes of the respective target structures in cells undergoing EMT. By contrast, characterization of nanobodies and chromobodies against vimentin revealed a broad applicability of these binding molecules to target and trace this EMT relevant target in many biochemical and cellular assays. Remarkably, visualization of endogenous vimentin structures with VB3-CB and VB6-CB now offers new opportunities to study the dynamic EMT process in living cells.

To achieve a more detailed insight into structural changes of the cytoskeleton upon EMT, a previously described chromobody, specifically targeting filamentous actin structures was additionally applied. Recently, the functionality of this commercially available actin-chromobody (Actin-CB, ChromoTek GmbH) has been proved in various eukaryotic systems (Rocchetti et al., 2014, Panza et al., 2015). In the following section, the vimentin specific chromobody VB6-CB as well as the actin specific chromobody Actin-CB were selected for the development of cell-based EMT models.

3.3.1 Vimentin-chromobody-based EMT model

As described in the introduction, vimentin is a mesenchymal marker protein which is not present in primary epithelial cells and shows only minor expression levels in some epithelial derived cancer cell lines. By contrast, vimentin is highly expressed in cells with mesenchymal origin (e.g. fibroblasts) and becomes enriched in epithelial cells, undergoing EMT. Hence, vimentin is a highly relevant EMT biomarker. To monitor dynamic changes of endogenous vimentin in a stable and reliable live-cell system VB6-CB was selected to generate a cell-based EMT model.

During the last decade, the lung cancer cell line A549 has been frequently used to study EMT in tumor progression (Kawata et al., 2012, Liu et al., 2013, Kim et al., 2014, Pan et al., 2015). In this context the well described transforming growth factor β (TGF-β) is widely deployed to induce EMT through SMAD-dependent transcriptional activation (see section 1.3). To study dynamic rearrangements of vimentin during EMT-related processes in living cells, VB6-CB was introduced into A549 cells. Initially tested transient transfection of A549 cells with a VB6-CB coding expression plasmid resulted in strong overexpression of the chromobody in many cells as well as a large heterogeneity regarding intercellular expression levels (data not shown). To achieve more moderate and uniform expression levels, VB6-CB was stably introduced in A549 cells using a lentiviral transduction system. Transduced cells were subjected to selective pressure by adding antibiotics in order achieve stable integration of the VB6-CB sequence in the genome of A549 cells. Single cells, stably expressing VB6-CB and displaying diverse expression levels, were separated into 96-well plates by fluorescence activated cells sorting (conducted by FACS facility, hill campus, University of Tuebingen), to develop a number of monoclonal cell lines. To minimize background fluorescence of unbound chromobody, a cell line with a low overall expression level of VB6-CB (A549_VB6-CB) was selected.

In section 3.2.3.2 it was shown that expression of VB6-CB is not cytotoxic in general. To test whether stable integration of the chromobody construct has an impact on cellular physiology particularly in response to TGF-β stimulation, a set of experiments regarding cell morphology, migration and invasion was performed. Thereby the chromobody cell line A549_VB6-CB was compared to the original A549 wildtype cell line (A549-wt). In a first attempt, A549-wt and A549_VB6-CB were seeded at different densities and stimulated with TGF-β for 72 h (Figure 3.21). Both, A549-wt and A549_VB6-CB cells, underwent morphological changes from a small epithelial cell shape to a larger spindel-like mesenchymal phenotype. Moreover, the morphology of both cell lines did not differ in any of the analyzed conditions.
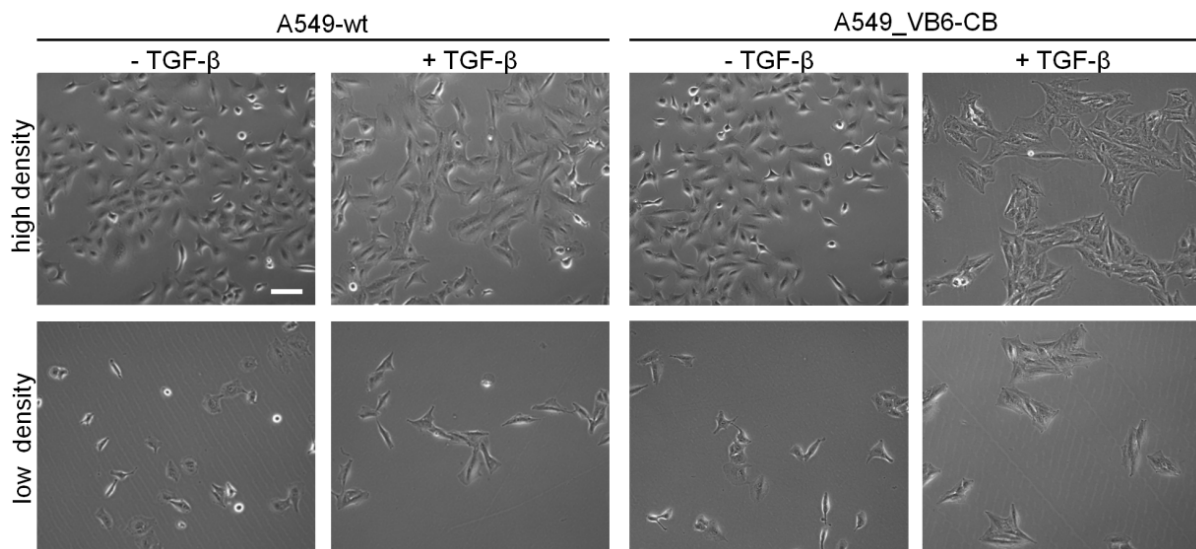

Figure 3.21: Cell morphology of A549-wt and A549 cells in response to TGF-β. A549-wt and A549_VB6-wt cells were plated at high (upper panel) and low densities (lower panel) and left untreated (- TGF-β) or stimulated with 5 ng/ml TGF-β (+ TGF-β). Phase contrast images were taken after 72 h. Shown are representative phase images of independent experiments (N = 5). Scale bar: 100 µm.

In a second attempt, the migratory and invasive potential of A549-wt and A549-VB6-CB cells were compared by performing wound healing and transwell invasion assays (Figure 3.22). For the wound healing assays A549-wt and A549_VB6-CB cells were grown to confluence and open wound areas were determined 24 h and 48 h after wounding in absence or presence of TGF-β (Figure 3.22 A). The results show no significant differences between the two cell lines regarding cell migration. For transwell invasion assays, A549-wt and A549_VB6-CB cells were cultured in polycarbonate transwell inserts and left untreated or stimulated with TGF-β for 48 h. After staining of invading cells with crystal violet, the percentage of invading cells was determined (Figure 3.22 B). While the absolute percentage of invading cells obtained for

RESULTS

A549-wt, under unstimulated as well as under stimulated conditions, was significantly higher than for A549_VB6-CB cells, the relative increase of invading cells in response to TGF-β was nearly identical for A549-wt (~ 2.8 fold) and A549_VB6-CB (~ 2.9 fold).
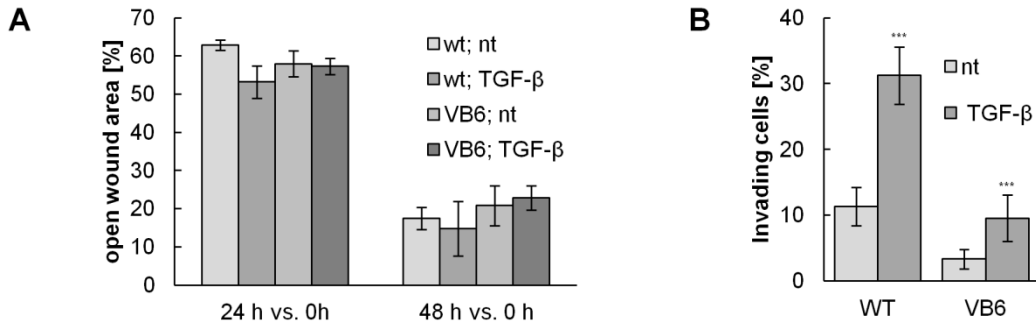

Figure 3.22: Migrative and invasive potential of A549-wt and A549_VB6-CB cells. (**A**) Wound healing assay. A549-wt and A549_VB6-CB cells were grown to 90 % confluence. Scratch wounds were applied and phase contrast images were taken 24 h and 48 h after wounding in the absence or presence of TGF-β (5 ng/ml). Shown are the percentages of the remaining open wound areas after 24 h and 48 h relative to the 0 h values (24 h vs. 0 h and 48 h vs. 0 h, upper panel), (n = 3; N =3). P-values of statistical analysis imply no significant changes (data not shown). (**B**) Invasion assay. A549-wt and A549_VB6-CB cells were cultured in a matrigel-coated transwell insert and left untreated (- TGF-β) or stimulated with 5 ng/ml TGF-β (+ TGF-β) for 48 h. Invading cells were stained with crystal violet. Shown is the percentage of invading cells determined with ImageJ, (n = 9, N = 1). For statistical analysis student's t-test was used.

In combination with results provided by Bjoern Traenkle, showing that the overall response to TGF-β regarding gene expression of the EMT-related marker genes E-cadherin, SNAI1 and Slug is highly similar between A549-wt and A549_VB6-CB cells (data not shown), the obtained data sets clearly indicate that stable insertion of the VB6-CB construct in the genome of A549 cells does not affect EMT-related processes.

To investigate the induction of vimentin in response of TGF-β, A549_VB6-CB cells were left untreated or stimulated with TGF-β for 72 h and vimentin was analyzed via immunoblotting and fluorescence microscopy (Figure 3.23). Soluble protein fractions of respective lysates were separated by SDS-PAGE, followed by Western blot analysis with antibodies against vimentin and GAPDH for detection. Compared to the loading control (GAPDH), only minor amounts of vimentin were detected in non-treated cells, while vimentin protein levels were highly increased in samples upon incubation with TGF-β (Figure 3.2 A). Microscopic analysis of the chromobody fluorescence in A549_VB-CB cells showed only weak fluorescent signals in non-treated cells (Figure 3.23 B). Moreover, in these cells the chromobody was almost exclusively located in the perinuclear region. By contrast, in cells stimulated with TGF-β VB6-CB visualized extended vimentin filaments throughout the entire cytoplasm. These

observations are in accordance with previous studies describing TGF-β-induced rearrangements of vimentin (Tirino et al., 2013). In addition, siRNA experiments performed by Bjoern Traenkle showed that knockdown vimentin was reflected by diffuse distribution of VB6-CB (data not shown).
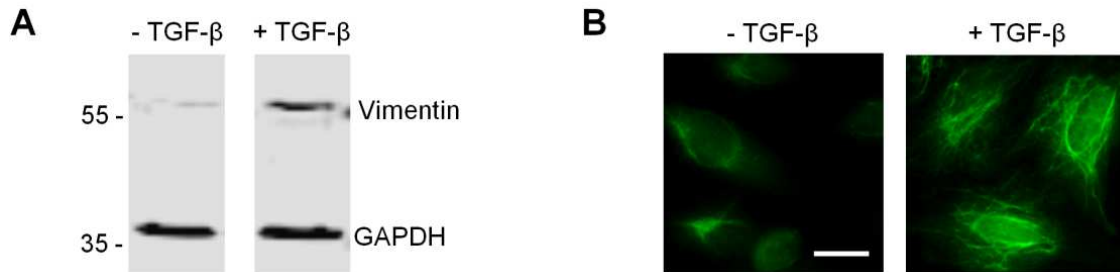

Figure 3.23: VB6-CB visualizes distribution and reorganization of vimentin. (**A**) A549_VB6-CB cells were left untreated (- TGF-β) or stimulated with TGF-β (5 ng/ml) for 72 h. Cell lysates were either subjected to immunoblot analysis with α-VIM-IgG and α-GAPDH antibody (N = 3). (**B**) Fluorescence microscopy of A549_VB6-CB cells left untreated (- TGF-β) or stimulated with TGF-β (5 ng/ml) for 72 h. Shown are representative images (N = 15).

To test whether vimentin rearrangements may also be monitored in real time, time-lapse analysis was applied. To that end, A549_VB6-CB cells were continuously recorded in 3 h intervals over four days. Thereby, TGF-β was added to the culture medium at the beginning of the time series and not removed for 48 h. Subsequently, the culture medium was changed to TGF-β-free medium and left for additional 45 h (Figure 3.24). The results showed a characteristic redistribution of vimentin filaments upon TGF-β stimulation and removal. Thereby, perinuclear vimentin in cells at the beginning of the time lapse (0 h) extended into filamentous fibers throughout the cytoplasm upon treatment with TGF-β up to 48 h. Subsequent removal of TGF-β lead to the reverse process and extended vimentin filaments nearly disappeared after 93 h.
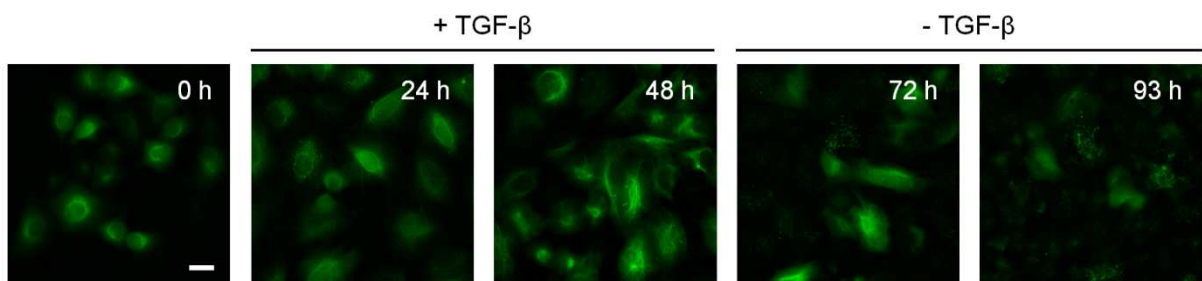

Figure 3.24: Time-lapse microscopy. A549_VB6-CB cells, were stimulated with TGF-β (5 ng/ml) for 48 h. Subsequently, TGF-β was removed and cells were cultivated for additional 45 h. Images were recorded in 3 h intervals, shown are representative images at indicated time points (N = 4). Scale bar: 20 μm.

Taken together, the comparative studies of A549-wt and A549_VB6-CB cells regarding cell morphology, migration and invasion have shown that stable integration of the VB6-CB construct into A549 cells has no impact on the ability of the cells to undergo EMT. Moreover, time-lapse analyses demonstrate that dynamic rearrangements of endogenous vimentin can be readily traced by the chromobody fluorescence on a single cell level. Consequently, the A549_VB6-CB cell line well suited to study vimentin during EMT.

3.3.2 Actin-chromobody-based EMT model

Actin is one of the best described cytoskeletal proteins and plays major roles in cytoarchitecture, cell adhesion and migration (Yamaguchi and Condeelis, 2007, Parsons et al., 2010). During the process of EMT, actin has been shown to relocate from cortical actin at the plasma membrane of epithelial cells to actin stress fibers in mesenchymal cells (Haynes et al., 2011). Recently, an actin specific chromobody has been described to visualize full localization dynamics of endogenous actin in living cells and whole organisms (Panza et al., 2015). Here, the actin-chromobody (Actin-CB) is used to develop EMT-relevant cellular models that can be applied for high-content imaging studies.

To investigate the dynamic distribution of endogenous actin in EMT-related processes, Actin-CB was introduced in two EMT-relevant cell lines: the above described epithelial lung cancer cell line A549 and the epithelial hepatocarcinoma cell line Huh7. While A549 cells are commonly used to study EMT in tumor progression as already described, Huh7 cells are often applied in studies that address EMT during hepatic dedifferentiation (Godoy et al., 2013, Meyer et al., 2013). As explained previously, intracellular expression levels of chromobodies upon transient transfection widely differ within intercellular populations. Hence, A549 and Huh7 cells were transduced by means of a lentiviral system, followed by selective pressure with appropriate antibiotics, in order achieve stable integration of Actin-CB in the genome of the respective cell lines. Similar to the previously described generation of stable A549_VB6-CB cell line, fluorescence-activated cell sorting was performed to obtain polyclonal pools with equal intercellular expression levels. To minimize side effects, due the background fluorescence of unbound chromobody, a cellular pool with relatively low Actin-CB expression levels was selected for A549 and Huh7 cells respectively.

To investigate actin visualization with Actin-CB in the selected cell systems, co-localization studies were performed to compare the distribution of the stably expressed chromobody to classic actin staining with phalloidin. The latter is a natural toxin that binds filamentous actin

with high affinity and serves as a well-established actin probe {Wulf, 1979 #762;Haynes, 2011 #63;Shankar, 2015 #127. Fixed A549_Actin-CB and Huh7_Actin-CB (green) cells were stained with phalloidin-Alexa555 (red) as well as DAPI for visualization of the nuclei (blue) (Figure 3.25 A). Microscopic analyses showed that both, Actin-CB and phalloidin, were clearly enriched at the plasma membrane of A549_Actin-CB and Huh7_Actin-CB cells and broadly co-localized within every cell. This indicates soluble expression of functional Actin-CB in both cell lines and reliable visualization of actin by the chromobody.
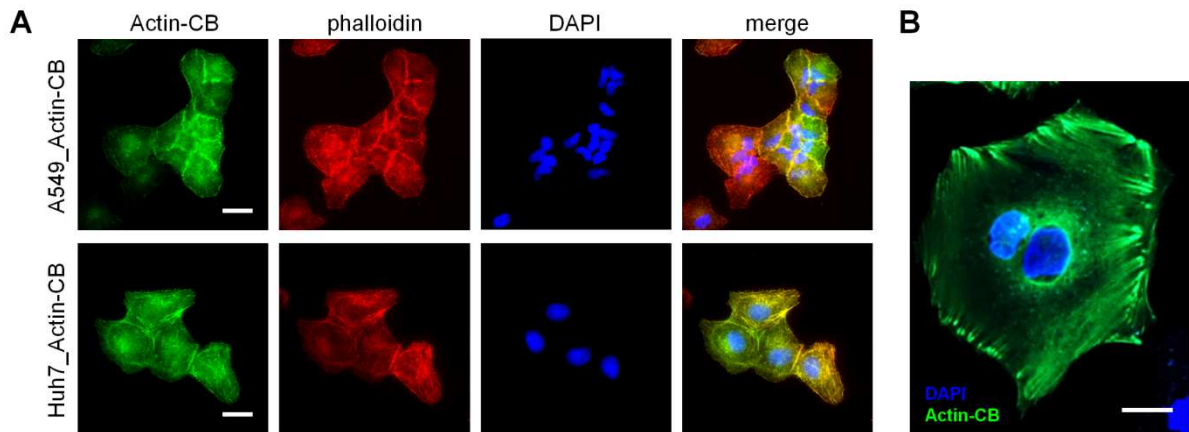

Figure 3.25: Expression of Actin-CB in diverse cell types. (**A**) A549_Actin-CB or Huh7_Actin-CB cells (green) were fixed and stained with phalloidin-alexa555 (red) and Dapi (blue). Shown are representative images of independent experiments (N = 10). (**B**) Primary hepatocyte expressing Actin-CB via lentiviral transduction and stained with DAPI (n = 8; N = 3). Scale bars: 20 µm.

With regard to future studies of EMT during hepatic dedifferentiation, Actin-CB expression was also tested in primary hepatocytes. Introduction of the Actin-CB in these cells was performed by lentiviral transduction. Analyses by fluorescence microscopy showed that Actin-CB visualizes endogenous actin even in primary cells without obvious effects on cell morphology (Figure 3.25 B).

Next, it was tested whether TGF-β-dependent relocalization of actin during EMT can be monitored by means of the cellular actin-chromobody models. To this end, A549_Actin-CB and Huh7_Actin-CB cells were left untreated or stimulated with TGF-β and analyzed by fluorescence microscopy after 72 h (Figure 3.26). Live-cell images showed that in untreated A549_Actin-CB and Huh7_Actin-CB cells, chromobody fluorescence was diffusely distributed within the cytoplasm, but strongly enriched at the plasma membrane outlining the respective localization of endogenous cortical actin. Upon treatment with TGF-β increased formation of actin stress fibers was observed. This suggests that the previously described

characteristic redistribution of actin upon TGF-β-induced EMT {Haynes, 2011 #63} can be traced and monitored by the fluorescence signal of Actin-CB in both cell lines.
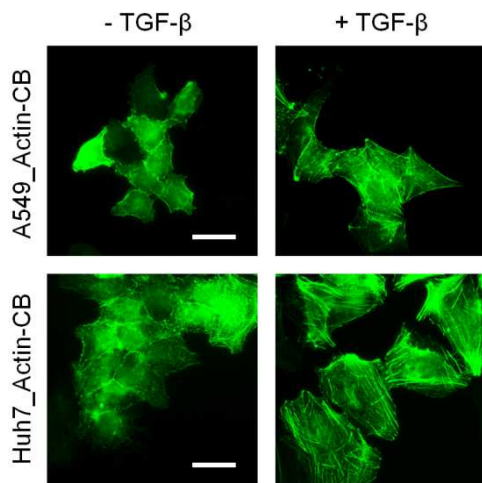

Figure 3.26: Actin-CB visualizes TGF-β induced reorganization of endogenous actin. Fluorescence microscopy of A549_Actin-CB and Huh7_Actin-CB cells left untreated (- TGF-β) or stimulated with TGF-β (5 ng/ml) for 72 h. Shown are representative images of independent experiments (N = 15).

In summary, the results in this section show that the cellular models, A549_Actin-CB and Huh7_Actin-CB, can both be applied to study EMT-relevant dynamic rearrangements of endogenous actin on a single cell level.

3.4 High-content imaging with actin- and vimentin-chromobody models

Currently, most approaches to perform high-content imaging rely on endpoint stainings of fixed and permeabilized samples or on ectopically expressed fluorescently labeled proteins that in many cases do not reflect the distribution and dynamic organization of endogenous proteins. Here, the actin- and vimentin-chromobody models A549_Actin-CB, Huh7_Actin-CB and A549_VB6-CB were adapted for high-content imaging and phenotypic screening in order to quantify morphological changes of endogenous actin and vimentin in a statistically relevant number of cells.

To establish a phenotypic readout based on the fluorescent signals of Actin-CB (Figure 3.27 A) and VB6-CB (Figure 3.27 B), appropriate segmentation masks were developed using the MetaXpress custom module editor (CME). For this, representative images of living A549_Actin-CB, Huh7_Actin-CB and A549_VB6-CB cells cultured in Hoechst-containing medium for nuclear staining were repeatedly analyzed. Thereby distinct parameters were altered to obtain optimized segmentation masks for each compartment. Figure 3.21 A shows a representative raw data image of Hoechst-stained Huh7_Actin-CB cells. Based on the fluorescence signal of Actin-CB in this image, actin stress fibers were automatically

recognized and segmented (Figure 3.27 A', A''). Hoechst staining was used to segment the nuclei (Figure 3.27 A'''), resulting in a final readout comprising the number of stress fibers per cell. For the readout of vimentin, the network of vimentin fibers (Figure 3.27 B') was automatically recognized and segmented within raw data images of Hoechst-stained A549_VB6-CB cells (Figure 3.27 B). Moreover, branch points were detected to separate vimentin fibers into individual fiber segments (Figure 3.27 B'') and nuclei segmentation was performed based on the Hoechst signal (Figure 3.27 B'''). The final vimentin readout comprises the number of fiber segments per cell, thereby allowing the comparison of spatiotemporal changes of vimentin structures among different cellular treatments.
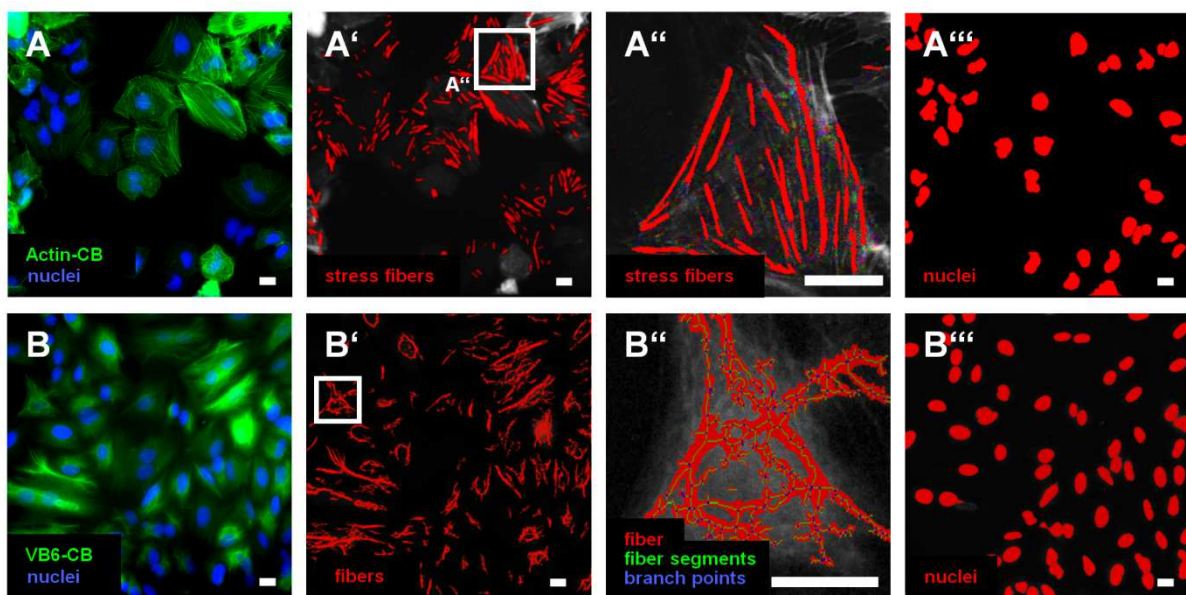

Figure 3.27: Image segmentation of actin- and vimentin-chromobodies for phenotypic readout. (**A**) Representative raw data image of live Huh7_Actin-CB cells showing actin (green) and nuclear staining with Hoechst (blue). (**A'**) Automated segmentation mask of actin stress fibers based on Actin-CB signal using MetaXpress Custom Module Editor (CME) software. (**A''**) Enlarged actin stress fiber segmentation. (**A'''**) Automated nuclei segmentation mask of Huh7_Actin-CB cells based on Hoechst staining. (**B**) Representative raw data image of live A549_VB6-CB cells showing vimentin filaments (green) and nuclear staining with Hoechst (blue). (**B'**) Automated segmentation mask of vimentin filaments based on VB6-CB signal using MetaXpress Custom Module Editor (CME) software. (**B''**) Enlarged segmentation of filament mask (red) including fiber segments (green) and branch points (blue). (**B'''**) Automated nuclei segmentation mask of A549_VB6-CB cells based on Hoechst staining. Scale bars: 20 µm.

To investigate proper applicability of the developed actin-chromobody cell lines, the established readouts were tested to measure the induction of EMT by treatment with TGF-β. A549_Actin-CB and Huh7_Actin-CB cells were left untreated or stimulated with TGF-β and images were recorded after 72 h of treatment. Subsequently, phenotypic actin readout was

applied on the recorded images and the number of actin stress fibers in untreated and stimulated A549_Actin-CB (Figure 3.28 A) and Huh7_Actin-CB (Figure 3.28 B) cells was determined. Quantitative analysis showed a five-fold increase of actin stress fibers in A549_Actin-CB cells (Figure 3.28 A'), while in Huh7_Actin-CB cells the average number of actin stress fibers increased only ~ 3-fold upon treatment with TGF-β (Figure 3.28 B'). Notably, the overall level of actin stress fiber in Huh7 cells was clearly higher than in A549_Actin-CB cells.
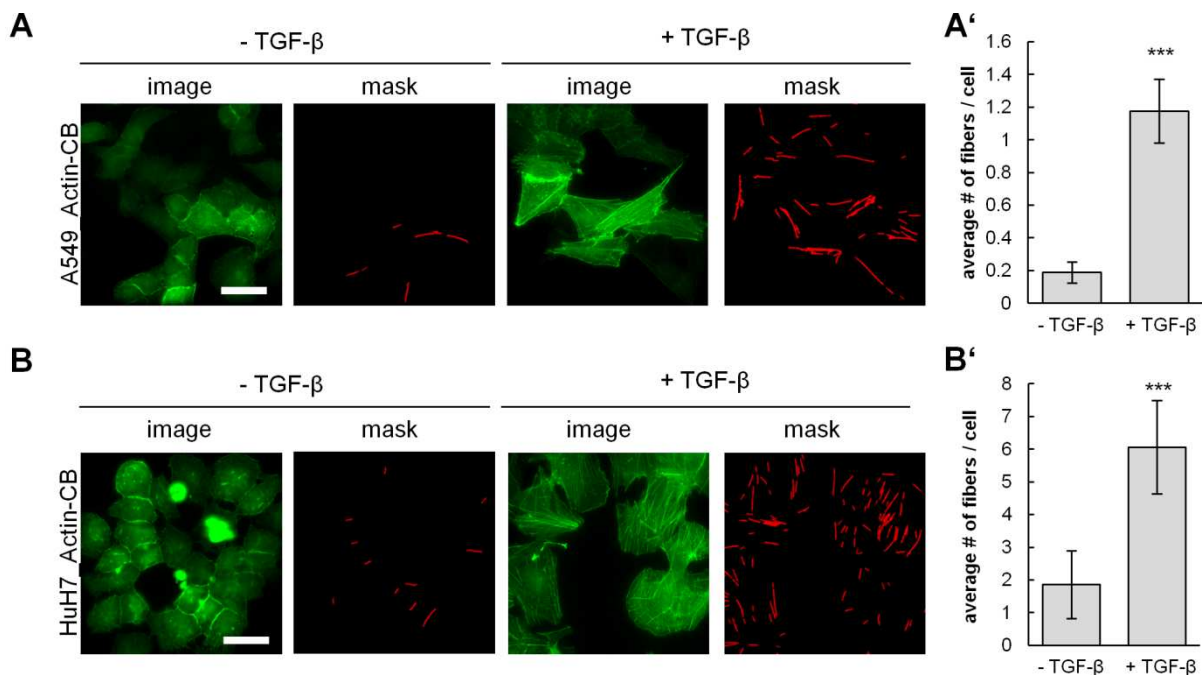

Figure 3.28: Quantitative analysis of actin upon TGF-β treatment. (**A**) Live-cell images of A549_Actin-CB cells left untreated (- TGF-β) or stimulated with TGF-β (5 ng/ml) for 72 h. Shown are raw data images (image) and the respective segmentation of actin stress fibers (mask). Scale bar: 20 µm. (**A'**) Quantification of vimentin fibers in >100 A549_Actin-CB cells under unstimulated (-TGF-β) and stimulated (+ TGF-β) conditions. Values represent the means ± s.e.m. of three independent experiments. For statistical analysis student's t-test was used, ***P<0.001. (**B**) Live-cell images of Huh7_Actin-CB cells left untreated (- TGF-β) or stimulated with TGF-β (5 ng/ml) for 72 h. Shown are raw data images (image) and the respective segmentation of actin stress fibers (mask). Scale bar: 20 µm. (**B'**) Quantification of vimentin fibers in >100 Huh7_Actin-CB cells under unstimulated (-TGF-β) and stimulated (+ TGF-β) conditions. Values represent the means ± s.e.m. of three independent experiments. For statistical analysis student's t-test was used, ***P<0.001.

The vimentin readout was examined in a time-lapse experiment using A549_VB6-CB cells (Figure 3.29). To this end, cells were cultured in absence or presence of TGF-β and fluorescence images were recorded after 24 h, 48 h and 72 h. Segmentation of the recorded images resulted in masks, showing few and small vimentin fibers within images of non-stimulated samples, while visibly more and larger fibers were segmented after 24 h TGF-β

treatment (Figure 3.29 A). Quantification of vimentin fiber segments per cell revealed a seven-fold increase after 24 h stimulation compared to the non-treated control (Figure 3.29 A'). This effect was even increased after 48 h and 72 h treatment, showing spacious vimentin fibers, covering broad parts of the image (Figure 3.29 B, C). Quantitative analysis after 48 h and 72 h treatments resulted in a 10-fold increase of fiber segments per cell compared to the non-stimulated controls (Figure 3.29 B', C').
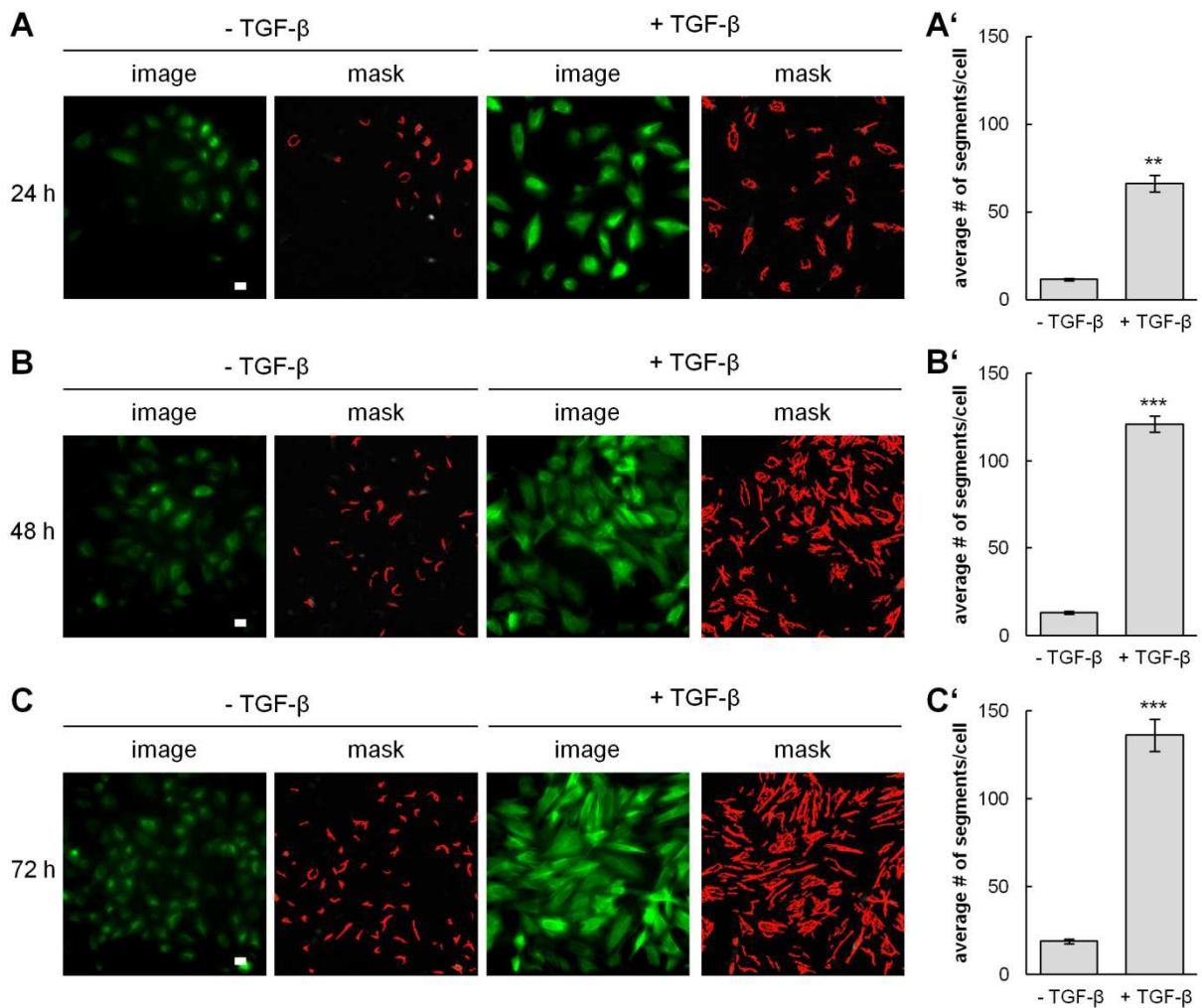
Figure 3.29: Quantitative analysis of vimentin upon TGF-β treatment. (**A-C**) Live-cell images of A549_VB6-CB cells left untreated (- TGF-β) or stimulated with TGF-β (5 ng/ml) for 24 h (**A**), 48 h (**B**) or 72 h (**C**). Shown are raw data images (image) and the respective segmentation of vimentin fibers (mask). Scale bars: 20 µm. (**A'-C'**) Quantification of vimentin fibers in >100 cells after treatment with TGF-β for 24 h (**A'**), 48 h (**B'**) or 72 h (**C'**). Values represent the means ± s.e.m. of three independent experiments. For statistical analysis student's t-test was used, **P<0.01, ***P<0.001.

Finally, it was investigated whether the developed chromobody-based cellular models are suited to study and quantify the effect of EMT modulating compounds. One of the recently described vimentin targeting compounds is the steroidal lactone Withaferin A (WFA) of

RESULTS

Withaferia somnifera. WFA has been shown to exhibit anti-tumor and anti-angiogenesis activity in vivo (Shohat et al., 1967, Mohan et al., 2004) and to covalently modify vimentin by inducing dominant negative effects (Bargagna-Mohan et al., 2007). Moreover, WFA has been described to promote phosphorylation and disruption of vimentin (Thaiparambil et al., 2011) and to inhibit TGF-β induced EMT in epithelial breast cancer cells (Lee et al., 2013). To test whether it is possible to verify effects of vimentin-targeting small compounds by means of the vimentin-chromobody model, real-time high-content imaging upon treatment with WFA was performed. For detailed quantification of the cellular effects upon WFA treatment the phenotypic readout described above was applied.

A549_VB6-CB cells were treated with increasing concentrations of WFA and continuously imaged for 24 h. Thereby effects of WFA were investigated in cells expressing different levels of vimentin, by addition or omission of TGF-β to the culture medium 16 h prior to the incubation with WFA. Quantitative analysis of vimentin fiber segments per cell revealed a time- as well as a dose-dependent reduction of vimentin caused by WFA in absence or presence of TGF-β (Figure 3.30).
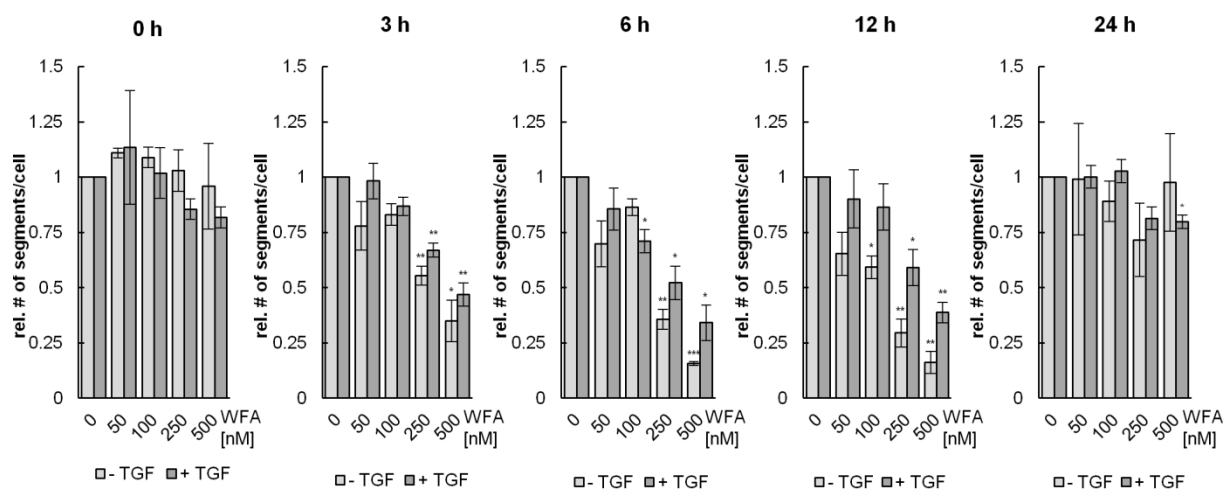
Figure 3.30: Withaferin A induces dose- and time-dependent decrease of vimentin. A549_VB6-CB cells were exposed to increasing concentrations of Withaferin A (WFA) in absence (- TGF) or presence of TGF-β (+ TGF) and subjected to time-lapse microscopy for 24 h. The effect of WFA-treatment on vimentin fiber segments was quantified in >100 cells after 0 h, 3 h, 6 h, 12 h and 24 h. Shown are relative numbers of segments per cell representing the means ± s.e.m. of three independent experiments. Statistical analysis of the dose-dependency was performed using student's t-test with reference to the untreated control (0 nM WFA), *P<0.05, **P<0.01, ***P<0.001.

While after 24 h WFA treatment, independently of the employed WFA concentration, no significant reduction of vimentin could be observed, after 3 h, 6 h and 12 h, vimentin fiber

segments were significantly decreased upon treatment with 250 nM and 500 nM WFA. This indicates that the effects of WFA were completely recovered after 24 h. Furthermore, the strongest decrease of vimentin fiber segments was observed after 6 h and 12 h, showing a two-fold reduction of vimentin in presence of TGF-β and a ten-fold reduction in absence of TGF-β. Overall, the results conclude that high-content imaging of the vimentin-chromobody model allows precise quantification of dose- and time-dependent compound effects independently of the initial level of vimentin.

To summarize, both actin-chromobody models A549_Actin-CB and Huh7_Actin-CB as well as the vimentin-chromobody model A549_VB6-CB can be applied for high-content imaging studies, thereby allowing a reliable segmentation of actin stress fibers or filamentous vimentin respectively. Induction of EMT by treatment with TGF-β could be quantified with all three chromobody models. Moreover, time- and dose-dependent effects of the vimentin-modulating small compound WFA were quantitatively detected by real-time high content imaging of the vimentin-chromobody model.

4 DISCUSSION

The cellular reprogramming process, epithelial-mesenchymal transition, is of particular interest for the development of anti-metastatic therapeutics. In this context, novel strategies that enable real-time analysis of EMT biomarkers are required that deepen our insight into the complex regulation of this dynamic process. In this thesis, nanobodies against the EMT marker proteins occludin, SNAI1 and vimentin were generated and analyzed regarding their applicability in biochemical as well as cell biological approaches. The occludin-specific nanobody OF6-NB is a powerful tool for biochemical applications particularly for pull-down experiments, yet is not appropriate to detect endogenous occludin in living cells. Functionality of the SNAI1-specific nanobody SG6-NB and chromobody SG6-CB are restricted to ectopically overexpressed Snail, while the recognition of endogenous Snail remains unclear. Two functional nanobodies, VB3-NB and VB6-NB, were developed and applied for biochemical detection and precipitation of vimentin, while their chromobody formats VB3-CB and VB6-CB are functional to trace endogenous vimentin in living cells. Based on the highly soluble and transient binding of VB6-CB and the previously described Actin-CB, EMT-relevant cellular models were generated and adapted for high-content imaging. These models allow live-visualization of actin and vimentin redistribution during EMT in real-time as well as quantitative detection of the effects of the EMT inducer TGF-β and the vimentin-modulating compound Withaferin A (WFA). In the following section the observed results are critically discussed in the context of the current state of the art in the field of nanobodies and EMT.

4.1 Nanobody selection process

To study spatial and temporal dynamics of cellular processes, such as EMT, a number of intracellular affinity reagents have been described that allow tracing of endogenous cellular target structures (see section 1.5). One advantage of these recombinant binding formats is that they can be easily selected form generic libraries. In this thesis specific nanobodies against the EMT-markers occludin, SNAI1 and vimentin have been selected via phage display. Phage display is the most robust and frequently used screening technique, nonetheless nanobodies can also be selected by mRNA display (Doshi et al., 2014), ribosome display (Yau et al., 2003), bacterial display (Fleetwood et al., 2013) or yeast display (Koide and Koide, 2012). Recently, a novel approach has been described that allows direct selection of nanobody sequences form the animal serum, without intermediary expression systems (Fridy et al., 2014). Most commonly, nanobody selection is based on libraries derived from immunized

animals (Lauwereys et al., 1998, Van Audenhove et al., 2013, Pardon et al., 2014), while in some cases naïve libraries from non-immunized animals have been applied (Monegal et al., 2009, Jobling et al., 2003).

Starting from a V_HH phage library, comprising $2x10^7$ cfu/ml, a clear enrichment of specific phages was obtained for each antigen after two panning cycles in this study. This is consistent with other studies, generally describing one or two panning cycles for selection of nanobodies from libraries derived from immunized animals, depending on the magnitude of the hcAb-mediated humoral response (Rothbauer et al., 2006, Pardon et al., 2014, Traenkle et al., 2015). Due to the larger diversity, at least two or more panning cycles are required for nanobody selection from naïve libraries (Groot et al., 2006, Jobling et al., 2003). For all antigens a satisfying number of specifically binding nanobodies were obtained after phage ELISA, hence, no more than 47 clones were tested per antigen. All selection technologies mentioned above are suited to identify high-affinity binding molecules, however, they are not able to predict functionality within living cells. Since a major focus of this work was to generate chromobodies for intracellular usage, the subsequent selection strategy of nanobodies, positive in phage ELISA, was implemented by simple intracellular co-localization studies as well as the fluorescent two-hybrid (F2H) assay. Other strategies to identify binding molecules within living cells have been described as well: The intracellular antibody capture technology (IACT) combines the phage display technology with a modified yeast two-hybrid (Y2H) assay, allowing the selection of binding molecules functional in yeast (Visintin et al., 1999, Visintin et al., 2002). An altered bacterial two-hybrid system was developed to enable a one-step isolation of nanobodies functional in bacteria (Pellis et al., 2012). Since antigens derived from *E. coli* comprise no posttranslational modifications and passive adsorption on solid surfaces sometimes leads to structural deterioration, another approach, describing a modified technique of the classic phage display using natively folded and freely accessible proteins produced in mammalian cells has been developed (Schmidthals, 2013). However, functional expression of all these selected binding molecules in mammalian cells is not ensured and still requires additional and careful intracellular validation.

4.2 Diversity of nanobody sequences

The variety of b lymphocytes producing specific antibodies is indispensable for the defense mechanisms of the adaptive humoral immune system. Thereby, the random combination of variable (V), diversity (D) and joining (J) genes (so called V(D)J recombination) is an underlying process during b cell maturation. For the formation of heavy chains of

conventional tetrameric antibodies as well as of heavy-chain-only antibodies, the alpaca genome comprises three V gene subgroups (IgHV1, IgHV2 and IgHV3), with IgHV3 containing 17 members of the V_HH set (divided into 6 subsets *A-F*) and 54 members of the V_H set (divided into 12 subsets *A-K*), seven D genes ($D_H1 - D_H7$) and seven J genes ($J_H1 - J_H7$) (Achour et al., 2008). In a first step, D and J segments are combined, while in a second step a V gene joins the assembled DJ sequence to form a complete V_HH or V_H exon (Nguyen et al., 1999). In heavy chain variable domains CDR1, FR2 and CDR2 are encoded by a V segment, while the CDR3 loop is formed by recombination of V, D, and J segments, resulting in increased sequence variability within this region (Wu et al., 1993).

Analysis of all the unique nanobody sequences selected in section 3.1 revealed significant differences. The two occludin-nanobodies are encoded by the same V gene of IgHV3 subgroup and V_HH subset *D* marked by the hydrophilic hallmark residues Phe37, Glu44, Asp45 and Gly47 in FR2 (Achour et al., 2008). The V gene of the SNAI1-nanobodies SA2-NB, SB4-NB, SF2-NB and SG1-NB belong to the V_HH subset *E* (Phe37, Glu44, Asp45, Leu47), while SF4-NB and SG6-NB are derived from the V_HH subset *B* (Tyr37, Glu44, Asp45, Leu47) of IgHV3 (Achour et al., 2008). As mentioned in the results section, the four vimentin-nanobodies VB3-NB, VE3-NB, VF6-NB and VG1-NB are V_HHs, including V genes derived from V_HH subset *A* (Tyr37, Gln44, Asp45, Leu47) of IgGV3, while the nanobodies VB6-NB, VC4-NB, VG4-NB and VH3-NB are encoded by V genes of the IgGV3 V_H set, including the hydrophobic residues Val37, Gly44, Leu45 and Trp47 in FR2 (Achour et al., 2008). During the generation of the phagemide library, precise preparation of DNA fragments, coding for heavy chains of hcAbs (IgG2, IgG3), should ensure that only V_HH domains are included in the library and selected by phage display and ELISA (Schmidthals, 2013). Thereby, three subsequent PCR reactions are performed to amplify the gene segments coding for the V_HH repertoire. The first PCR is specific for all heavy chains of conventional IgG1, IgG2, and IgG3, resulting in PCR products with different lengths, since the hcAbs lack the C_H1 domain. Only the shorter PCR product, derived from hcAbs serves as template for subsequent PCR amplifications specific for the variable domains. Hence, contamination with DNA fragments coding for heavy chains of conventional IgGs (IgG1s) during the second PCR amplification step is the likeliest explanation for the selected V_H sequences.

The varying length and high diversity within the CDR3 loops of the identified sequences is largely set by the integration of the D genes (Wu et al., 1993). An elongated CDR3 loop, often described for V_HH domains (Muyldermans, 2013), was only observed for the occludin-nanobodies, both comprising identical D genes with an additional cysteine residue (Figure

3.4). It can be assumed that this CDR3 loop is stabilized by the formation of a disulfide bridge mediated by the additional cysteine, which might be crucial for correct folding and recognition of the antigen. Hence, improper folding of OF6-CB in the reducing environment of the cytoplasm might be one reason, why this chromobody is only partially functional within living cells. All Snail nanobodies share the same D segment indicated by nearly identical CDR3s. By contrast, within V_HH sequences of the vimentin-nanobodies, CDR3 of VE3 is derived from another D segment than VB3, VF6 and VG1, and the V_H sequences each comprise largely diverse CDR3s indicating recombination of different D genes. Sequence analyses of CDR3 and FR4 regions revealed that all selected nanobodies contain the same J gene, J_H4, occurring most frequently in V_H as well as in V_HH sequences (Achour et al., 2008).

Beyond V(D)J recombination, other mechanisms such as somatic hypermutations (reviewed in French et al., 1989) and imprecise joining events, resulting in addition or loss of nucleotides at the junctions of recombined segments (reviewed in Schatz et al., 1992), increase the diversity of the selected nanobodies and explain varieties within sequences derived from the same V, D or J genes.

4.3 General applicability of the developed nanobodies and chromobodies

The main focus of this work was to generate a system that allows intracellular tracing of endogenous EMT-markers in living cells. Among the identified nanobodies and chromobodies only VB3-CB and VB6-CB are fully functional for intracellular applications, while occludin- and SNAI1-chromobodies are not suited to trace endogenous targets within living cells.

Occludin is an integral transmembranic component of cellular tight junctions between epithelial cells (Furuse et al., 1993). As mentioned above, the malfunction of the developed occludin-chromobodies might be explained by incorrect folding in the reducing environment of the cytoplasm. Another reason might be that within cells, the chromobody epitope is inaccessible. In intact tight junctions, occludin is known to interact with many other tight junctional proteins, including the three ZO proteins JAM, VAP-33, JEAP and CLMP (reviewed in Feldman et al., 2005). Thus, interaction of one of these proteins with the cytoplasmic C-terminal domain of occludin might mask the chromobody. When overexpressing occludin, some epitopes might be accessible, assuming that the ectopic occludin concentration is much higher than the concentration of endogenous interaction partners. This might explain that OF6-CB co-localizes with mCherry-OCLN, but not with

endogenous occludin (Figure 3.4). Surprisingly, intracellular-immunoprecipitation experiments indicated intracellular binding of OF6-CB to ectopically expressed as well as endogenous occludin (Figure 3.6). This might be explained by the disruption of tight junctional protein complexes leading to increased accessibility of the epitope upon cell lysis. Moreover, OF6-CB may bind to endogenous occludin within living cells, yet in a minor extent, so it is not detectable by fluorescence microscopy, but by IC-IP followed by immunoblotting, which is much more sensitive, due the enrichment of the antigen. OF6-NB was shown to efficiently precipitate and detect occludin in immunoprecipitation and Western blot experiments (Figure 3.5 and 3.6), leading to the assumption that OF6-NB recognizes a linear epitope rather than a conformational structure, as was shown for most nanobodies described so far (De Genst et al., 2006).

The high performance of the OF6-NB and OF6-CB in immunoprecipitation experiments as well as in IC-IP studies might facilitate the identification of novel binding partners of occludin. Additionally, several nanobodies have been recently applied as chaperones for the crystallization of complex biological structures, including integral transmembrane proteins (Conrath et al., 2009, Rasmussen et al., 2011, Pardon et al., 2014). Hence, OF6-NB might be useful to stabilize the overall structure of occludin alone or in complex with other proteins. This would expand the knowledge significantly, since only the structure of the cytoplasmic C-terminal domain of occludin has been elucidated to date (Li et al., 2005).

The canonical EMT marker and transcriptional repressor SNAI1 is of great interest for cancer research, particularly regarding its role in the development of metastases, acquisition of cancer stem cell-like properties and resistance to chemotherapeutic drugs (reviewed in Wang et al., 2013b and Kaufhold and Bonavida, 2014). Most studies addressing SNAI1 apply measurements on mRNA levels (Moreno-Bueno et al., 2009, Zhou et al., 2014), since SNAI1 protein levels are difficult to detect in Western blot or in immunocytochemical (IHC) and immunohistochemical (ICC) assays (Zhou et al., 2004, Lee et al., 2006, Qiao et al., 2010). This is explained by the high instability of the SNAI1 protein, combined with a lack of functionally reliable SNAI1 antibodies. In this context, it is not surprising that SG6-NB is barely functional for immunoprecipitation of SNAI1. The more promising format is the intracellular functional SG6-CB which recognizes ectopically expressed SNAI1 within living cells, as was shown by IC-IP (Figure 3.9) and by a modified fluorescent two-hybrid assay (Figure 3.10). Whether SG6-CB also binds to endogenous SNAI1, remains unclear, but it is a most attractive candidate for further investigations e.g. by analyzing IC-IP bound fractions by mass spectrometry.

DISCUSSION

Vimentin is the major intermediate filament protein found in mesenchymal cells and its role as cytoskeletal component has been known for many years (reviewed in Herrmann et al., 1996). Yet, we are still at the beginning to understand its dynamic and interdependent functions especially during EMT and metastasis formation. *In vitro* studies with the vimentin-specific nanobodies VB3-NB and VB6-NB coupled to an organic dye have shown that only VB6-NB detects denatured vimentin in Western blot and immunofluorescence. By generating a bivalent VB6-nanobody and thereby increasing its avidity, antigen detection was dramatically improved. Interestingly, VB3-NB precipitates vimentin more efficiently than VB6-NB, but in Western blot and immunofluorescence its epitope might be inaccessible. Based on these findings, VB6-NB is assumed to recognize a linear epitope, as it was also stated for OF6-NB, while VB3-NB might bind to a rather conformational epitope that is destroyed upon denaturation of vimentin. This hypothesis is supported by the fact that VB3-NB and VB6-NB are derived from different antibody classes (hcAb vs. conventional IgGs) and comprise completely differing hypervariable domains (Figure 4.1). Hence, it can be hypothesized that the two nanobodies address different epitopes, both located in the rod domain of vimentin. Yet, the precise epitope of each nanobody/chromobody is not known.

```
        CDR1           FR2          CDR2       CDR3
VB3   NTFSIKVMG  WYRQAPGKQRELVA  VSTNSGAS  YDGRYEDY
VB6   FTFSAASMR  WVRQVPGKGLEWVA  TIDGTGAN  FGRNY---
       ***    *  * **.*** * **  .   :**. :  .*
```
Figure 4.1: Sequence alignment of the three CDR regions (CDR1-3) and FR2 of VB3-NB and VB6-NB.

In recent years, novel super-resolution techniques have revolutionized the field of fluorescence microscopy (reviewed in Hell, 2009 and Fornasiero and Opazo, 2015). In this context fluorescently labeled nanobodies are used to allow a closer spatial proximity of the fluorophore and the target structure and thereby minimize the linkage errors observed with the much larger primary and secondary antibodies. In the past, a GFP-specific nanobody, covalently coupled to a fluorescent dye, has been applied for photoactivation localization microscopy (PALM) of fluorescently labeled microtubules (Ries et al., 2012). Recently, a tubulin-specific nanobody has been developed for super-resolution imaging of endogenous microtubules (Mikhaylova et al., 2015). Since VB6-NB was shown to detect vimentin directly in immunofluorescence, it may be a promising candidate to visualize endogenous vimentin by super-resolution microscopy, which is currently being investigated.

Another recent study describes a novel compound and 3-arylquinoline derivative, named Arylquin1, which triggers secretion of the tumor suppressor protein Par-4 leading to apoptosis

in diverse cancer cells, but not in normal cells (Burikhanov et al., 2014). Burikanov et al. revealed a potential mechanism, by which Par-4 is clustered upon binding to vimentin and thereby prevented from secretion. By binding to vimentin, Arylquin 1 displaces Par-4 from vimentin, resulting in Par-4 secretion. The proposed interaction between Par-4 and vimentin was supported by immunoprecipitation and intracellular co-localization experiments. In this context, VB6-CB might help for a better understanding of Arylquin 1's mode of action. Intracellular expression of VB6-CB might exhibit vimentin localization, depending on Arylquin 1 and Par-4. Moreover, IC-IP experiments could be applied to analyze the proposed interaction between vimentin and Par-4 in absence or presence of Arylquin 1 in a more physiological environment.

4.4 Chromobodies for live cell imaging

As described earlier in the introduction, chromobodies, comprising a nanobody moiety and a fluorescent protein, have become a valuable alternative to conventional antibodies and ectopic expression of fluorescently labeled target proteins. Several studies describe applications of chromobodies in living cells to visualize and trace dynamic changes of intracellular target structures (Rothbauer et al., 2006, Kirchhofer et al., 2010, Burgess et al., 2012, Li et al., 2012, Traenkle et al., 2015). In the context of this thesis, intrabodies addressing EMT marker proteins in living cells were of particular interest.

For live cell visualization of the well-known cytoskeletal component actin, which is known to undergo a dramatic reorganization during EMT, a number of chromobody-based and non-chromobody approaches have been described. The small peptide, lifeact, has been derived from the first 17 amino acids of Abp140 of *Saccharomyces cerevisiae* and successfully been applied as a live-cell actin marker in various cell lines as well as whole organisms e.g. *drosophila* and mice (Riedl et al., 2008, Riedl et al., 2010, Spracklen et al., 2014). Moreover, a number of intracellular functional F-actin specific nanobodies have been developed (Van Audenhove et al., 2013, Rocchetti et al., 2014).

The commercially available actin-chromobody, which has been applied in this study, is a valuable tool to trace the dynamic organization of F-actin *in cellulo* and *in vivo*, as it has recently been demonstrated in living zebrafish models (Panza et al., 2015). However, although reorganization of the actin cytoskeleton is linked to EMT it still occurs in numerous cellular processes and cannot only be classified as an EMT-specific phenomenon. To date, no approaches are available to visualize any other EMT specific marker in living cells.

DISCUSSION

In the present study, two chromobodies, VB3-CB and VB6-CB, were developed as novel biosensors to study the endogenous localization and dynamic rearrangements of the mesenchymal EMT-marker vimentin in live cells. The current state of the art regarding live-cell imaging of vimentin mainly relies on microinjection or ectopic expression of fluorescently labeled vimentin (Kuczmarski and Goldman, 2007, Helfand et al., 2011, Chang et al., 2009, Kajita et al., 2014). However, detailed analyses of protein expression, cell shape, motility and migration of several breast cancer cell lines upon ectopic expression or knock-down of vimentin have shown that increased vimentin expression correlates with a mesenchymal phenotype, while loss of vimentin expression causes mesenchymal cells to adopt epithelial phenotypes (Mendez et al., 2010). Hence, overexpression of fluorescently labeled vimentin does not reflect the endogenous situation.

The two chromobodies, developed in this study, visualize vimentin for the first time in its physiologically relevant state. Comparative analyses of fluorescently labeled vimentin (GFP-VIM) and the two chromobodies have shown that GFP-VIM strongly aggregates upon overexpression, while the chromobodies were more soluble. Both chromobodies were shown to have no effect on cell viability compared to solely expressed GFP. These findings are supported by the unaltered morphology and minimal changes in migration and invasion of A549 cells expressing VB6-CB (A549_VB6-CB), compared to the wild-type cell line. The more transient binding mode, observed by FRAP analysis suggests minimal interference with endogenous vimentin dynamics. Still, further impact on protein function cannot be completely excluded. As mentioned above, in a facilitated model vimentin disassembles upon extensive phosphorylation of Ser/Thr residues, while assembled filaments are widely unphosphorylated (Snider and Omary, 2014). Since alpaca immunization and nanobody selection were performed with recombinant vimentin purified from bacteria, it is likely that VB6-CB recognize both, soluble and polymerized vimentin independently of the phosphorylation state. Yet, intracellular binding of the chromobody might hinder posttranslational modifications of vimentin by masking the binding site of kinases or interaction with other binding partners, as it has been proposed for some intrabodies (Sato et al., 2013a, Bethuyne et al., 2014). In this context, recognition of the rod domain may be advantageous and less harmful than binding of the chromobody to the N- or C-terminus, since important phosphorylation sites are located mainly in the head- and tail domain of vimentin.

4.5 Induction of EMT

EMT can be induced by numerous intrinsic (e.g. receptors, transcription factors) and extrinsic stimuli, such as growth factors and components of the ECM (reviewed by (Gonzalez and Medici, 2014)). In this context, the transforming growth factor β1 (TGF-β1) is the most widely used inducer, regarding EMT in cancer research. During early stages of tumorigenesis, TGF-β inhibits cell proliferation and acts as a tumor suppressor, while in later stages it promotes tumor progression by the initiation of EMT leading to increased invasiveness and formation of metastases (Heldin et al., 2009). In this study, induction of EMT with TGF-β led to characteristic changes in morphology and motility of both wild-type A549 and A549_VB6-CB. Surprisingly, no significant changes in wound healing were induced by TGF-β in both cell lines. This might be explained by the proliferation inhibiting effect of TGF-β, which cannot be differentiated from cell migration by classic scratch assays. Moreover, previous studies have shown that A549 cells with cancer stem cell (CSC)-like properties respond to TGF-β with enhanced motility in wound healing assays, while the non-CSC cells did not change in motility (Tirino et al., 2013). Whether the monoclonal A549_VB6-CB cell line exhibits a CSC or non-CSC-like phenotype remains unclear and has to be further investigated.

In A549_VB6-CB cells increased vimentin protein levels were detected by Western blot upon induction of EMT with TGF-β. This is due to regulation of vimentin protein expression by SMAD-dependent TGF-β signaling. Activated TGF-β receptors phosphorylate SMAD2/3, which complex with SMAD4 and translocate in the nucleus. Once in the nucleus, the SMAD complex activates the expression of EMT transcription factors, including FOXC2, which was shown to promote vimentin expression (Mani et al., 2007, Lamouille et al., 2014). Moreover, the SMAD complex activates transcription through interaction with DNA-binding factors of the Sp1 or AP-1 family such as c-Jun, c-Fos and Sp1/SP3 that bind to the vimentin promoter and initiate vimentin expression (Rittling et al., 1989, Wu et al., 2007, Wu et al., 2003). SMAD3 was also shown to directly activate the expression of vimentin (Wu et al., 2007). Moreover, the vimentin promoter is a target of β-catenin/TCF4 complex and of NFκB, both components of SMAD-independent pathways, that can be activated by TGF-β (see section 1.3.2) (Gilles et al., 2003, Lilienbaum and Paulin, 1993, Wu et al., 2007).

Live-cell imaging of TGF-β treated A549_VB6-CB cells showed a reverse redistribution from perinuclear vimentin in untreated cells, extending to a complex network throughout the cell periphery. This is consistent with a recent study, focusing on TGF-β-mediated EMT in different populations of A549 cells with features of cancer stem cells (CSC) or non-CSC

properties (Tirino et al., 2013). Vimentin redistribution upon TGF-β treatment was detected in both CSCs and non-CSCs. Likewise, EMT-dependent vimentin reorganization in A549 cells has been observed by overexpression of the transcription factor PREP1, which is described to affect TGF-β-SMAD signaling (Risolino et al., 2014). Regarding vimentin's role in cell motility and migration, Helfand et al. have shown that within migrating mesenchymal-like fibroblasts, gradients of different vimentin assembly states are present within the cells. While in the tail and perinuclear regions of these cells vimentin was organized in a complex network of filaments, in lamellipodia a disassembled fraction of vimentin was observed (Helfand et al., 2011). Consequently, the reliable visualization of TGF-β mediated reorganization of the highly relevant EMT biomarker vimentin makes VB6-CB a valuable tool for researchers in the field of vimentin and EMT.

Interestingly, TGF-β-mediated induction of vimentin lead to a slight increase of the chromobody fluorescence in A549_VB6-CB cells, which cannot be simply explained, since chromobody expression is not expected to be dependent on TGF-β. Recently, similar results were observed for a chromobody specific for β-catenin, showing a significant increase in the global chromobody signal after inhibition of the β-catenin destruction complex, while chromobody mRNA levels remained unaffected (Traenkle et al., 2015). In this study, a mechanism leading to an antigen-mediated stabilization of the chromobody has been proposed. Other studies have described the stabilization of intrabodies, modified by the addition of a degradation promoting domain, upon ectopic expression of the respective antigens (Sibler et al., 2005). Similar to the mentioned β-catenin specific chromobody, VB6-CB might be stabilized by the presence of its antigen independently of an introduced destabilizing domain, suggesting a general principle for antigen-dependent stabilization of intracellularly expressed chromobodies. Further investigations will be necessary to clarify, whether this may constitute a novel and flexible approach to detect dynamic changes in the expression levels of endogenous proteins by means of chromobodies.

With regard to actin cytoskeletal arrangements, TGF-β-mediated EMT induction led to the reorganization of cortical actin bundles to thick stress fibers at the ventral cell surface in both developed Actin-CB models: A549_Actin-CB and Huh7_Actin-CB (Figure 3.26). These observations are consistent with previous studies describing EMT-related actin rearrangements e.g. in hepatocytes (Godoy et al., 2009) or mouse mammary epithelial NMuMG cells (Haynes et al., 2011). TGF-β-dependent remodeling of actin has been shown to be dependent on RhoA activation (Masszi et al., 2003). Moreover, increased expression of moesin, a member of the ezrin/radixin/moesin (ERM) family has been reported in response to

TGF-β and is proposed to be required for efficient actin filament remodeling (Haynes et al., 2011).

4.6 Relevance of EMT chromobody models for therapeutic research and clinical settings

EMT plays a prominent role in the development of cancer metastases and in the acquisition of therapy resistance of many cancers. Common therapeutics have often been ineffective regarding metastatic cancer, hence, novel technologies to identify compounds targeting the dynamic transition process and its related marker proteins are of particular interest for the anti-metastatic cancer therapy. Screening strategies addressing EMT currently rely on endpoint readouts of gene expression, fluorescence intensity, glow luminescence, and high-content imaging. For example, Li et al. developed a high-throughput screening approach based on a luciferase reporter system measuring vimentin expression and analyzed the effect of the primary hits on the invasive potential of spheroids (Li et al., 2011). Another study, conducted by Gupta et al. screened for compounds affecting cell viability of epithelial CSCs by a luminescence assay (Gupta et al., 2009). Recently, Chua et al. have designed a high-content screening assay to identify EMT inhibitors affecting cell growth and cell migration (Chua et al., 2012).

In this thesis, cell-based chromobody models were generated for the first time to visualize dynamic changes of the EMT-markers actin and vimentin in real time. Moreover, high-content imaging models were developed to allow monitoring and quantifying subtle changes in expression and dynamic redistribution of actin and vimentin upon pathway activation. Finally, the vimentin-chromobody model was applied to determine time- and dose-dependent alterations of vimentin upon compound treatment with Withaferin A (WFA). This proof of principle study demonstrates that the approach developed in this thesis, to trace endogenous EMT-markers, provides much deeper insight into the cellular properties and effects of EMT modulating compounds. The observation of early effects 3 h after WFA incubation with doses of 250 nM and higher indicates a substantial cellular uptake of WFA and its functionality in the cellular environment. Continuous live-cell imaging revealed a maximum effect after 6 h – 12 h and a complete reversion after 24 h, which indicates that WFA might be actively exported, inactivated upon metabolization or counteracted by cellular vimentin-regulatory circuits. In any case, such transient compound effects cannot be identified by any endpoint assay. This example clearly illustrates that compound screens which are restricted to certain time points are prone to report false negatives. The approach developed in this thesis is

DISCUSSION

suitable to overcome these limitations and is expected to increase the yield of screening campaigns, thereby facilitating the identification of effective EMT modulators.

In the context of EMT, preclinical drug discovery still relies mainly on 2D cell culture studies, for reasons of simplicity and low costs. However, critics argue that 2D models do not reflect the complexity of cancerous tissue *in vivo*, including the contribution of the ECM into which cells undergoing EMT invade. To simulate the *in vivo* situation, novel 3D approaches have been recently reported (Li et al., 2011, Chua et al., 2012, Katz et al., 2011, Aref et al., 2013). Katz et al. have established a 3D breast cancer *in vitro* model that mimics the invasion of cells with mesenchymal phenotype to break through the basal membrane into stromal collagen (Katz et al., 2011). In another approach Aref et al. have developed a microfluidic system that integrates A549 lung tumor cell spheroids in a 3D hydrogel scaffold and in co-culture with endothelial HUVEC cells (Aref et al., 2013). The authors describe significant differences in drug response between 2D and 3D models and between monoculture and co-culture, regarding cell proliferation and migration away from the spheroid. Acknowledging the current debate, the next step will be to transfer the described EMT chromobody models A549_VB6-CB, A549_Actin-CB and Huh7_Actin-CB to robust 3D models, allowing a most authentic identification of EMT targeting compounds. Notably, observations described for primary hepatic 2D and 3D cultures regarding drug toxicity tests led to similar conclusions. For example, toxic effects of acetaminophen *in vivo* can be reproduced in 3D, but not in 2D models (Schyschka et al., 2013). Moreover, expression levels and distribution of actin and vimentin significantly differ between 2D and 3D cultured hepatocytes (Godoy et al., 2009). Since, both Actin-CB and VB6-CB, can be functionally expressed in primary hepatocytes as shown in this study, chromobody tracking of endogenous actin and vimentin in primary hepatocytes might lead to a better understanding of toxicological effects of drugs in such 3D models.

When it comes to downstream preclinical screening of potential drug candidates, animal studies are indispensable. Since most studies on EMT are based on *in vitro* and *in cellulo* assays, the validity of these data for the *in vivo* situation has been under intense debate (Tarin et al., 2005, Cardiff, 2005). This is partly due to the difficulty to distinguish the origin of fibroblasts and CTCs, thereby differentiating between EMT-derived cells and cells with other origins. Moreover inhibiting EMT *in vivo,* has been proposed to be possibly counterproductive to prevent distant metastases in patients already exhibiting CTCs (Tsai et al., 2012, Nieto, 2013). However, novel studies demonstrated that data derived from *in vitro* EMT studies can be translated into the clinical setting (Jahn et al., 2012, Tsai et al., 2012,

Bonnomet et al., 2012). Most interestingly, the breast cancer EMT *in vivo* model of Bonnomet et al. is based on MDA-MB-468 vimentin-negative cells that grow into primary heterogeneous xenografts with vimentin-negative as well as vimentin-positive regions. Furthermore, circulating tumor cells exhibited EMT markers suggesting that spontaneous EMT events promote intravasation and metastatic dissemination *in vivo*. Based on these data and on the fact that chromobodies and other intrabodies have been successfully introduced in living animals (e.g. zebrafish, mice) (Panza et al., 2015, Sato et al., 2013b), it can be proposed that intracellular tracing of the reliable EMT biomarker vimentin with VB6-CB might facilitate live-experiments and histological studies regarding EMT, CTCs, metastatic dissemination and potential drug candidates *in vivo*.

4.7 Outlook

In this thesis, novel nanobodies and chromobodies against the EMT-biomarkers occludin, SNAI1 and vimentin have been developed. OF6-NB specifically targets occludin in Western blot and pull down experiments. Since OF6-CB is not functional for intracellular imaging, a chromobody against an alternative membrane associated EMT-marker protein would be highly valuable. In this context, the tight junction component ZO1 might be a suitable target, since this large protein localizes at the cytosolic surface of the plasma membrane and might be more accessible for chromobody binding. Currently, potential ZO1 specific chromobodies are under development.

The role of SNAI1 in tumor progression and metastasis formation is of particular interest for cancer researchers as described in numerous recent studies (Zhou et al., 2014, Wang et al., 2014, Kaufhold and Bonavida, 2014). However, as shown in this study, available SNAI1 antibodies are poorly functional. Hence, further efforts to generate SNAI1 specific nano- or chromobodies are highly reasonable. Based on the findings described in this thesis, further experiments to analyze whether SG6-CB indeed binds endogenous SNAI1 e.g. by mass spectrometry would be indicated. Moreover, the development of bivalent SNAI1-nanobodies to obtain binding molecules with increased avidity might lead to better results.

The two identified vimentin binders VB3 and VB6 are functional as nanobodies as well as chromobodies. With regard to the emerging technologies for super resolution microscopy the bivalent VB6-VB6-NB is an interesting tool for super resolution recordings of endogenous vimentin. In this context, experimental settings have to be optimized including the fixation processes, selection of appropriate dyes and dye-coupling.

Most importantly, chromobody-based models developed in this study combine the relevance of actin and particularly vimentin as EMT biomarkers with the unique advantage of live-cell analysis and can be used to monitor time- and dose-dependencies of compound-mediated effects. Based on these proof-of-principle studies, the next step will be to apply the A549-VB6-CB system to compound screening. Since vimentin is regulated by extensive phosphorylation, it would be highly interesting to test e.g. libraries comprising kinase inhibitors.

Finally, the developed 2D models may be adapted to 3D cell systems, using current techniques such as 3D-KITChip or the hanging drop system. Although it will be very challenging to develop a reliable 3D phenotypic readout, such models will provide deeper insights in the complex regulation of EMT in physiologically more relevant systems.

5 REFERENCES

ABSKHARON, R. N., GIACHIN, G., WOHLKONIG, A., SOROR, S. H., PARDON, E., LEGNAME, G. & STEYAERT, J. 2014. Probing the N-terminal beta-sheet conversion in the crystal structure of the human prion protein bound to a nanobody. *J Am Chem Soc,* 136**,** 937-44.

ACHOUR, I., CAVELIER, P., TICHIT, M., BOUCHIER, C., LAFAYE, P. & ROUGEON, F. 2008. Tetrameric and homodimeric camelid IgGs originate from the same IgH locus. *J Immunol,* 181**,** 2001-9.

ACLOQUE, H., ADAMS, M. S., FISHWICK, K., BRONNER-FRASER, M. & NIETO, M. A. 2009. Epithelial-mesenchymal transitions: the importance of changing cell state in development and disease. *J Clin Invest,* 119**,** 1438-49.

ANDO-AKATSUKA, Y., SAITOU, M., HIRASE, T., KISHI, M., SAKAKIBARA, A., ITOH, M., YONEMURA, S., FURUSE, M. & TSUKITA, S. 1996. Interspecies diversity of the occludin sequence: cDNA cloning of human, mouse, dog, and rat-kangaroo homologues. *J Cell Biol,* 133**,** 43-7.

ARBABI GHAHROUDI, M., DESMYTER, A., WYNS, L., HAMERS, R. & MUYLDERMANS, S. 1997. Selection and identification of single domain antibody fragments from camel heavy-chain antibodies. *FEBS Lett,* 414**,** 521-6.

AREF, A. R., HUANG, R. Y., YU, W., CHUA, K. N., SUN, W., TU, T. Y., BAI, J., SIM, W. J., ZERVANTONAKIS, I. K., THIERY, J. P. & KAMM, R. D. 2013. Screening therapeutic EMT blocking agents in a three-dimensional microenvironment. *Integr Biol (Camb),* 5**,** 381-9.

ARNOUX, V., NASSOUR, M., L'HELGOUALC'H, A., HIPSKIND, R. A. & SAVAGNER, P. 2008. Erk5 controls Slug expression and keratinocyte activation during wound healing. *Mol Biol Cell,* 19**,** 4738-49.

BAMFORTH, S. D., KNIESEL, U., WOLBURG, H., ENGELHARDT, B. & RISAU, W. 1999. A dominant mutant of occludin disrupts tight junction structure and function. *J Cell Sci,* 112 (Pt 12)**,** 1879-88.

BARGAGNA-MOHAN, P., HAMZA, A., KIM, Y. E., KHUAN ABBY HO, Y., MOR-VAKNIN, N., WENDSCHLAG, N., LIU, J., EVANS, R. M., MARKOVITZ, D. M., ZHAN, C. G., KIM, K. B. & MOHAN, R. 2007. The tumor inhibitor and antiangiogenic agent withaferin A targets the intermediate filament protein vimentin. *Chem Biol,* 14**,** 623-34.

BARRIERE, G., FICI, P., GALLERANI, G., FABBRI, F. & RIGAUD, M. 2015. Epithelial-mesenchymal transition: a double-edged sword. *Clin Transl Med,* 4**,** 14.

BARTHELEMY, P. A., RAAB, H., APPLETON, B. A., BOND, C. J., WU, P., WIESMANN, C. & SIDHU, S. S. 2008. Comprehensive analysis of the factors contributing to the stability and solubility of autonomous human VH domains. *J Biol Chem,* 283**,** 3639-54.

BAZZONI, G., MARTINEZ-ESTRADA, O. M., ORSENIGO, F., CORDENONSI, M., CITI, S. & DEJANA, E. 2000. Interaction of junctional adhesion molecule with the tight junction components ZO-1, cingulin, and occludin. *J Biol Chem,* 275**,** 20520-6.

BEEMAN, N., WEBB, P. G. & BAUMGARTNER, H. K. 2012. Occludin is required for apoptosis when claudin-claudin interactions are disrupted. *Cell Death Dis,* 3**,** e273.

BETHUYNE, J., DE GIETER, S., ZWAENEPOEL, O., GARCIA-PINO, A., DURINCK, K., VERHELLE, A., HASSANZADEH-GHASSABEH, G., SPELEMAN, F., LORIS, R. & GETTEMANS, J. 2014. A nanobody modulates the p53 transcriptional program without perturbing its functional architecture. *Nucleic Acids Res,* 42**,** 12928-38.

BIOCCA, S., NEUBERGER, M. S. & CATTANEO, A. 1990. Expression and targeting of intracellular antibodies in mammalian cells. *EMBO J,* 9**,** 101-8.

REFERENCES

BIRD, R. E., HARDMAN, K. D., JACOBSON, J. W., JOHNSON, S., KAUFMAN, B. M., LEE, S. M., LEE, T., POPE, S. H., RIORDAN, G. S. & WHITLOW, M. 1988. Single-chain antigen-binding proteins. *Science,* 242**,** 423-6.

BONNOMET, A., SYNE, L., BRYSSE, A., FEYEREISEN, E., THOMPSON, E. W., NOEL, A., FOIDART, J. M., BIREMBAUT, P., POLETTE, M. & GILLES, C. 2012. A dynamic in vivo model of epithelial-to-mesenchymal transitions in circulating tumor cells and metastases of breast cancer. *Oncogene,* 31**,** 3741-53.

BRABLETZ, T., JUNG, A., REU, S., PORZNER, M., HLUBEK, F., KUNZ-SCHUGHART, L. A., KNUECHEL, R. & KIRCHNER, T. 2001. Variable beta-catenin expression in colorectal cancers indicates tumor progression driven by the tumor environment. *Proc Natl Acad Sci U S A,* 98**,** 10356-61.

BURGESS, A., LORCA, T. & CASTRO, A. 2012. Quantitative live imaging of endogenous DNA replication in mammalian cells. *PLoS One,* 7**,** e45726.

BURIKHANOV, R., SVIRIPA, V. M., HEBBAR, N., ZHANG, W., LAYTON, W. J., HAMZA, A., ZHAN, C. G., WATT, D. S., LIU, C. & RANGNEKAR, V. M. 2014. Arylquins target vimentin to trigger Par-4 secretion for tumor cell apoptosis. *Nat Chem Biol,* 10**,** 924-6.

BYUN, Y., CHEN, F., CHANG, R., TRIVEDI, M., GREEN, K. J. & CRYNS, V. L. 2001. Caspase cleavage of vimentin disrupts intermediate filaments and promotes apoptosis. *Cell Death Differ,* 8**,** 443-50.

CARDIFF, R. D. 2005. Epithelial to Mesenchymal Transition Tumors: Fallacious or Snail's Pace? *Clin Cancer Res,* 11**,** 8534-7.

CASSIMERIS, L., GUGLIELMI, L., DENIS, V., LARROQUE, C. & MARTINEAU, P. 2013. Specific in vivo labeling of tyrosinated alpha-tubulin and measurement of microtubule dynamics using a GFP tagged, cytoplasmically expressed recombinant antibody. *PLoS One,* 8**,** e59812.

CATTANEO, A. & BIOCCA, S. 1999. The selection of intracellular antibodies. *Trends Biotechnol,* 17**,** 115-21.

CAUSSINUS, E., KANCA, O. & AFFOLTER, M. 2012. Fluorescent fusion protein knockout mediated by anti-GFP nanobody. *Nat Struct Mol Biol,* 19**,** 117-21.

CHALFIE, M., TU, Y., EUSKIRCHEN, G., WARD, W. W. & PRASHER, D. C. 1994. Green fluorescent protein as a marker for gene expression. *Science,* 263**,** 802-5.

CHANG, C. C., HSU, W. H., WANG, C. C., CHOU, C. H., KUO, M. Y., LIN, B. R., CHEN, S. T., TAI, S. K., KUO, M. L. & YANG, M. H. 2013. Connective tissue growth factor activates pluripotency genes and mesenchymal-epithelial transition in head and neck cancer cells. *Cancer Res,* 73**,** 4147-57.

CHANG, L., BARLAN, K., CHOU, Y. H., GRIN, B., LAKONISHOK, M., SERPINSKAYA, A. S., SHUMAKER, D. K., HERRMANN, H., GELFAND, V. I. & GOLDMAN, R. D. 2009. The dynamic properties of intermediate filaments during organelle transport. *J Cell Sci,* 122**,** 2914-23.

CHEN, Y., MERZDORF, C., PAUL, D. L. & GOODENOUGH, D. A. 1997. COOH terminus of occludin is required for tight junction barrier function in early Xenopus embryos. *J Cell Biol,* 138**,** 891-9.

CHERNYATINA, A. A., NICOLET, S., AEBI, U., HERRMANN, H. & STRELKOV, S. V. 2012. Atomic structure of the vimentin central alpha-helical domain and its implications for intermediate filament assembly. *Proc Natl Acad Sci U S A,* 109**,** 13620-5.

CHUA, K. N., SIM, W. J., RACINE, V., LEE, S. Y., GOH, B. C. & THIERY, J. P. 2012. A cell-based small molecule screening method for identifying inhibitors of epithelial-mesenchymal transition in carcinoma. *PLoS One,* 7**,** e33183.

COGLI, L., PROGIDA, C., BRAMATO, R. & BUCCI, C. 2013. Vimentin phosphorylation and assembly are regulated by the small GTPase Rab7a. *Biochim Biophys Acta,* 1833**,** 1283-93.

COLBY, D. W., GARG, P., HOLDEN, T., CHAO, G., WEBSTER, J. M., MESSER, A., INGRAM, V. M. & WITTRUP, K. D. 2004. Development of a human light chain variable domain (V(L)) intracellular antibody specific for the amino terminus of huntingtin via yeast surface display. *J Mol Biol,* 342**,** 901-12.

COMLEY, J. 2014. The current status of non-biopharma drug discovery. *Drug Discovery World,* Spring 2014.

CONRATH, K., PEREIRA, A. S., MARTINS, C. E., TIMOTEO, C. G., TAVARES, P., SPINELLI, S., KINNE, J., FLAUDROPS, C., CAMBILLAU, C., MUYLDERMANS, S., MOURA, I., MOURA, J. J., TEGONI, M. & DESMYTER, A. 2009. Camelid nanobodies raised against an integral membrane enzyme, nitric oxide reductase. *Protein Sci,* 18**,** 619-28.

CONRATH, K., VINCKE, C., STIJLEMANS, B., SCHYMKOWITZ, J., DECANNIERE, K., WYNS, L., MUYLDERMANS, S. & LORIS, R. 2005. Antigen binding and solubility effects upon the veneering of a camel VHH in framework-2 to mimic a VH. *J Mol Biol,* 350**,** 112-25.

CONRATH, K. E., LAUWEREYS, M., GALLENI, M., MATAGNE, A., FRERE, J. M., KINNE, J., WYNS, L. & MUYLDERMANS, S. 2001. Beta-lactamase inhibitors derived from single-domain antibody fragments elicited in the camelidae. *Antimicrob Agents Chemother,* 45**,** 2807-12.

CONRATH, K. E., WERNERY, U., MUYLDERMANS, S. & NGUYEN, V. K. 2003. Emergence and evolution of functional heavy-chain antibodies in Camelidae. *Dev Comp Immunol,* 27**,** 87-103.

CUMMINS, P. M. 2012. Occludin: one protein, many forms. *Mol Cell Biol,* 32**,** 242-50.

DAUPHIN, M., BARBE, C., LEMAIRE, S., NAWROCKI-RABY, B., LAGONOTTE, E., DELEPINE, G., BIREMBAUT, P., GILLES, C. & POLETTE, M. 2013. Vimentin expression predicts the occurrence of metastases in non small cell lung carcinomas. *Lung Cancer,* 81**,** 117-22.

DAVIES, D. R. & METZGER, H. 1983. Structural basis of antibody function. *Annu Rev Immunol,* 1**,** 87-117.

DAVIS, F. M., STEWART, T. A., THOMPSON, E. W. & MONTEITH, G. R. 2014. Targeting EMT in cancer: opportunities for pharmacological intervention. *Trends Pharmacol Sci,* 35**,** 479-88.

DE CRAENE, B. & BERX, G. 2013. Regulatory networks defining EMT during cancer initiation and progression. *Nat Rev Cancer,* 13**,** 97-110.

DE GENST, E., SILENCE, K., DECANNIERE, K., CONRATH, K., LORIS, R., KINNE, J., MUYLDERMANS, S. & WYNS, L. 2006. Molecular basis for the preferential cleft recognition by dromedary heavy-chain antibodies. *Proc Natl Acad Sci U S A,* 103**,** 4586-91.

DE MEYER, T., MUYLDERMANS, S. & DEPICKER, A. 2014. Nanobody-based products as research and diagnostic tools. *Trends Biotechnol,* 32**,** 263-70.

DESMYTER, A., TRANSUE, T. R., GHAHROUDI, M. A., THI, M. H., POORTMANS, F., HAMERS, R., MUYLDERMANS, S. & WYNS, L. 1996. Crystal structure of a camel single-domain VH antibody fragment in complex with lysozyme. *Nat Struct Biol,* 3**,** 803-11.

DOMINGUEZ, R. & HOLMES, K. C. 2011. Actin structure and function. *Annu Rev Biophys,* 40**,** 169-86.

DOSHI, R., CHEN, B. R., VIBAT, C. R., HUANG, N., LEE, C. W. & CHANG, G. 2014. In vitro nanobody discovery for integral membrane protein targets. *Sci Rep,* 4**,** 6760.

DU, D., XU, F., YU, L., ZHANG, C., LU, X., YUAN, H., HUANG, Q., ZHANG, F., BAO, H., JIA, L., WU, X., ZHU, X., ZHANG, X., ZHANG, Z. & CHEN, Z. 2010. The tight junction protein, occludin, regulates the directional migration of epithelial cells. *Dev Cell,* 18**,** 52-63.

REFERENCES

DUPIN, E., CALLONI, G., REAL, C., GONCALVES-TRENTIN, A. & LE DOUARIN, N. M. 2007. Neural crest progenitors and stem cells. *C R Biol,* 330**,** 521-9.

EGGENSTEIN, E., EICHINGER, A., KIM, H. J. & SKERRA, A. 2014. Structure-guided engineering of Anticalins with improved binding behavior and biochemical characteristics for application in radio-immuno imaging and/or therapy. *J Struct Biol,* 185**,** 203-14.

FANNING, A. S., JAMESON, B. J., JESAITIS, L. A. & ANDERSON, J. M. 1998. The tight junction protein ZO-1 establishes a link between the transmembrane protein occludin and the actin cytoskeleton. *J Biol Chem,* 273**,** 29745-53.

FELDMAN, G. J., MULLIN, J. M. & RYAN, M. P. 2005. Occludin: structure, function and regulation. *Adv Drug Deliv Rev,* 57**,** 883-917.

FENG, X. H. & DERYNCK, R. 2005. Specificity and versatility in tgf-beta signaling through Smads. *Annu Rev Cell Dev Biol,* 21**,** 659-93.

FLEETWOOD, F., DEVOOGDT, N., PELLIS, M., WERNERY, U., MUYLDERMANS, S., STAHL, S. & LOFBLOM, J. 2013. Surface display of a single-domain antibody library on Gram-positive bacteria. *Cell Mol Life Sci,* 70**,** 1081-93.

FODDE, R. & BRABLETZ, T. 2007. Wnt/beta-catenin signaling in cancer stemness and malignant behavior. *Curr Opin Cell Biol,* 19**,** 150-8.

FORNASIERO, E. F. & OPAZO, F. 2015. Super-resolution imaging for cell biologists: concepts, applications, current challenges and developments. *Bioessays,* 37**,** 436-51.

FRENCH, D. L., LASKOV, R. & SCHARFF, M. D. 1989. The role of somatic hypermutation in the generation of antibody diversity. *Science,* 244**,** 1152-7.

FRIDY, P. C., LI, Y., KEEGAN, S., THOMPSON, M. K., NUDELMAN, I., SCHEID, J. F., OEFFINGER, M., NUSSENZWEIG, M. C., FENYO, D., CHAIT, B. T. & ROUT, M. P. 2014. A robust pipeline for rapid production of versatile nanobody repertoires. *Nat Methods,* 11**,** 1253-60.

FURUSE, M., HIRASE, T., ITOH, M., NAGAFUCHI, A., YONEMURA, S., TSUKITA, S. & TSUKITA, S. 1993. Occludin: a novel integral membrane protein localizing at tight junctions. *J Cell Biol,* 123**,** 1777-88.

GEBACK, T., SCHULZ, M. M., KOUMOUTSAKOS, P. & DETMAR, M. 2009. TScratch: a novel and simple software tool for automated analysis of monolayer wound healing assays. *Biotechniques,* 46**,** 265-74.

GILLES, C., POLETTE, M., MESTDAGT, M., NAWROCKI-RABY, B., RUGGERI, P., BIREMBAUT, P. & FOIDART, J. M. 2003. Transactivation of vimentin by beta-catenin in human breast cancer cells. *Cancer Res,* 63**,** 2658-64.

GODOY, P., HENGSTLER, J. G., ILKAVETS, I., MEYER, C., BACHMANN, A., MULLER, A., TUSCHL, G., MUELLER, S. O. & DOOLEY, S. 2009. Extracellular matrix modulates sensitivity of hepatocytes to fibroblastoid dedifferentiation and transforming growth factor beta-induced apoptosis. *Hepatology,* 49**,** 2031-43.

GODOY, P., HEWITT, N. J., ALBRECHT, U., ANDERSEN, M. E., ANSARI, N., BHATTACHARYA, S., BODE, J. G., BOLLEYN, J., BORNER, C., BOTTGER, J., BRAEUNING, A., BUDINSKY, R. A., BURKHARDT, B., CAMERON, N. R., CAMUSSI, G., CHO, C. S., CHOI, Y. J., CRAIG ROWLANDS, J., DAHMEN, U., DAMM, G., DIRSCH, O., DONATO, M. T., DONG, J., DOOLEY, S., DRASDO, D., EAKINS, R., FERREIRA, K. S., FONSATO, V., FRACZEK, J., GEBHARDT, R., GIBSON, A., GLANEMANN, M., GOLDRING, C. E., GOMEZ-LECHON, M. J., GROOTHUIS, G. M., GUSTAVSSON, L., GUYOT, C., HALLIFAX, D., HAMMAD, S., HAYWARD, A., HAUSSINGER, D., HELLERBRAND, C., HEWITT, P., HOEHME, S., HOLZHUTTER, H. G., HOUSTON, J. B., HRACH, J., ITO, K., JAESCHKE, H., KEITEL, V., KELM, J. M., KEVIN PARK, B., KORDES, C., KULLAK-UBLICK, G. A., LECLUYSE, E. L., LU, P.,

LUEBKE-WHEELER, J., LUTZ, A., MALTMAN, D. J., MATZ-SOJA, M., MCMULLEN, P., MERFORT, I., MESSNER, S., MEYER, C., MWINYI, J., NAISBITT, D. J., NUSSLER, A. K., OLINGA, P., PAMPALONI, F., PI, J., PLUTA, L., PRZYBORSKI, S. A., RAMACHANDRAN, A., ROGIERS, V., ROWE, C., SCHELCHER, C., SCHMICH, K., SCHWARZ, M., SINGH, B., STELZER, E. H., STIEGER, B., STOBER, R., SUGIYAMA, Y., TETTA, C., THASLER, W. E., VANHAECKE, T., VINKEN, M., WEISS, T. S., WIDERA, A., WOODS, C. G., XU, J. J., YARBOROUGH, K. M. & HENGSTLER, J. G. 2013. Recent advances in 2D and 3D in vitro systems using primary hepatocytes, alternative hepatocyte sources and non-parenchymal liver cells and their use in investigating mechanisms of hepatotoxicity, cell signaling and ADME. *Arch Toxicol,* 87**,** 1315-530.

GONZALEZ, D. M. & MEDICI, D. 2014. Signaling mechanisms of the epithelial-mesenchymal transition. *Sci Signal,* 7**,** re8.

GREENBERG, A. S., AVILA, D., HUGHES, M., HUGHES, A., MCKINNEY, E. C. & FLAJNIK, M. F. 1995. A new antigen receptor gene family that undergoes rearrangement and extensive somatic diversification in sharks. *Nature,* 374**,** 168-73.

GROOT, A. J., VERHEESEN, P., WESTERLAKEN, E. J., GORT, E. H., VAN DER GROEP, P., BOVENSCHEN, N., VAN DER WALL, E., VAN DIEST, P. J. & SHVARTS, A. 2006. Identification by phage display of single-domain antibody fragments specific for the ODD domain in hypoxia-inducible factor 1alpha. *Lab Invest,* 86**,** 345-56.

GROSS, G. G., JUNGE, J. A., MORA, R. J., KWON, H. B., OLSON, C. A., TAKAHASHI, T. T., LIMAN, E. R., ELLIS-DAVIES, G. C., MCGEE, A. W., SABATINI, B. L., ROBERTS, R. W. & ARNOLD, D. B. 2013. Recombinant probes for visualizing endogenous synaptic proteins in living neurons. *Neuron,* 78**,** 971-85.

GUPTA, P. B., ONDER, T. T., JIANG, G., TAO, K., KUPERWASSER, C., WEINBERG, R. A. & LANDER, E. S. 2009. Identification of selective inhibitors of cancer stem cells by high-throughput screening. *Cell,* 138**,** 645-59.

HAMERS-CASTERMAN, C., ATARHOUCH, T., MUYLDERMANS, S., ROBINSON, G., HAMERS, C., SONGA, E. B., BENDAHMAN, N. & HAMERS, R. 1993. Naturally occurring antibodies devoid of light chains. *Nature,* 363**,** 446-8.

HARMSEN, M. M. & DE HAARD, H. J. 2007. Properties, production, and applications of camelid single-domain antibody fragments. *Appl Microbiol Biotechnol,* 77**,** 13-22.

HARMSEN, M. M., RUULS, R. C., NIJMAN, I. J., NIEWOLD, T. A., FRENKEN, L. G. & DE GEUS, B. 2000. Llama heavy-chain V regions consist of at least four distinct subfamilies revealing novel sequence features. *Mol Immunol,* 37**,** 579-90.

HASKINS, J., GU, L., WITTCHEN, E. S., HIBBARD, J. & STEVENSON, B. R. 1998. ZO-3, a novel member of the MAGUK protein family found at the tight junction, interacts with ZO-1 and occludin. *J Cell Biol,* 141**,** 199-208.

HAVEL, L. S., KLINE, E. R., SALGUEIRO, A. M. & MARCUS, A. I. 2014. Vimentin regulates lung cancer cell adhesion through a VAV2-Rac1 pathway to control focal adhesion kinase activity. *Oncogene*.

HAY, E. D. 1968. Organization and fine structure of epithelium and mesenchyme in the developing chick embryo. *In:* FLEISCHMAJER R, B. R. (ed.) *Epithelial-mesenchymal interactions.* Baltimore: Williams and Wilkins.

HAY, E. D. 2005. The mesenchymal cell, its role in the embryo, and the remarkable signaling mechanisms that create it. *Dev Dyn,* 233**,** 706-20.

HAYNES, J., SRIVASTAVA, J., MADSON, N., WITTMANN, T. & BARBER, D. L. 2011. Dynamic actin remodeling during epithelial-mesenchymal transition depends on increased moesin expression. *Mol Biol Cell,* 22**,** 4750-64.

REFERENCES

HELDIN, C. H., LANDSTROM, M. & MOUSTAKAS, A. 2009. Mechanism of TGF-beta signaling to growth arrest, apoptosis, and epithelial-mesenchymal transition. *Curr Opin Cell Biol,* 21**,** 166-76.

HELFAND, B. T., MENDEZ, M. G., MURTHY, S. N., SHUMAKER, D. K., GRIN, B., MAHAMMAD, S., AEBI, U., WEDIG, T., WU, Y. I., HAHN, K. M., INAGAKI, M., HERRMANN, H. & GOLDMAN, R. D. 2011. Vimentin organization modulates the formation of lamellipodia. *Mol Biol Cell,* 22**,** 1274-89.

HELL, S. W. 2009. Microscopy and its focal switch. *Nat Methods,* 6**,** 24-32.

HELMA, J., CARDOSO, M. C., MUYLDERMANS, S. & LEONHARDT, H. 2015. Nanobodies and recombinant binders in cell biology. *J Cell Biol,* 209**,** 633-44.

HELMA, J., SCHMIDTHALS, K., LUX, V., NÜSKE, S., SCHOLZ, A. M., KRÄUSSLICH, H.-G., ROTHBAUER, U. & LEONHARDT, H. 2012a. Direct and Dynamic Detection of HIV-1 in Living Cells. *PloS one,* 7**,** e50026.

HELMA, J., SCHMIDTHALS, K., LUX, V., NUSKE, S., SCHOLZ, A. M., KRAUSSLICH, H. G., ROTHBAUER, U. & LEONHARDT, H. 2012b. Direct and dynamic detection of HIV-1 in living cells. *PLoS One,* 7**,** e50026.

HERRMANN, H., BAR, H., KREPLAK, L., STRELKOV, S. V. & AEBI, U. 2007. Intermediate filaments: from cell architecture to nanomechanics. *Nat Rev Mol Cell Biol,* 8**,** 562-73.

HERRMANN, H., HANER, M., BRETTEL, M., MULLER, S. A., GOLDIE, K. N., FEDTKE, B., LUSTIG, A., FRANKE, W. W. & AEBI, U. 1996. Structure and assembly properties of the intermediate filament protein vimentin: the role of its head, rod and tail domains. *J Mol Biol,* 264**,** 933-53.

HUANG, T., CHEN, Z. & FANG, L. 2013. Curcumin inhibits LPS-induced EMT through downregulation of NF-kappaB-Snail signaling in breast cancer cells. *Oncol Rep,* 29**,** 117-24.

IMAMURA, T., TAKASE, M., NISHIHARA, A., OEDA, E., HANAI, J., KAWABATA, M. & MIYAZONO, K. 1997. Smad6 inhibits signalling by the TGF-beta superfamily. *Nature,* 389**,** 622-6.

ISMAIL, I. A., KANG, H. S., LEE, H. J., CHANG, H., YUN, J., LEE, C. W., KIM, N. H., KIM, H. S., YOOK, J. I., HONG, S. H. & KWON, B. M. 2013. 2-Hydroxycinnamaldehyde inhibits the epithelial-mesenchymal transition in breast cancer cells. *Breast Cancer Res Treat,* 137**,** 697-708.

ITOH, M., MORITA, K. & TSUKITA, S. 1999. Characterization of ZO-2 as a MAGUK family member associated with tight as well as adherens junctions with a binding affinity to occludin and alpha catenin. *J Biol Chem,* 274**,** 5981-6.

IWAYA, K., NORIO, K. & MUKAI, K. 2007. Coexpression of Arp2 and WAVE2 predicts poor outcome in invasive breast carcinoma. *Mod Pathol,* 20**,** 339-43.

IZZI, L. & ATTISANO, L. 2004. Regulation of the TGFbeta signalling pathway by ubiquitin-mediated degradation. *Oncogene,* 23**,** 2071-8.

JAHN, S. C., LAW, M. E., CORSINO, P. E., PARKER, N. N., PHAM, K., DAVIS, B. J., LU, J. & LAW, B. K. 2012. An in vivo model of epithelial to mesenchymal transition reveals a mitogenic switch. *Cancer Lett,* 326**,** 183-90.

JOBLING, S. A., JARMAN, C., TEH, M. M., HOLMBERG, N., BLAKE, C. & VERHOEYEN, M. E. 2003. Immunomodulation of enzyme function in plants by single-domain antibody fragments. *Nat Biotechnol,* 21**,** 77-80.

JOHANSSON, K. A. & GRAPIN-BOTTON, A. 2002. Development and diseases of the pancreas. *Clin Genet,* 62**,** 14-23.

JORDAN, N. V., JOHNSON, G. L. & ABELL, A. N. 2011. Tracking the intermediate stages of epithelial-mesenchymal transition in epithelial stem cells and cancer. *Cell Cycle,* 10**,** 2865-73.

JUNG, H. Y. & YANG, J. 2015. Unraveling the TWIST between EMT and cancer stemness. *Cell Stem Cell,* 16**,** 1-2.

KABAT, E. A. & WU, T. T. 1991. Identical V region amino acid sequences and segments of sequences in antibodies of different specificities. Relative contributions of VH and VL genes, minigenes, and complementarity-determining regions to binding of antibody-combining sites. *J Immunol,* 147**,** 1709-19.

KAISER, P. D., MAIER, J., TRAENKLE, B., EMELE, F. & ROTHBAUER, U. 2014. Recent progress in generating intracellular functional antibody fragments to target and trace cellular components in living cells. *Biochim Biophys Acta,* 1844**,** 1933-1942.

KAJITA, M., MCCLINIC, K. N. & WADE, P. A. 2004. Aberrant expression of the transcription factors snail and slug alters the response to genotoxic stress. *Mol Cell Biol,* 24**,** 7559-66.

KAJITA, M., SUGIMURA, K., OHOKA, A., BURDEN, J., SUGANUMA, H., IKEGAWA, M., SHIMADA, T., KITAMURA, T., SHINDOH, M., ISHIKAWA, S., YAMAMOTO, S., SAITOH, S., YAKO, Y., TAKAHASHI, R., OKAJIMA, T., KIKUTA, J., MAIJIMA, Y., ISHII, M., TADA, M. & FUJITA, Y. 2014. Filamin acts as a key regulator in epithelial defence against transformed cells. *Nat Commun,* 5**,** 4428.

KALLURI, R. & NEILSON, E. G. 2003. Epithelial-mesenchymal transition and its implications for fibrosis. *J Clin Invest,* 112**,** 1776-84.

KALLURI, R. & WEINBERG, R. A. 2009. The basics of epithelial-mesenchymal transition. *J Clin Invest,* 119**,** 1420-8.

KATZ, E., DUBOIS-MARSHALL, S., SIMS, A. H., GAUTIER, P., CALDWELL, H., MEEHAN, R. R. & HARRISON, D. J. 2011. An in vitro model that recapitulates the epithelial to mesenchymal transition (EMT) in human breast cancer. *PLoS One,* 6**,** e17083.

KAUFHOLD, S. & BONAVIDA, B. 2014. Central role of Snail1 in the regulation of EMT and resistance in cancer: a target for therapeutic intervention. *J Exp Clin Cancer Res,* 33**,** 62.

KAWATA, M., KOINUMA, D., OGAMI, T., UMEZAWA, K., IWATA, C., WATABE, T. & MIYAZONO, K. 2012. TGF-beta-induced epithelial-mesenchymal transition of A549 lung adenocarcinoma cells is enhanced by pro-inflammatory cytokines derived from RAW 264.7 macrophage cells. *J Biochem,* 151**,** 205-16.

KIM, E. Y., KIM, A., KIM, S. K., KIM, H. J., CHANG, J., AHN, C. M. & CHANG, Y. S. 2014. Inhibition of mTORC1 induces loss of E-cadherin through AKT/GSK-3beta signaling-mediated upregulation of E-cadherin repressor complexes in non-small cell lung cancer cells. *Respir Res,* 15**,** 26.

KIM, Y. N., KOO, K. H., SUNG, J. Y., YUN, U. J. & KIM, H. 2012. Anoikis resistance: an essential prerequisite for tumor metastasis. *Int J Cell Biol,* 2012**,** 306879.

KIRCHHOFER, A., HELMA, J., SCHMIDTHALS, K., FRAUER, C., CUI, S., KARCHER, A., PELLIS, M., MUYLDERMANS, S., CASAS-DELUCCHI, C. S., CARDOSO, M. C., LEONHARDT, H., HOPFNER, K. P. & ROTHBAUER, U. 2010. Modulation of protein properties in living cells using nanobodies. *Nat Struct Mol Biol,* 17**,** 133-8.

KIRMSE, R., PORTET, S., MUCKE, N., AEBI, U., HERRMANN, H. & LANGOWSKI, J. 2007. A quantitative kinetic model for the in vitro assembly of intermediate filaments from tetrameric vimentin. *J Biol Chem,* 282**,** 18563-72.

KLOOSTER, R., EMAN, M. R., LE DUC, Q., VERHEESEN, P., VERRIPS, C. T., ROOVERS, R. C. & POST, J. A. 2009. Selection and characterization of KDEL-specific VHH antibody fragments and their application in the study of ER resident protein expression. *J Immunol Methods,* 342**,** 1-12.

KLOOSTER, R., MAASSEN, B. T., STAM, J. C., HERMANS, P. W., TEN HAAFT, M. R., DETMERS, F. J., DE HAARD, H. J., POST, J. A. & THEO VERRIPS, C. 2007. Improved

REFERENCES

anti-IgG and HSA affinity ligands: clinical application of VHH antibody technology. *J Immunol Methods,* 324**,** 1-12.

KNIGHTS, A. J., FUNNELL, A. P., CROSSLEY, M. & PEARSON, R. C. 2012. Holding Tight: Cell Junctions and Cancer Spread. *Trends Cancer Res,* 8**,** 61-69.

KOIDE, A., BAILEY, C. W., HUANG, X. & KOIDE, S. 1998. The fibronectin type III domain as a scaffold for novel binding proteins. *J Mol Biol,* 284**,** 1141-51.

KOIDE, A. & KOIDE, S. 2012. Affinity maturation of single-domain antibodies by yeast surface display. *Methods Mol Biol,* 911**,** 431-43.

KOTHARI, A. N., MI, Z., ZAPF, M. & KUO, P. C. 2014. Novel clinical therapeutics targeting the epithelial to mesenchymal transition. *Clin Transl Med,* 3**,** 35.

KUCZMARSKI, E. R. & GOLDMAN, R. D. 2007. Preparation and Microinjection of x-Rhodamine-Labeled Vimentin. *CSH Protoc,* 2007**,** pdb prot4676.

KUMMER, L., PARIZEK, P., RUBE, P., MILLGRAMM, B., PRINZ, A., MITTL, P. R., KAUFHOLZ, M., ZIMMERMANN, B., HERBERG, F. W. & PLUCKTHUN, A. 2012. Structural and functional analysis of phosphorylation-specific binders of the kinase ERK from designed ankyrin repeat protein libraries. *Proc Natl Acad Sci U S A,* 109**,** E2248-57.

KUNZ, C., BORGHOUTS, C., BUERGER, C. & GRONER, B. 2006. Peptide aptamers with binding specificity for the intracellular domain of the ErbB2 receptor interfere with AKT signaling and sensitize breast cancer cells to Taxol. *Mol Cancer Res,* 4**,** 983-98.

LAMOUILLE, S., CONNOLLY, E., SMYTH, J. W., AKHURST, R. J. & DERYNCK, R. 2012. TGF-beta-induced activation of mTOR complex 2 drives epithelial-mesenchymal transition and cell invasion. *J Cell Sci,* 125**,** 1259-73.

LAMOUILLE, S., XU, J. & DERYNCK, R. 2014. Molecular mechanisms of epithelial-mesenchymal transition. *Nat Rev Mol Cell Biol,* 15**,** 178-96.

LAPIERRE, L. A., TUMA, P. L., NAVARRE, J., GOLDENRING, J. R. & ANDERSON, J. M. 1999. VAP-33 localizes to both an intracellular vesicle population and with occludin at the tight junction. *J Cell Sci,* 112 (Pt 21)**,** 3723-32.

LAUWEREYS, M., ARBABI GHAHROUDI, M., DESMYTER, A., KINNE, J., HOLZER, W., DE GENST, E., WYNS, L. & MUYLDERMANS, S. 1998. Potent enzyme inhibitors derived from dromedary heavy-chain antibodies. *EMBO J,* 17**,** 3512-20.

LEE, J., HAHM, E. R., MARCUS, A. I. & SINGH, S. V. 2013. Withaferin A inhibits experimental epithelial-mesenchymal transition in MCF-10A cells and suppresses vimentin protein level in vivo in breast tumors. *Mol Carcinog*.

LEE, J. M., DEDHAR, S., KALLURI, R. & THOMPSON, E. W. 2006. The epithelial-mesenchymal transition: new insights in signaling, development, and disease. *J Cell Biol,* 172**,** 973-81.

LEMMON, M. A. & SCHLESSINGER, J. 2010. Cell signaling by receptor tyrosine kinases. *Cell,* 141**,** 1117-34.

LI, Q., CHEN, C., KAPADIA, A., ZHOU, Q., HARPER, M. K., SCHAACK, J. & LABARBERA, D. V. 2011. 3D models of epithelial-mesenchymal transition in breast cancer metastasis: high-throughput screening assay development, validation, and pilot screen. *J Biomol Screen,* 16**,** 141-54.

LI, T., BOURGEOIS, J. P., CELLI, S., GLACIAL, F., LE SOURD, A. M., MECHERI, S., WEKSLER, B., ROMERO, I., COURAUD, P. O., ROUGEON, F. & LAFAYE, P. 2012. Cell-penetrating anti-GFAP VHH and corresponding fluorescent fusion protein VHH-GFP spontaneously cross the blood-brain barrier and specifically recognize astrocytes: application to brain imaging. *FASEB J,* 26**,** 3969-79.

LI, X., DENG, W., NAIL, C. D., BAILEY, S. K., KRAUS, M. H., RUPPERT, J. M. & LOBO-RUPPERT, S. M. 2006. Snail induction is an early response to Gli1 that determines the efficiency of epithelial transformation. *Oncogene,* 25**,** 609-21.

LI, Y., FANNING, A. S., ANDERSON, J. M. & LAVIE, A. 2005. Structure of the conserved cytoplasmic C-terminal domain of occludin: identification of the ZO-1 binding surface. *J Mol Biol,* 352**,** 151-64.

LILIENBAUM, A. & PAULIN, D. 1993. Activation of the human vimentin gene by the Tax human T-cell leukemia virus. I. Mechanisms of regulation by the NF-kappa B transcription factor. *J Biol Chem,* 268**,** 2180-8.

LIM, J. & THIERY, J. P. 2012. Epithelial-mesenchymal transitions: insights from development. *Development,* 139**,** 3471-86.

LIU, N., LI, Y., SU, S., WANG, N., WANG, H. & LI, J. 2013. Inhibition of cell migration by ouabain in the A549 human lung cancer cell line. *Oncol Lett,* 6**,** 475-479.

LIU, Y. 2004. Epithelial to mesenchymal transition in renal fibrogenesis: pathologic significance, molecular mechanism, and therapeutic intervention. *J Am Soc Nephrol,* 15**,** 1-12.

MANI, S. A., GUO, W., LIAO, M. J., EATON, E. N., AYYANAN, A., ZHOU, A. Y., BROOKS, M., REINHARD, F., ZHANG, C. C., SHIPITSIN, M., CAMPBELL, L. L., POLYAK, K., BRISKEN, C., YANG, J. & WEINBERG, R. A. 2008. The epithelial-mesenchymal transition generates cells with properties of stem cells. *Cell,* 133**,** 704-15.

MANI, S. A., YANG, J., BROOKS, M., SCHWANINGER, G., ZHOU, A., MIURA, N., KUTOK, J. L., HARTWELL, K., RICHARDSON, A. L. & WEINBERG, R. A. 2007. Mesenchyme Forkhead 1 (FOXC2) plays a key role in metastasis and is associated with aggressive basal-like breast cancers. *Proc Natl Acad Sci U S A,* 104**,** 10069-74.

MARTIN, T. A., MANSEL, R. E. & JIANG, W. G. 2010. Loss of occludin leads to the progression of human breast cancer. *Int J Mol Med,* 26**,** 723-34.

MASSZI, A., DI CIANO, C., SIROKMANY, G., ARTHUR, W. T., ROTSTEIN, O. D., WANG, J., MCCULLOCH, C. A., ROSIVALL, L., MUCSI, I. & KAPUS, A. 2003. Central role for Rho in TGF-beta1-induced alpha-smooth muscle actin expression during epithelial-mesenchymal transition. *Am J Physiol Renal Physiol,* 284**,** F911-24.

MEDICI, D., HAY, E. D. & GOODENOUGH, D. A. 2006. Cooperation between snail and LEF-1 transcription factors is essential for TGF-beta1-induced epithelial-mesenchymal transition. *Mol Biol Cell,* 17**,** 1871-9.

MENDEZ, M. G., KOJIMA, S. & GOLDMAN, R. D. 2010. Vimentin induces changes in cell shape, motility, and adhesion during the epithelial to mesenchymal transition. *FASEB J,* 24**,** 1838-51.

MEYER, C., DZIERAN, J., LIU, Y., SCHINDLER, F., MUNKER, S., MULLER, A., COULOUARN, C. & DOOLEY, S. 2013. Distinct dedifferentiation processes affect caveolin-1 expression in hepatocytes. *Cell Commun Signal,* 11**,** 6.

MEYER, C., HAHN, U. & RENTMEISTER, A. 2011. Cell-specific aptamers as emerging therapeutics. *J Nucleic Acids,* 2011**,** 904750.

MIELE, L., GOLDE, T. & OSBORNE, B. 2006. Notch signaling in cancer. *Curr Mol Med,* 6**,** 905-18.

MIKHAYLOVA, M., CLOIN, B. M., FINAN, K., VAN DEN BERG, R., TEEUW, J., KIJANKA, M. M., SOKOLOWSKI, M., KATRUKHA, E. A., MAIDORN, M., OPAZO, F., MOUTEL, S., VANTARD, M., PEREZ, F., VAN BERGEN EN HENEGOUWEN, P. M., HOOGENRAAD, C. C., EWERS, H. & KAPITEIN, L. C. 2015. Resolving bundled microtubules using anti-tubulin nanobodies. *Nat Commun,* 6**,** 7933.

MINGOT, J. M., VEGA, S., MAESTRO, B., SANZ, J. M. & NIETO, M. A. 2009. Characterization of Snail nuclear import pathways as representatives of C2H2 zinc finger transcription factors. *J Cell Sci,* 122**,** 1452-60.

REFERENCES

MOHAN, R., HAMMERS, H. J., BARGAGNA-MOHAN, P., ZHAN, X. H., HERBSTRITT, C. J., RUIZ, A., ZHANG, L., HANSON, A. D., CONNER, B. P., ROUGAS, J. & PRIBLUDA, V. S. 2004. Withaferin A is a potent inhibitor of angiogenesis. *Angiogenesis,* 7**,** 115-22.

MONEGAL, A., AMI, D., MARTINELLI, C., HUANG, H., ALIPRANDI, M., CAPASSO, P., FRANCAVILLA, C., OSSOLENGO, G. & DE MARCO, A. 2009. Immunological applications of single-domain llama recombinant antibodies isolated from a naive library. *Protein Eng Des Sel,* 22**,** 273-80.

MORENO-BUENO, G., PEINADO, H., MOLINA, P., OLMEDA, D., CUBILLO, E., SANTOS, V., PALACIOS, J., PORTILLO, F. & CANO, A. 2009. The morphological and molecular features of the epithelial-to-mesenchymal transition. *Nat Protoc,* 4**,** 1591-613.

MORRIS, H. T. & MACHESKY, L. M. 2015. Actin cytoskeletal control during epithelial to mesenchymal transition: focus on the pancreas and intestinal tract. *Br J Cancer,* 112**,** 613-20.

MUYLDERMANS, S. 2013. Nanobodies: natural single-domain antibodies. *Annu Rev Biochem,* 82**,** 775-97.

MUYLDERMANS, S., ATARHOUCH, T., SALDANHA, J., BARBOSA, J. A. & HAMERS, R. 1994. Sequence and structure of VH domain from naturally occurring camel heavy chain immunoglobulins lacking light chains. *Protein Eng,* 7**,** 1129-35.

NAKAO, A., AFRAKHTE, M., MOREN, A., NAKAYAMA, T., CHRISTIAN, J. L., HEUCHEL, R., ITOH, S., KAWABATA, M., HELDIN, N. E., HELDIN, C. H. & TEN DIJKE, P. 1997. Identification of Smad7, a TGFbeta-inducible antagonist of TGF-beta signalling. *Nature,* 389**,** 631-5.

NGUYEN-DUC, T., PEETERS, E., MUYLDERMANS, S., CHARLIER, D. & HASSANZADEH-GHASSABEH, G. 2013. Nanobody(R)-based chromatin immunoprecipitation/micro-array analysis for genome-wide identification of transcription factor DNA binding sites. *Nucleic Acids Res,* 41**,** e59.

NGUYEN, V. K., HAMERS, R., WYNS, L. & MUYLDERMANS, S. 1999. Loss of splice consensus signal is responsible for the removal of the entire C(H)1 domain of the functional camel IGG2A heavy-chain antibodies. *Mol Immunol,* 36**,** 515-24.

NGUYEN, V. K., HAMERS, R., WYNS, L. & MUYLDERMANS, S. 2000. Camel heavy-chain antibodies: diverse germline V(H)H and specific mechanisms enlarge the antigen-binding repertoire. *EMBO J,* 19**,** 921-30.

NGUYEN, V. K., SU, C., MUYLDERMANS, S. & VAN DER LOO, W. 2002. Heavy-chain antibodies in Camelidae; a case of evolutionary innovation. *Immunogenetics,* 54**,** 39-47.

NIESSEN, C. M. 2007. Tight junctions/adherens junctions: basic structure and function. *J Invest Dermatol,* 127**,** 2525-32.

NIETO, M. A. 2002. The snail superfamily of zinc-finger transcription factors. *Nat Rev Mol Cell Biol,* 3**,** 155-66.

NIETO, M. A. 2013. Epithelial plasticity: a common theme in embryonic and cancer cells. *Science,* 342**,** 1234850.

NILSSON, J., HELOU, K., KOVACS, A., BENDAHL, P. O., BJURSELL, G., FERNO, M., CARLSSON, P. & KANNIUS-JANSON, M. 2010. Nuclear Janus-activated kinase 2/nuclear factor 1-C2 suppresses tumorigenesis and epithelial-to-mesenchymal transition by repressing Forkhead box F1. *Cancer Res,* 70**,** 2020-9.

NUTTALL, S. D., KRISHNAN, U. V., HATTARKI, M., DE GORI, R., IRVING, R. A. & HUDSON, P. J. 2001. Isolation of the new antigen receptor from wobbegong sharks, and use as a scaffold for the display of protein loop libraries. *Mol Immunol,* 38**,** 313-26.

OCANA, O. H., CORCOLES, R., FABRA, A., MORENO-BUENO, G., ACLOQUE, H., VEGA, S., BARRALLO-GIMENO, A., CANO, A. & NIETO, M. A. 2012. Metastatic colonization

requires the repression of the epithelial-mesenchymal transition inducer Prrx1. *Cancer Cell,* 22**,** 709-24.

ORBAN, E., SZABO, E., LOTZ, G., KUPCSULIK, P., PASKA, C., SCHAFF, Z. & KISS, A. 2008. Different expression of occludin and ZO-1 in primary and metastatic liver tumors. *Pathol Oncol Res,* 14**,** 299-306.

OTSUKI, S., INOKUCHI, M., ENJOJI, M., ISHIKAWA, T., TAKAGI, Y., KATO, K., YAMADA, H., KOJIMA, K. & SUGIHARA, K. 2011. Vimentin expression is associated with decreased survival in gastric cancer. *Oncol Rep,* 25**,** 1235-42.

OZDAMAR, B., BOSE, R., BARRIOS-RODILES, M., WANG, H. R., ZHANG, Y. & WRANA, J. L. 2005. Regulation of the polarity protein Par6 by TGFbeta receptors controls epithelial cell plasticity. *Science,* 307**,** 1603-9.

PAN, Y., LI, X., DUAN, J., YUAN, L., FAN, S., FAN, J., XIAOKAITI, Y., YANG, H., WANG, Y. & LI, X. 2015. Enoxaparin Sensitizes Human Non-Small-Cell Lung Carcinomas to Gefitinib by Inhibiting DOCK1 Expression, Vimentin Phosphorylation, and Akt Activation. *Mol Pharmacol,* 87**,** 378-90.

PANZA, P., MAIER, J., SCHMEES, C., ROTHBAUER, U. & SOLLNER, C. 2015. Live imaging of endogenous protein dynamics in zebrafish using chromobodies. *Development,* 142**,** 1879-84.

PARDON, E., LAEREMANS, T., TRIEST, S., RASMUSSEN, S. G., WOHLKONIG, A., RUF, A., MUYLDERMANS, S., HOL, W. G., KOBILKA, B. K. & STEYAERT, J. 2014. A general protocol for the generation of Nanobodies for structural biology. *Nat Protoc,* 9**,** 674-93.

PARSONS, J. T., HORWITZ, A. R. & SCHWARTZ, M. A. 2010. Cell adhesion: integrating cytoskeletal dynamics and cellular tension. *Nat Rev Mol Cell Biol,* 11**,** 633-43.

PASQUIER, J., ABU-KAOUD, N., AL THANI, H. & RAFII, A. 2015. Epithelial to Mesenchymal Transition in a Clinical Perspective. *Journal of Oncology*.

PEINADO, H., BALLESTAR, E., ESTELLER, M. & CANO, A. 2004. Snail mediates E-cadherin repression by the recruitment of the Sin3A/histone deacetylase 1 (HDAC1)/HDAC2 complex. *Mol Cell Biol,* 24**,** 306-19.

PEINADO, H., OLMEDA, D. & CANO, A. 2007. Snail, Zeb and bHLH factors in tumour progression: an alliance against the epithelial phenotype? *Nat Rev Cancer,* 7**,** 415-28.

PEIRO, S., ESCRIVA, M., PUIG, I., BARBERA, M. J., DAVE, N., HERRANZ, N., LARRIBA, M. J., TAKKUNEN, M., FRANCI, C., MUNOZ, A., VIRTANEN, I., BAULIDA, J. & GARCIA DE HERREROS, A. 2006. Snail1 transcriptional repressor binds to its own promoter and controls its expression. *Nucleic Acids Res,* 34**,** 2077-84.

PELLIS, M., PARDON, E., ZOLGHADR, K., ROTHBAUER, U., VINCKE, C., KINNE, J., DIERYNCK, I., HERTOGS, K., LEONHARDT, H., MESSENS, J., MUYLDERMANS, S. & CONRATH, K. 2012. A bacterial-two-hybrid selection system for one-step isolation of intracellularly functional Nanobodies. *Arch Biochem Biophys,* 526**,** 114-23.

PHUA, D. C., HUMBERT, P. O. & HUNZIKER, W. 2009. Vimentin regulates scribble activity by protecting it from proteasomal degradation. *Mol Biol Cell,* 20**,** 2841-55.

PLUCKTHUN, A. 2015. Designed ankyrin repeat proteins (DARPins): binding proteins for research, diagnostics, and therapy. *Annu Rev Pharmacol Toxicol,* 55**,** 489-511.

QIAO, B., JOHNSON, N. W. & GAO, J. 2010. Epithelial-mesenchymal transition in oral squamous cell carcinoma triggered by transforming growth factor-beta1 is Snail family-dependent and correlates with matrix metalloproteinase-2 and -9 expressions. *Int J Oncol,* 37**,** 663-8.

RALEIGH, D. R., BOE, D. M., YU, D., WEBER, C. R., MARCHIANDO, A. M., BRADFORD, E. M., WANG, Y., WU, L., SCHNEEBERGER, E. E., SHEN, L. & TURNER, J. R. 2011. Occludin S408 phosphorylation regulates tight junction protein interactions and barrier function. *J Cell Biol,* 193**,** 565-82.

REFERENCES

RASK-ANDERSEN, M., ALMEN, M. S. & SCHIOTH, H. B. 2011. Trends in the exploitation of novel drug targets. *Nat Rev Drug Discov,* 10**,** 579-90.

RASMUSSEN, S. G., CHOI, H. J., FUNG, J. J., PARDON, E., CASAROSA, P., CHAE, P. S., DEVREE, B. T., ROSENBAUM, D. M., THIAN, F. S., KOBILKA, T. S., SCHNAPP, A., KONETZKI, I., SUNAHARA, R. K., GELLMAN, S. H., PAUTSCH, A., STEYAERT, J., WEIS, W. I. & KOBILKA, B. K. 2011. Structure of a nanobody-stabilized active state of the beta(2) adrenoceptor. *Nature,* 469**,** 175-80.

RAST, J. P., AMEMIYA, C. T., LITMAN, R. T., STRONG, S. J. & LITMAN, G. W. 1998. Distinct patterns of IgH structure and organization in a divergent lineage of chrondrichthyan fishes. *Immunogenetics,* 47**,** 234-45.

RICHARDSON, F., YOUNG, G. D., SENNELLO, R., WOLF, J., ARGAST, G. M., MERCADO, P., DAVIES, A., EPSTEIN, D. M. & WACKER, B. 2012. The evaluation of E-Cadherin and vimentin as biomarkers of clinical outcomes among patients with non-small cell lung cancer treated with erlotinib as second- or third-line therapy. *Anticancer Res,* 32**,** 537-52.

RIDLEY, A. J. 2011. Life at the leading edge. *Cell,* 145**,** 1012-22.

RIEDL, J., CREVENNA, A. H., KESSENBROCK, K., YU, J. H., NEUKIRCHEN, D., BISTA, M., BRADKE, F., JENNE, D., HOLAK, T. A., WERB, Z., SIXT, M. & WEDLICH-SOLDNER, R. 2008. Lifeact: a versatile marker to visualize F-actin. *Nat Methods,* 5**,** 605-7.

RIEDL, J., FLYNN, K. C., RADUCANU, A., GARTNER, F., BECK, G., BOSL, M., BRADKE, F., MASSBERG, S., ASZODI, A., SIXT, M. & WEDLICH-SOLDNER, R. 2010. Lifeact mice for studying F-actin dynamics. *Nat Methods,* 7**,** 168-9.

RIES, J., KAPLAN, C., PLATONOVA, E., EGHLIDI, H. & EWERS, H. 2012. A simple, versatile method for GFP-based super-resolution microscopy via nanobodies. *Nat Methods,* 9**,** 582-4.

RISOLINO, M., MANDIA, N., IAVARONE, F., DARDAEI, L., LONGOBARDI, E., FERNANDEZ, S., TALOTTA, F., BIANCHI, F., PISATI, F., SPAGGIARI, L., HARTER, P. N., MITTELBRONN, M., SCHULTE, D., INCORONATO, M., DI FIORE, P. P., BLASI, F. & VERDE, P. 2014. Transcription factor PREP1 induces EMT and metastasis by controlling the TGF-beta-SMAD3 pathway in non-small cell lung adenocarcinoma. *Proc Natl Acad Sci U S A,* 111**,** E3775-84.

RITTLING, S. R., COUTINHO, L., AMRAM, T. & KOLBE, M. 1989. AP-1/jun binding sites mediate serum inducibility of the human vimentin promoter. *Nucleic Acids Res,* 17**,** 1619-33.

ROCCHETTI, A., HAWES, C. & KRIECHBAUMER, V. 2014. Fluorescent labelling of the actin cytoskeleton in plants using a cameloid antibody. *Plant Methods,* 10**,** 12.

ROTHBAUER, U., ZOLGHADR, K., MUYLDERMANS, S., SCHEPERS, A., CARDOSO, M. C. & LEONHARDT, H. 2008. A versatile nanotrap for biochemical and functional studies with fluorescent fusion proteins. *Mol Cell Proteomics,* 7**,** 282-9.

ROTHBAUER, U., ZOLGHADR, K., TILLIB, S., NOWAK, D., SCHERMELLEH, L., GAHL, A., BACKMANN, N., CONRATH, K., MUYLDERMANS, S., CARDOSO, M. C. & LEONHARDT, H. 2006. Targeting and tracing antigens in live cells with fluorescent nanobodies. *Nat Methods,* 3**,** 887-9.

SADLER, N. M., HARRIS, B. R., METZGER, B. A. & KIRSHNER, J. 2013. N-cadherin impedes proliferation of the multiple myeloma cancer stem cells. *Am J Blood Res,* 3**,** 271-85.

SAHLGREN, C., GUSTAFSSON, M. V., JIN, S., POELLINGER, L. & LENDAHL, U. 2008. Notch signaling mediates hypoxia-induced tumor cell migration and invasion. *Proc Natl Acad Sci U S A,* 105**,** 6392-7.

SATELLI, A. & LI, S. 2011. Vimentin in cancer and its potential as a molecular target for cancer therapy. *Cell Mol Life Sci,* 68**,** 3033-46.

SATO, M., SAWAHATA, R., SAKUMA, C., TAKENOUCHI, T. & KITANI, H. 2013a. Single domain intrabodies against WASP inhibit TCR-induced immune responses in transgenic mice T cells. *Sci Rep,* 3**,** 3003.

SATO, Y., MUKAI, M., UEDA, J., MURAKI, M., STASEVICH, T. J., HORIKOSHI, N., KUJIRAI, T., KITA, H., KIMURA, T., HIRA, S., OKADA, Y., HAYASHI-TAKANAKA, Y., OBUSE, C., KURUMIZAKA, H., KAWAHARA, A., YAMAGATA, K., NOZAKI, N. & KIMURA, H. 2013b. Genetically encoded system to track histone modification in vivo. *Sci Rep,* 3**,** 2436.

SCHATZ, D. G., OETTINGER, M. A. & SCHLISSEL, M. S. 1992. V(D)J recombination: molecular biology and regulation. *Annu Rev Immunol,* 10**,** 359-83.

SCHMIDTHALS, K. 2013. Generation and characterization of heavy-chain antibodies derived from Camelids. *PhD thesis.*

SCHORNACK, S., FUCHS, R., HUITEMA, E., ROTHBAUER, U., LIPKA, V. & KAMOUN, S. 2009. Protein mislocalization in plant cells using a GFP-binding chromobody. *The Plant Journal,* 60**,** 744-754.

SCHYSCHKA, L., SANCHEZ, J. J., WANG, Z., BURKHARDT, B., MULLER-VIEIRA, U., ZEILINGER, K., BACHMANN, A., NADALIN, S., DAMM, G. & NUSSLER, A. K. 2013. Hepatic 3D cultures but not 2D cultures preserve specific transporter activity for acetaminophen-induced hepatotoxicity. *Arch Toxicol,* 87**,** 1581-93.

SHANKAR, J. & NABI, I. R. 2015. Actin cytoskeleton regulation of epithelial-mesenchymal transition in metastatic cancer cells. *PLoS One,* 10**,** e0119954.

SHINTANI, Y., FUKUMOTO, Y., CHAIKA, N., GRANDGENETT, P. M., HOLLINGSWORTH, M. A., WHEELOCK, M. J. & JOHNSON, K. R. 2008. ADH-1 suppresses N-cadherin-dependent pancreatic cancer progression. *Int J Cancer,* 122**,** 71-7.

SHOHAT, B., GITTER, S., ABRAHAM, A. & LAVIE, D. 1967. Antitumor activity of withaferin A (NSC-101088). *Cancer Chemother Rep,* 51**,** 271-6.

SIBLER, A. P., COURTETE, J., MULLER, C. D., ZEDER-LUTZ, G. & WEISS, E. 2005. Extended half-life upon binding of destabilized intrabodies allows specific detection of antigen in mammalian cells. *FEBS J,* 272**,** 2878-91.

SIHAG, R. K., INAGAKI, M., YAMAGUCHI, T., SHEA, T. B. & PANT, H. C. 2007. Role of phosphorylation on the structural dynamics and function of types III and IV intermediate filaments. *Exp Cell Res,* 313**,** 2098-109.

SNIDER, N. T. & OMARY, M. B. 2014. Post-translational modifications of intermediate filament proteins: mechanisms and functions. *Nat Rev Mol Cell Biol,* 15**,** 163-77.

SPRACKLEN, A. J., FAGAN, T. N., LOVANDER, K. E. & TOOTLE, T. L. 2014. The pros and cons of common actin labeling tools for visualizing actin dynamics during Drosophila oogenesis. *Dev Biol,* 393**,** 209-26.

STADLER, C., REXHEPAJ, E., SINGAN, V. R., MURPHY, R. F., PEPPERKOK, R., UHLEN, M., SIMPSON, J. C. & LUNDBERG, E. 2013. Immunofluorescence and fluorescent-protein tagging show high correlation for protein localization in mammalian cells. *Nat Methods,* 10**,** 315-23.

STEIGEMANN, P. & GERLICH, D. W. 2009. Cytokinetic abscission: cellular dynamics at the midbody. *Trends Cell Biol,* 19**,** 606-16.

SUZUKI, T., ELIAS, B. C., SETH, A., SHEN, L., TURNER, J. R., GIORGIANNI, F., DESIDERIO, D., GUNTAKA, R. & RAO, R. 2009. PKC eta regulates occludin phosphorylation and epithelial tight junction integrity. *Proc Natl Acad Sci U S A,* 106**,** 61-6.

SZENT-GYORGYI, C., SCHMIDT, B. F., CREEGER, Y., FISHER, G. W., ZAKEL, K. L., ADLER, S., FITZPATRICK, J. A., WOOLFORD, C. A., YAN, Q., VASILEV, K. V., BERGET, P. B.,

REFERENCES

BRUCHEZ, M. P., JARVIK, J. W. & WAGGONER, A. 2008. Fluorogen-activating single-chain antibodies for imaging cell surface proteins. *Nat Biotechnol,* 26**,** 235-40.

TANG, J. C., SZIKRA, T., KOZOROVITSKIY, Y., TEIXIERA, M., SABATINI, B. L., ROSKA, B. & CEPKO, C. L. 2013. A nanobody-based system using fluorescent proteins as scaffolds for cell-specific gene manipulation. *Cell,* 154**,** 928-39.

TANIMIZU, N. & MIYAJIMA, A. 2007. Molecular mechanism of liver development and regeneration. *Int Rev Cytol,* 259**,** 1-48.

TARIN, D., THOMPSON, E. W. & NEWGREEN, D. F. 2005. The fallacy of epithelial-mesenchymal transition in neoplasia. *Cancer Res,* 65**,** 5996-6000; discussion 6000-1.

TERWISSCHA VAN SCHELTINGA, A. G., LUB-DE HOOGE, M. N., HINNER, M. J., VERHEIJEN, R. B., ALLERSDORFER, A., HULSMEYER, M., NAGENGAST, W. B., SCHRODER, C. P., KOSTERINK, J. G., DE VRIES, E. G., AUDOLY, L. & OLWILL, S. A. 2014. In vivo visualization of MET tumor expression and anticalin biodistribution with the MET-specific anticalin 89Zr-PRS-110 PET tracer. *J Nucl Med,* 55**,** 665-71.

THAIPARAMBIL, J. T., BENDER, L., GANESH, T., KLINE, E., PATEL, P., LIU, Y., TIGHIOUART, M., VERTINO, P. M., HARVEY, R. D., GARCIA, A. & MARCUS, A. I. 2011. Withaferin A inhibits breast cancer invasion and metastasis at sub-cytotoxic doses by inducing vimentin disassembly and serine 56 phosphorylation. *Int J Cancer,* 129**,** 2744-55.

THIERY, J. P., ACLOQUE, H., HUANG, R. Y. & NIETO, M. A. 2009. Epithelial-mesenchymal transitions in development and disease. *Cell,* 139**,** 871-90.

THIERY, J. P. & LIM, C. T. 2013. Tumor dissemination: an EMT affair. *Cancer Cell,* 23**,** 272-3.

THIERY, J. P. & SLEEMAN, J. P. 2006. Complex networks orchestrate epithelial-mesenchymal transitions. *Nat Rev Mol Cell Biol,* 7**,** 131-42.

TIMMERMAN, L. A., GREGO-BESSA, J., RAYA, A., BERTRAN, E., PEREZ-POMARES, J. M., DIEZ, J., ARANDA, S., PALOMO, S., MCCORMICK, F., IZPISUA-BELMONTE, J. C. & DE LA POMPA, J. L. 2004. Notch promotes epithelial-mesenchymal transition during cardiac development and oncogenic transformation. *Genes Dev,* 18**,** 99-115.

TIRINO, V., CAMERLINGO, R., BIFULCO, K., IROLLO, E., MONTELLA, R., PAINO, F., SESSA, G., CARRIERO, M. V., NORMANNO, N., ROCCO, G. & PIROZZI, G. 2013. TGF-beta1 exposure induces epithelial to mesenchymal transition both in CSCs and non-CSCs of the A549 cell line, leading to an increase of migration ability in the CD133+ A549 cell fraction. *Cell Death Dis,* 4**,** e620.

TOBIOKA, H., TOKUNAGA, Y., ISOMURA, H., KOKAI, Y., YAMAGUCHI, J. & SAWADA, N. 2004. Expression of occludin, a tight-junction-associated protein, in human lung carcinomas. *Virchows Arch,* 445**,** 472-6.

TOLEIKIS, L., BRODERS, O. & DUBEL, S. 2004. Cloning single-chain antibody fragments (scFv) from hybridoma cells. *Methods Mol Med,* 94**,** 447-58.

TRAENKLE, B., EMELE, F., ANTON, R., POETZ, O., HAEUSSLER, R. S., MAIER, J., KAISER, P. D., SCHOLZ, A. M., NUESKE, S., BUCHFELLNER, A., ROMER, T. & ROTHBAUER, U. 2015. Monitoring interactions and dynamics of endogenous beta-catenin with intracellular nanobodies in living cells. *Mol Cell Proteomics*.

TSAI, J. H., DONAHER, J. L., MURPHY, D. A., CHAU, S. & YANG, J. 2012. Spatiotemporal regulation of epithelial-mesenchymal transition is essential for squamous cell carcinoma metastasis. *Cancer Cell,* 22**,** 725-36.

TSIEN, R. Y. 1998. The green fluorescent protein. *Annu Rev Biochem,* 67**,** 509-44.

VAN AUDENHOVE, I., VAN IMPE, K., RUANO-GALLEGO, D., DE CLERCQ, S., DE MUYNCK, K., VANLOO, B., VERSTRAETE, H., FERNANDEZ, L. A. & GETTEMANS, J.

2013. Mapping cytoskeletal protein function in cells by means of nanobodies. *Cytoskeleton (Hoboken),* 70**,** 604-22.

VINAS-CASTELLS, R., BELTRAN, M., VALLS, G., GOMEZ, I., GARCIA, J. M., MONTSERRAT-SENTIS, B., BAULIDA, J., BONILLA, F., DE HERREROS, A. G. & DIAZ, V. M. 2010. The hypoxia-controlled FBXL14 ubiquitin ligase targets SNAIL1 for proteasome degradation. *J Biol Chem,* 285**,** 3794-805.

VINCENT, T., NEVE, E. P., JOHNSON, J. R., KUKALEV, A., ROJO, F., ALBANELL, J., PIETRAS, K., VIRTANEN, I., PHILIPSON, L., LEOPOLD, P. L., CRYSTAL, R. G., DE HERREROS, A. G., MOUSTAKAS, A., PETTERSSON, R. F. & FUXE, J. 2009. A SNAIL1-SMAD3/4 transcriptional repressor complex promotes TGF-beta mediated epithelial-mesenchymal transition. *Nat Cell Biol,* 11**,** 943-50.

VISINTIN, M., SETTANNI, G., MARITAN, A., GRAZIOSI, S., MARKS, J. D. & CATTANEO, A. 2002. The intracellular antibody capture technology (IACT): towards a consensus sequence for intracellular antibodies. *J Mol Biol,* 317**,** 73-83.

VISINTIN, M., TSE, E., AXELSON, H., RABBITTS, T. H. & CATTANEO, A. 1999. Selection of antibodies for intracellular function using a two-hybrid in vivo system. *Proc Natl Acad Sci U S A,* 96**,** 11723-8.

VU, K. B., GHAHROUDI, M. A., WYNS, L. & MUYLDERMANS, S. 1997. Comparison of llama VH sequences from conventional and heavy chain antibodies. *Mol Immunol,* 34**,** 1121-31.

VUORILUOTO, K., HAUGEN, H., KIVILUOTO, S., MPINDI, J. P., NEVO, J., GJERDRUM, C., TIRON, C., LORENS, J. B. & IVASKA, J. 2011. Vimentin regulates EMT induction by Slug and oncogenic H-Ras and migration by governing Axl expression in breast cancer. *Oncogene,* 30**,** 1436-48.

WANG, H., ZHANG, G., ZHANG, H., ZHANG, F., ZHOU, B., NING, F., WANG, H. S., CAI, S. H. & DU, J. 2014. Acquisition of epithelial-mesenchymal transition phenotype and cancer stem cell-like properties in cisplatin-resistant lung cancer cells through AKT/beta-catenin/Snail signaling pathway. *Eur J Pharmacol,* 723**,** 156-66.

WANG, H., ZHANG, H., TANG, L., CHEN, H., WU, C., ZHAO, M., YANG, Y., CHEN, X. & LIU, G. 2013a. Resveratrol inhibits TGF-beta1-induced epithelial-to-mesenchymal transition and suppresses lung cancer invasion and metastasis. *Toxicology,* 303**,** 139-46.

WANG, Y., SHI, J., CHAI, K., YING, X. & ZHOU, B. P. 2013b. The Role of Snail in EMT and Tumorigenesis. *Curr Cancer Drug Targets,* 13**,** 963-72.

WOODHAM, E. F. & MACHESKY, L. M. 2014. Polarised cell migration: intrinsic and extrinsic drivers. *Curr Opin Cell Biol,* 30**,** 25-32.

WOOLVEN, B. P., FRENKEN, L. G., VAN DER LOGT, P. & NICHOLLS, P. J. 1999. The structure of the llama heavy chain constant genes reveals a mechanism for heavy-chain antibody formation. *Immunogenetics,* 50**,** 98-101.

WU, K. J., ZENG, J., ZHU, G. D., ZHANG, L. L., ZHANG, D., LI, L., FAN, J. H., WANG, X. Y. & HE, D. L. 2009a. Silibinin inhibits prostate cancer invasion, motility and migration by suppressing vimentin and MMP-2 expression. *Acta Pharmacol Sin,* 30**,** 1162-8.

WU, T. T., JOHNSON, G. & KABAT, E. A. 1993. Length distribution of CDRH3 in antibodies. *Proteins,* 16**,** 1-7.

WU, Y., EVERS, B. M. & ZHOU, B. P. 2009b. Small C-terminal domain phosphatase enhances snail activity through dephosphorylation. *J Biol Chem,* 284**,** 640-8.

WU, Y., ZHANG, X., SALMON, M., LIN, X. & ZEHNER, Z. E. 2007. TGFbeta1 regulation of vimentin gene expression during differentiation of the C2C12 skeletal myogenic cell line requires Smads, AP-1 and Sp1 family members. *Biochim Biophys Acta,* 1773**,** 427-39.

REFERENCES

WU, Y., ZHANG, X. & ZEHNER, Z. E. 2003. c-Jun and the dominant-negative mutant, TAM67, induce vimentin gene expression by interacting with the activator Sp1. *Oncogene,* 22**,** 8891-901.

XIE, L., LAW, B. K., CHYTIL, A. M., BROWN, K. A., AAKRE, M. E. & MOSES, H. L. 2004. Activation of the Erk pathway is required for TGF-beta1-induced EMT in vitro. *Neoplasia,* 6**,** 603-10.

XU, J., LAMOUILLE, S. & DERYNCK, R. 2009. TGF-beta-induced epithelial to mesenchymal transition. *Cell Res,* 19**,** 156-72.

YAMAGUCHI, H. & CONDEELIS, J. 2007. Regulation of the actin cytoskeleton in cancer cell migration and invasion. *Biochim Biophys Acta,* 1773**,** 642-52.

YAMASHITA, N., TOKUNAGA, E., KITAO, H., HISAMATSU, Y., TAKETANI, K., AKIYOSHI, S., OKADA, S., AISHIMA, S., MORITA, M. & MAEHARA, Y. 2013. Vimentin as a poor prognostic factor for triple-negative breast cancer. *J Cancer Res Clin Oncol,* 139**,** 739-46.

YAN, C., GRIMM, W. A., GARNER, W. L., QIN, L., TRAVIS, T., TAN, N. & HAN, Y. P. 2010. Epithelial to mesenchymal transition in human skin wound healing is induced by tumor necrosis factor-alpha through bone morphogenic protein-2. *Am J Pathol,* 176**,** 2247-58.

YANG, M. H., HSU, D. S., WANG, H. W., WANG, H. J., LAN, H. Y., YANG, W. H., HUANG, C. H., KAO, S. Y., TZENG, C. H., TAI, S. K., CHANG, S. Y., LEE, O. K. & WU, K. J. 2010. Bmi1 is essential in Twist1-induced epithelial-mesenchymal transition. *Nat Cell Biol,* 12**,** 982-92.

YANG, Z., GARCIA, A., XU, S., POWELL, D. R., VERTINO, P. M., SINGH, S. & MARCUS, A. I. 2013. Withania somnifera root extract inhibits mammary cancer metastasis and epithelial to mesenchymal transition. *PLoS One,* 8**,** e75069.

YAO, X., CHEN, X., COTTONHAM, C. & XU, L. 2008. Preferential utilization of Imp7/8 in nuclear import of Smads. *J Biol Chem,* 283**,** 22867-74.

YATES, B. P., PECK, M. A. & BERGET, P. B. 2013. Directed evolution of a fluorogen-activating single chain antibody for function and enhanced brightness in the cytoplasm. *Mol Biotechnol,* 54**,** 829-41.

YAU, K. Y., GROVES, M. A., LI, S., SHEEDY, C., LEE, H., TANHA, J., MACKENZIE, C. R., JERMUTUS, L. & HALL, J. C. 2003. Selection of hapten-specific single-domain antibodies from a non-immunized llama ribosome display library. *J Immunol Methods,* 281**,** 161-75.

YAUCH, R. L., JANUARIO, T., EBERHARD, D. A., CAVET, G., ZHU, W., FU, L., PHAM, T. Q., SORIANO, R., STINSON, J., SESHAGIRI, S., MODRUSAN, Z., LIN, C. Y., O'NEILL, V. & AMLER, L. C. 2005. Epithelial versus mesenchymal phenotype determines in vitro sensitivity and predicts clinical activity of erlotinib in lung cancer patients. *Clin Cancer Res,* 11**,** 8686-98.

YOOK, J. I., LI, X. Y., OTA, I., HU, C., KIM, H. S., KIM, N. H., CHA, S. Y., RYU, J. K., CHOI, Y. J., KIM, J., FEARON, E. R. & WEISS, S. J. 2006. A Wnt-Axin2-GSK3beta cascade regulates Snail1 activity in breast cancer cells. *Nat Cell Biol,* 8**,** 1398-406.

YU, L., HEBERT, M. C. & ZHANG, Y. E. 2002. TGF-beta receptor-activated p38 MAP kinase mediates Smad-independent TGF-beta responses. *EMBO J,* 21**,** 3749-59.

YU, M., BARDIA, A., WITTNER, B. S., STOTT, S. L., SMAS, M. E., TING, D. T., ISAKOFF, S. J., CICILIANO, J. C., WELLS, M. N., SHAH, A. M., CONCANNON, K. F., DONALDSON, M. C., SEQUIST, L. V., BRACHTEL, E., SGROI, D., BASELGA, J., RAMASWAMY, S., TONER, M., HABER, D. A. & MAHESWARAN, S. 2013. Circulating breast tumor cells exhibit dynamic changes in epithelial and mesenchymal composition. *Science,* 339**,** 580-4.

ZEISBERG, M., YANG, C., MARTINO, M., DUNCAN, M. B., RIEDER, F., TANJORE, H. & KALLURI, R. 2007. Fibroblasts derive from hepatocytes in liver fibrosis via epithelial to mesenchymal transition. *J Biol Chem,* 282**,** 23337-47.

ZHANG, W., FENG, M., ZHENG, G., CHEN, Y., WANG, X., PEN, B., YIN, J., YU, Y. & HE, Z. 2012. Chemoresistance to 5-fluorouracil induces epithelial-mesenchymal transition via up-regulation of Snail in MCF7 human breast cancer cells. *Biochem Biophys Res Commun,* 417**,** 679-85.

ZHENG, H., LI, W., WANG, Y., LIU, Z., CAI, Y., XIE, T., SHI, M., WANG, Z. & JIANG, B. 2013. Glycogen synthase kinase-3 beta regulates Snail and beta-catenin expression during Fas-induced epithelial-mesenchymal transition in gastrointestinal cancer. *Eur J Cancer,* 49**,** 2734-46.

ZHOU, B. P., DENG, J., XIA, W., XU, J., LI, Y. M., GUNDUZ, M. & HUNG, M. C. 2004. Dual regulation of Snail by GSK-3beta-mediated phosphorylation in control of epithelial-mesenchymal transition. *Nat Cell Biol,* 6**,** 931-40.

ZHOU, W., LV, R., QI, W., WU, D., XU, Y., LIU, W., MOU, Y. & WANG, L. 2014. Snail contributes to the maintenance of stem cell-like phenotype cells in human pancreatic cancer. *PLoS One,* 9**,** e87409.

ZHU, M., GONG, X., HU, Y., OU, W. & WAN, Y. 2014. Streptavidin-biotin-based directional double Nanobody sandwich ELISA for clinical rapid and sensitive detection of influenza H5N1. *J Transl Med,* 12**,** 352.

ZHU, Q. S., ROSENBLATT, K., HUANG, K. L., LAHAT, G., BROBEY, R., BOLSHAKOV, S., NGUYEN, T., DING, Z., BELOUSOV, R., BILL, K., LUO, X., LAZAR, A., DICKER, A., MILLS, G. B., HUNG, M. C. & LEV, D. 2011. Vimentin is a novel AKT1 target mediating motility and invasion. *Oncogene,* 30**,** 457-70.

ZOLGHADR, K., GREGOR, J., LEONHARDT, H. & ROTHBAUER, U. 2012. Case study on live cell apoptosis-assay using lamin-chromobody cell-lines for high-content analysis. *Methods Mol Biol,* 911**,** 569-75.

ZOLGHADR, K., MORTUSEWICZ, O., ROTHBAUER, U., KLEINHANS, R., GOEHLER, H., WANKER, E. E., CARDOSO, M. C. & LEONHARDT, H. 2008. A fluorescent two-hybrid assay for direct visualization of protein interactions in living cells. *Mol Cell Proteomics,* 7**,** 2279-87.

108

6 ANNEX

6.1 Publications

Primary literature

Parts of this thesis are published in:

Maier J., Traenkle B., Rothbauer R. Real-time analysis of epithelial-mesenchymal transition using fluorescent single-domain antibodies. Sci Rep. 2015 Aug 21;5:13402.
http://www.nature.com/articles/srep13402

Further publications:

Panza P, **Maier J**, Schmees C, Rothbauer U, Söllner C Live imaging of endogenous protein dynamics in zebrafish using chromobodies. Development. 2015 May 15;142(10):1879-84.

Traenkle B, Emele F, Anton R, Poetz O, Haeussler RS, **Maier J**, Kaiser PD, Scholz AM, Nueske S, Buchfellner A, Romer T, Rothbauer U. Monitoring Interactions and Dynamics of Endogenous Beta-catenin With Intracellular Nanobodies in Living Cells. Mol Cell Proteomics. 2015 Mar;14(3):707-23.

Muth F, Günther M, Bauer SM, Döring E, Fischer S, **Maier J**, Drückes P, Köppler J, Trappe J, Rothbauer U, Koch P, Laufer SA. Tetra-substituted pyridinylimidazoles as dual inhibitors of p38α mitogen-activated protein kinase and c-Jun N-terminal kinase 3 for potential treatment of neurodegenerative diseases. J Med Chem. 2015 Jan 8.

Heubach Y, Planatscher H, Sommersdorf C, Maisch D, **Maier J**, Joos TO, Templin MF, Poetz O. From spots to beads-PTM-peptide bead arrays for the characterization of anti-histone antibodies. Proteomics. 2013 Mar;13(6):1010-5.

Hagn M, Schwesinger E, Ebel V, Sontheimer K, **Maier J**, Beyer T, Syrovets T, Laumonnier Y, Fabricius D, Simmet T, Jahrsdörfer B. Human B cells secrete granzyme B when recognizing viral antigens in the context of the acute phase cytokine IL-21. J Immunol. 2009 Aug 1;183(3):1838-45.

Jahrsdörfer B, Vollmer A, Blackwell SE, **Maier J**, Sontheimer K, Beyer T, Mandel B, Lunov O, Tron K, Nienhaus GU, Simmet T, Debatin KM, Weiner GJ, Fabricius D. Granzyme B produced by human plasmacytoid dendritic cells suppresses T-cell expansion. Blood. 2010 Feb 11;115(6):1156-65.

Manuscript in preparation:

K. Schorpp, I. Rothenaigner, **J. Maier**, B. Traenkle, M. Jung, U. Rothbauer and K. Hadian Identification of cell cycle modulators using the Chromobody technology in a multiplexed High-Content Screening approach.

Review article

Kaiser PD, **Maier J**, Traenkle B, Emele F, Rothbauer U. Recent progress in generating intracellular functional antibody fragments to target and trace cellular components in living cells. Biochim Biophys Acta. 2014 Nov;1844(11):1933-1942.

ANNEX

Conferences:

Presentation:

Maier J, Sannino G, Schmees C, Rothbauer U. Generation of a cell-based system to visualize epithelial-mesenchymal transition in tumor progression. Molecular Life Sciences 2013, Frankfurt

Poster:

Maier J., Traenkle B., Rothbauer R. Intracellular nanobodies to trace dynamic changes of endogenous vimentin in living cells. FEBS Congress 2015, Berlin, Germany

Maier J, Sannino G, Schmees C, Rothbauer U. Generation of single domain antibodies to trace EMT marker proteins in living cells. TEMTIA 2013, Alicante, Spanien

Maier J, Sannino G, Schmees C, Rothbauer U. Generation of a cell-based system to visualize epithelial-mesenchymal transition in tumor progression. Molecular Life Sciences 2013, Frankfurt, Germany

6.2 Eidesstattliche Erklärung

Ich erkläre hiermit, dass ich die zur Promotion eingereichte Arbeit mit dem Titel: „Novel Nanobodies and Chromobodies to Study Biomarkers of Epithelial-Mesenchymal Transition (EMT)" selbständig verfasst, nur die angegebenen Quellen und Hilfsmittel benutzt und wörtlich oder inhaltlich übernommene Stellen als solche gekennzeichnet habe. Ich erkläre, dass die Richtlinien zur Sicherung guter wissenschaftlicher Praxis der Universität Tübingen (Beschluss des Senats vom 25.5.2000) beachtet wurden. Ich versichere an Eides statt, dass diese Angaben wahr sind und dass ich nichts verschwiegen habe. Mir ist bekannt, dass die falsche Abgabe einer Versicherung an Eides statt mit Freiheitsstrafe von bis zu drei Jahren oder mit Geldstrafe bestraft wird.

Tübingen den, 13.10.2015   _____

Julia Maier

6.3 Danksagung